UNIVERSITÀ DEGLI STUDI DI
CASSINO E DEL LAZIO MERIDIONALE

Corso di Dottorato in
Metodi, Modelli e Tecnologie per l'Ingegneria

Ciclo XXXVII

Towards a Sustainable Future: The Role of CFD in Innovating Indoor Environmental Quality and Energy Systems

SSD: ING-IND07/A

Coordinatore del Corso
Chiar.mo Prof. Fabrizio Marignetti

Dottorando
Christian Canale

SUPERVISORI
Chiar.mo Prof. Gino Cortellessa
Chiar.mo Prof. Fausto Arpino

UNIVERSITÀ DEGLI STUDI DI CASSINO E DEL LAZIO MERIDIONALE

CORSO DI DOTTORATO IN METODI, MODELLI E TECNOLOGIE PER L'INGEGNERIA

December 18, 2024

Author: **Christian Canale**

Title: **Towards a Sustainable Future: The Role of CFD in Innovating Indoor Environmental Quality and Energy Systems**

Department: **Dipartimento di Ingegneria Civile e Meccanica**

Degree: **Doctor of Philosophy**

Permission is herewith granted to the university to circulate and to have copied for non-commercial purposes, at its discretion, the above title upon the request of individuals or institutions.

Signature of Author

TABLE OF CONTENTS

Summary

In light of the significant challenges presented by the 21st century, sustainable development emerges as a crucial imperative. It embodies our collective responsibility to address environmental, social, and economic issues, thereby ensuring an improved quality of life for both present and future generations.

This doctoral dissertation offers a pathway toward a safer and more sustainable future by investigating innovative solutions that fulfill the immediate need for healthier indoor environments, while also aiming for the long-term goal of achieving a carbon-neutral landscape. In all three parts of the doctoral thesis, the use of experimental and Computational Fluid Dynamics (CFD) approaches is evident to study and evaluate different aspects of the engineering field and sustainability world. Environmental aspects, indoor air quality and efficiency of energy systems are the main components of this dissertation.

In Part I of the dissertation, the focus is on energy conversion systems and the decarbonization strategies associated with these engineering systems. Specifically, Waste-to-Energy (WtE) plants play a significant role in the global waste management economy and have a substantial impact on climate-altering substances that pose risks to both the environment and human health. This section analyzes various Computational Fluid Dynamics (CFD) numerical approaches to understand and evaluate the operating conditions and the evolution of syngas within the combustion chamber. A comparison is made between a numerical gaseous combustion strategy and non-reacting and lumped model approaches, demonstrating that CFD methods are crucial for accurately assessing the operating conditions of WtE plants and for minimizing the formation of dioxins and other harmful climate-altering substances. Additionally, CFD numerical models have been utilized in the study of orifice plate flowmeters in the transportation sector, to enhance the efficiency of experimental procedures and novel fluid tests.

Part II centres on the modelling of Indoor Air Quality (IAQ) in indoor environments using both numerical and experimental techniques. This section of the dissertation, encompassing Chapters 4, 5, and 6, builds upon the evaluation and refinement of numerical Lagrangian methods, underscoring the vital role of Computational Fluid Dynamics (CFD) in analyzing airflow patterns, particularly in close-contact and shared settings. Despite the extensive exploration of the Lagrangian approach to airborne particles in scientific literature, some unresolved challenges remain. To address these

gaps, this section introduces a comprehensive benchmark study aimed at enhancing the reliability and accuracy of numerical methods. Chapter 4 focuses on the physical modelling of transport routes for respiratory particles and integrates CFD into the Lagrangian analysis. Chapter 5 details an experimental campaign conducted at the Aerodynamics Laboratories of Delft University of Technology. In this study, a side mirror model of a car was tested in an open-jet facility, where velocity measurements were taken using Particle-Tracking Velocimetry (PTV) under three distinct seeding particle scenarios. This chapter discusses time-averaged velocity fields, and velocity fluctuations, and provides a thorough uncertainty analysis of the experimental results.

The findings from Chapter 5 are subsequently employed in Chapter 6 to validate a CFD tool developed within the OpenFOAM framework. This chapter includes a comparative analysis of Unsteady Reynolds-Averaged Navier-Stokes (URANS), Large Eddy Simulation (LES), and Detached Eddy Simulation (DES) methodologies, offering valuable insights into the strengths and limitations of each method in replicating the experimental outcomes.

Part III redirects focus to the implementation of the models created and examined in the previous section. Specifically, it looks at a face-to-face arrangement between individuals and a patented protective device. This section provides an assessment of the numerical strategy outlined in Chapter 4 concerning indoor air quality (IAQ), which serves as the core component of indoor environmental quality (IEQ). The emphasis is on the examination of IAQ and infection risk potential (IRP), carried out through both experimental methods and Computational Fluid Dynamics (CFD) simulations, across two specific scenarios involving close interactions between two individuals in a shared space. An analysis of airborne particle transmission behavior in close contact situations was detailed in Chapter 7. A comprehensive method was formulated to evaluate the risk of SARS-CoV-2 infection during close proximity encounters (less than 2 meters). A CFD numerical model was created to estimate the volume of droplets and the viral load inhaled and deposited on a susceptible person at varying distances. The results of the model were validated using Particle Image Velocimetry (PIV) measurements, which defined the airflow resulting from human exhalation. The research is centered on direct interactions in stagnant air scenarios, integrating thermo-fluid dynamic modeling of exhaled droplets and viral load to evaluate infection risk. Chapter 8 shifts its focus to a larger indoor setting: a university lecture hall. The investigation examines how varying the airflow rate from the ventilation system influences the dispersion of airborne droplets released by a teacher lecturing for a 2-hour period. Findings indicate that increasing the airflow rate from

the HVAC system does not consistently enhance indoor air quality or lower occupant exposure. The dissertation then analyzes a personal protective device, which is evaluated in both face-to-face and shared environmental contexts. CFD plays a crucial role in delivering valuable insights and analysis regarding the fluid dynamics of the device and the movement of respiratory particles in the examined setup.

List of Symbols

The notation used is given here in the following order: upper-case Roman, lower-case Roman, upper-case Greek, lower-case Greek, constants, acronyms and abbreviations, superscripts, and subscripts.

Upper-case Roman

AER	Air exchange rate via ventilation	h^{-1}
C_D	Discharge coefficient	-
Co	Courant number	-
C_P	Specific heat at constant pressure	J kg^{-1} K^{-1}
C_V	Specific heat at constant volume	J kg^{-1} K^{-1}
$D(c_v)$	Dose of RNA copies inhaled by the exposed subject	RNA copies
E_{vl}	Viral load emission rate	RNA copies h^{-1}
EF_f	Emission factor of the fuel	kg CO_2/Sm^3
ER_N	Droplet number emission rate	droplet s^{-1}
ER_V	Droplet volume emission rate	µl s^{-1}
$\boldsymbol{F}_{Basset}$	Basset force	N
$\boldsymbol{F}_{BM}$	Brownian motion force	N
$\boldsymbol{F}_{body}$	Body force	N
$\boldsymbol{F}_{D}$	Drag force	N
$\boldsymbol{F}_{G}$	Gravity force	N
$\boldsymbol{F}_{interaction}$	Interaction force	N
$\boldsymbol{F}_{Magnus}$	Magnus force	N
$\boldsymbol{F}_{pp}$	Particle-particle interaction force	N
$\boldsymbol{F}_{pressure}$	Pressure force	N

$\boldsymbol{F}_{pw}$	Particle-wall interaction force	N
$\boldsymbol{F}_{Saffman}$	Saffman force	N
$\boldsymbol{F}_{surface}$	Surface force	N
$\boldsymbol{F}_{VM}$	Virtual mass force	N
Pr	Prandtl number	-
Q	Volumetric flow rate	$m^3\ h^{-1}$
$\mathcal{R}_{xx}, \mathcal{R}_{yy}$	Reynolds normal stresses	$m^2\ s^{-2}$
$\mathcal{R}_{xy}$	Reynolds shear stress	$m^2\ s^{-2}$
R	Individual risk of infection	-
Re	Reynolds number	-
Re_l	Turbulence Reynolds number	-
S	Number of susceptible occupants	-
S_x	Source term of the quantity x	
SOC_{HST}	State of charge of the HST	-
Stk	Stokes number	-
T	Temperature	K, °C
T_0	Reference temperature (Equation (1.11))	K
V	Droplet volume concentration	$\mu l\ cm^{-3}$

Upper-case Greek

Γ	Diffusion coefficient (Equation (2.27))	
Δ	Cutoff width	m
Δh	Characteristic size of the mesh cell	m
Δt	Pulse separation	ms
$\Delta\vartheta$	Time step	s
Φ	Dissipation function	$kg\ m^{-1}\ s^{-3}$
Ω	Vorticity	s^{-1}

Lower-case Greek

ε	Turbulent kinetic energy dissipation rate	$m^2\ s^{-3}$
η	Kolmogorov length scale	m
κ	Thermal conductivity	$W\ m^{-1}\ K^{-1}$
λ	Second viscosity ($\lambda = -2/3\mu$)	Pa s

μ	Dynamic viscosity	Pa s
μ_T	Eddy (turbulent) viscosity	Pa s
ν	Molecular viscosity	$m^2\ s^{-1}$
ν_{SGS}	SGS viscosity	$m^2\ s^{-1}$
ρ	Air density	$kg\ m^{-3}$
ρ_0	Reference density (Equation (1.11))	$kg\ m^{-3}$
ρ_d	Droplet density	$kg\ m^{-3}$
τ_d	Droplet response time	s
τ_f	Flow characteristic time scale	s
τ_{SGS}	Subgrid-scale Reynolds stresses	$kg\ m^{-1}\ s^{-2}$
φ	General property per unit mass	
ω	Specific dissipation rate	s^{-1}

Lower-case Roman

c_v		
d_d		
f#	f-stop	
h_c		
k	Turbulent kinetic energy	m^2s^{-2}
$k_{resolved}$	Resolved turbulent kinetic energy	m^2s^{-2}
k_{total}	Total turbulent kinetic energy	m^2s^{-2}
l	Characteristic size of the largest eddies	m
ℓ	Turbulent mixing length	m
k_c	Coverage factor	-
k	Turbulent kinetic energy	$m^2\ s^{-2}$
$k_{resolved}$	Resolved turbulent kinetic energy	$m^2\ s^{-2}$
p	Pressure	Pa
p_a	Water vapor partial pressure	Pa
r	Eddy size	m
t	Time	s

$\mathbf{u}$	Velocity vector	$m\ s^{-1}$
u	Velocity component in the x direction	$m\ s^{-1}$

Acronyms and abbreviations

1D	One-dimensional
2D	Two-dimensional
3D	Three-dimensional
ACH	Air changes per hour
BC	Boundary conditions
CCS	Carbon Capture and Storage
CFD	Computational Fluid Dynamics
CPU	Central Processing Unit
CV	Control volume
DNS	Direct numerical simulation
FOV	Field of view
FVM	Finite Volume Method
HFSB	Helium Filles Soap Bubbles
IAQ	Indoor air quality
IEQ	Indoor environmental quality
IRP	Infectious respiratory particle
ISO	International Organization for Standardization
KE	Kinetic energy
LES	Large eddy simulation
LPT	Lagrangian Particle Tracking
OpenFOAM	Open-Source Field Operation and Manipulation
PISO	Pressure Implicit with Splitting of Operator
PIV	Particle Image Velocimetry
RANS	Reynolds-averaged Navier-Stokes
RMSE	Root Mean Squared Error
SDGs	Sustainable Development Goals
SGS	Subgrid scale
SIMPLE	Semi-Implicit Method for Pressure-Linked Equations

SST	Shear Stress Transport
STC	Standard Test Conditions
TKE	Turbulent kinetic energy
URANS	Unsteady RANS
WHO	World Health Organization

List of Figures

List of Tables

INTRODUCTION

1.1 Research background and scope

The last decade has been marked by the need of society to shift towards a holistic approach to global development. The only key to success is represented by sustainable development which integrates economic growth, social inclusion, and environmental protection. In a common sense, sustainable development as development that meets the needs of the present without compromising the ability of future generations to meet their own needs. This concept highlights the importance of balancing current developmental needs with the sustainability of resources and the environment for future generations. Sustainable development aims to create a balanced and equitable future by addressing these interconnected dimensions. This approach ensures the well-being of current populations and safeguards the resources and ecosystems needed by future generations. The transition to sustainable development requires innovative solutions, collaborative efforts, and a commitment to long-term thinking, as the world faces challenges such as climate change, resource depletion, and social inequality. As we move forward, embracing sustainable development principles will be crucial in building resilient communities, fostering inclusive economic progress, and preserving our planet's health.

This thesis delves into the intersection of these critical areas, exploring how improvements in indoor air quality and the efficiency of energy systems can contribute to sustainable development goals. Indoor air quality, an overlooked aspect of environmental health, has significant implications for human well-being, productivity, and quality of life. By investigating innovative solutions and assessing their impact on both environmental sustainability and human health, this research aims to provide actionable insights that align with the broader objectives of the SDGs. This includes examining cutting-edge technologies, policies, and practices that can improve air quality within buildings, such as advanced ventilation systems, air purifiers, and sustainable building materials. Furthermore, the efficiency of energy systems is crucial for reducing environmental impact and enhancing energy security and economic stability.

The present thesis aims to contribute to addressing several Sustainable Development Goals (SDGs):

- **SDG 3**: Ensure healthy lives and promote well-being for all ages by reducing mortality, combating diseases, and providing access to essential health services and medicines.
- **SDG 7**: Ensure access to affordable, reliable, sustainable, and modern energy for all by increasing renewable energy, improving energy efficiency, and expanding infrastructure.
- **SDG 11**: Make cities and human settlements inclusive, safe, resilient, and sustainable by ensuring access to housing and services, enhancing sustainable urbanization, and reducing environmental impact.
- **SDG 13**: Take urgent action to combat climate change and its impacts by strengthening resilience, integrating climate measures into policies, and improving education and capacity on climate change.
- **SDG 15**: Protect, restore, and promote sustainable use of terrestrial ecosystems, manage forests, combat desertification, and halt biodiversity loss to ensure the sustainability of land resources.

Through a multidisciplinary approach, this study aims to enhance our understanding of how integrated strategies can promote healthier, more energy-efficient, and sustainable communities. It will combine insights from environmental science, engineering, public health, and urban planning to develop comprehensive frameworks for sustainable development. By aligning with the Sustainable Development Goals (SDGs) 3 and 11, which prioritize the well-being and security of individuals in our global society, this thesis explores the critical role of indoor environmental air quality in promoting health and sustainable urban living. Poor air quality can significantly impact both physical and mental health, making it essential to ensure clean and safe indoor environments in achieving these goals. This work examines various engineering strategies aimed at improving indoor air quality (IAQ), including advanced ventilation systems, air purification technologies, and sustainable building designs. These strategies not only contribute to the health and well-being of occupants but also support the development of sustainable cities and communities by reducing environmental impacts and enhancing the resilience of urban infrastructures. The thesis also highlights the intersection of health, technology, and sustainability in fostering environments that are both livable and sustainable. SDGs 7, 13, and 15 emphasize environmental sustainability, conservation, and climate action. Waste-to-

energy (WTE) plants, carbon capture systems, and advanced energy accounting methods play crucial roles within this framework. WTE plants transform municipal and industrial waste into energy, decreasing reliance on landfills and lowering greenhouse gas emissions while producing renewable energy. This supports the integration of renewable energy sources (RESs) into the energy grid, promoting a circular economy and reducing dependence on fossil fuels. Carbon capture systems enhance this process by capturing CO2 emissions generated during waste combustion in WTE plants. The captured CO2 can then be stored underground or repurposed in various industrial applications, significantly reducing the overall carbon footprint. To ensure the efficiency and effectiveness of these technologies, developing precise energy accounting and measurement systems is essential. These systems allow for accurate tracking of energy production, consumption, and emission reductions, providing valuable data for optimizing operations and demonstrating compliance with sustainability goals. By implementing WTE plants, carbon capture technologies, and robust energy accounting methods, we can enhance energy efficiency, mitigate climate change impacts, and protect terrestrial ecosystems, aligning with the objectives of sustainable energy access, climate action, and ecosystem preservation. This comprehensive approach paves the way for a more resilient and environmentally sustainable future.

1.2 Thesis structure

This thesis is organized into three key sections, each delving into a unique subject area and consisting of independent chapters. Each section is outlined below, linking it to the broader context discussed in the previous section and offering a clear guide for readers through the document. Final reflections and potential directions for future research are included in Chapter 9.

I. **ENERGY CONVERSION SYSTEMS AND DECARBONIZATION STRATEGIES**. This section of the thesis focuses on decarbonization strategies and energy conversion systems in Chapter 2 and Chapter 3. It emphasizes Waste-to-Energy (WtE) systems, which convert municipal and industrial waste into valuable energy, reducing landfill use, greenhouse gas emissions, and contributing to the circular economy. These energy conversion systems are subject to strict national regulations, with controlling combustion temperature being a major challenge. Chapter 2compares different numerical CFD strategies, including a lumped parameters model

and two URANS CFD models. It also explores the development and implementation of advanced instruments for monitoring and optimizing the combustion process. One critical aspect is finding effective methods to monitor the combustion chamber to prevent carbon monoxide formation, which is a significant environmental and health concern. The chapter evaluates various sensors and measurement technologies, such as real-time gas analyzers and advanced infrared thermography, to assess their effectiveness in detecting and controlling CO levels. The goal is to identify the best strategy for optimal combustion conditions, emission reduction, and overall efficiency improvement of WtE systems, thus contributing to effective decarbonization strategies and environmental sustainability.Chapter 3 explores the development of advanced flow measurement techniques for enhanced energy accounting accuracy using numerical simulations. These measurement systems are crucial for precise tracking of fuel consumption, energy use, and emissions within the sector. Improved flow measurement technologies enable more accurate monitoring and reporting of energy performance, which is essential for optimizing operational efficiency and achieving regulatory compliance. By implementing state-of-the-art flow measurement solutions, this thesis aims to support better energy management practices, reduce operational costs, and facilitate the transition to more sustainable transport solutions

II. **INDOOR AIR QUALITY: MODELLING AND BENCHMARKING**. This part of the dissertation (Chapter 4, Chapter 5 and **Error! Reference s ource not found.**) builds directly on the modelling and benchmarking of the numerical lagrangian techniques, which highlights the value of Computational Fluid Dynamics (CFD) in studying and evaluating airflow patterns within indoor environments, particularly in close contact and shared scenarios. However, the reliability of these numerical results is highly dependent on the simplifying assumptions used. Specifically, this chapter addresses the challenges related to the Lagrangian approach of airborne particles - a topic that has been sufficiently explored in existing scientific literature, but has still some shadow zone that need to be explored. This gap prompted the development of an extended and comprehensive benchmark study, aimed at providing valuable insights and refining the numerical techniques employed in the previous sections. Chapter 5 delves into the experimental campaign that was carried out in the Delft University of

Technology Aerodynamics Laboratories. A side mirror model of a car was tested in an open-jet facility of the TU Delft University and a velocity measurement was performed through the Particle-Tracking Velocimetry (PTV) technique, under three distinct seeding particles. The time-averaged velocity fields are presented and discussed, as well as the velocity fluctuations. Moreover, a detailed uncertainty analysis of the experimental results is presented. Experimental measurements are employed in Chapter 5 to validate the CFD tool developed in the OpenFOAM environment. Here, a URANS, LES and DES approaches are compared to the experimental study.

III. **INDOOR ENVIRONMENTAL QUALITY: APPLICATIONS**. This section presents an evaluation of the numerical strategy discussed in Chapter 4 in the context of indoor air quality (IAQ), which serves as the foundational pillar of indoor environmental quality (IEQ). The focus is on the analysis of the IAQ and IRP, conducted through both experiments and Computational Fluid Dynamics (CFD) simulations, in two distinct scenario of close contact between two subject and a shared environment. An evaluation of the behaviour of the airborne particle transmission in a close contact scenario has been performed in Chapter 7. An integrated approach was developed to assess the risk of SARS-CoV-2 infection in close proximity scenarios (less than 2 meters). A CFD numerical model to estimate the volume of droplets and the viral load received by a susceptible person through inhalation and deposition at various distances. The model's results were validated using Particle Image Velocimetry (PIV) measurements, which characterized the airflow from human expiratory activities. The study focuses on face-to-face interactions in stagnant air conditions, combining thermo-fluid dynamic modeling of exhaled droplets and viral load to assess the infection risk. Chapter 8 focuses on a large indoor environment: a university lecture room. The study explores the effects of changing the airflow rate provided by the ventilation system on the distribution of airborne droplets emitted by a teacher speaking in front of the class during a 2-hour lesson. Results show that increasing the air flow rate from the HVAC system is not always effective in improving indoor air quality and reducing occupant exposure. The dissertation moves on the analysis of a personal protection device, which is tested in both face-to-face and shared environment configurations. The CFD is essential to provide useful results and analysis of the fluid dynamic

of the device and also on the transportation of the respiratory particles in the studied configuration.

I

ENERGY CONVERSION SYSTEMS AND DECARBONIZATION STRATEGIES

CHAPTER 2. Waste-To-Energy systems and CFD modeling

2.1 Introduction

The increasing global demand for energy and the escalating challenges of waste management have intensified the focus on Waste-to-Energy (WtE) technologies as a viable and sustainable solution. WtE processes provide a dual advantage: they not only mitigate the environmental impact of waste disposal by reducing reliance on landfills and curbing greenhouse gas emissions but also contribute to generating renewable energy, addressing two critical global challenges simultaneously. As nations strive to meet their energy needs while adhering to stringent environmental regulations and sustainability goals, WtE has emerged as a crucial component of the circular economy. By converting the energy embedded in waste into electricity, heat, or fuel, WtE systems offer a pathway to reducing dependence on fossil fuels and enhancing energy security [1].

The regulatory landscape surrounding WtE technologies in Italy is particularly significant due to the country's commitment to environmental protection and energy efficiency. Italian regulations on dioxin emissions, which are by-products of the combustion process in WtE plants [2], are among the most stringent in the world. Dioxins, a group of chemically related compounds known for their environmental persistence and potential health risks, are subject to strict emission limits under Italian law. These regulations are in line with the European Union's Waste Incineration Directive (2000/76/EC) and the Industrial Emissions Directive (2010/75/EU), which set the maximum allowable dioxin concentration in emissions at 0.1 nanograms per cubic meter (ng/m^3) of air [1]. Italy has implemented these directives with rigorous monitoring and control measures to ensure compliance, often exceeding the baseline requirements through the adoption of advanced filtration and gas cleaning technologies in WtE facilities [2], [3]. .

Moreover, the Italian regulatory framework for WtE systems emphasizes the integration of Best Available Techniques (BAT) to minimize the formation of dioxins and other pollutants during the energy conversion process [4]. This includes the use of optimized combustion conditions, such as maintaining appropriate temperatures and residence times in the combustion chamber, as well as the post-combustion treatment

of flue gases using techniques like selective catalytic reduction (SCR) and activated carbon injection. These measures are not only critical for reducing the environmental footprint of WtE plants but also for ensuring that these facilities operate within the bounds of sustainability and public health protection. The regulatory focus on minimizing dioxin emissions is complemented by Italy's broader strategy to enhance the energy efficiency of WtE systems [5]. This involves the promotion of Combined Heat and Power (CHP) configurations, which optimize the energy recovery process by simultaneously producing electricity and useful thermal energy from waste. CHP systems are particularly valued under Italian energy policies, which incentivize high-efficiency WtE plants through favourable tariffs and certificates for renewable energy production. The integration of WtE into Italy’s energy grid is also supported by policies that encourage the development of district heating networks, further enhancing the overall efficiency and sustainability of these systems [3], [6].

A crucial tool in the advancement and optimization of WtE technologies is Computational Fluid Dynamics (CFD) numerical simulation. CFD simulations play a pivotal role in designing, analysing, and optimising WtE systems by providing detailed insights into the complex fluid flow, heat transfer, and chemical reaction processes occurring within these plants. By modelling the combustion process, CFD can help engineers and researchers understand how waste materials are converted into energy, identify hotspots for potential pollutant formation, and assess the effectiveness of various emission control technologies. For instance, CFD can be used to simulate the formation and dispersion of dioxins within the combustion chamber and flue gas treatment systems, allowing for the optimization of operational parameters such as temperature profiles, oxygen concentration, and residence time to minimize these harmful emissions [7].

CFD simulations also facilitate the study of airflow and mixing patterns within the combustion chamber, which are critical for achieving complete combustion and maximizing energy recovery [8]. By analyzing different configurations and operational strategies, CFD can help optimize the design of WtE plants to enhance their thermal efficiency and reduce the production of unburned residues and pollutants. Furthermore, CFD is invaluable in the integration of WtE systems with other energy recovery processes, such as in CHP configurations, where it can be used to model and optimize the distribution of thermal energy for electricity generation and district heating [9]. The application of CFD in WtE research not only enhances the understanding of the underlying processes but also supports compliance with stringent environmental regulations. By enabling the detailed prediction of pollutant formation

and energy conversion efficiencies, CFD assists in the design of systems that meet regulatory standards for emissions while maximizing energy output. This computational approach aligns with Italy's emphasis on innovation and sustainability in the energy sector, providing a powerful tool for continuous improvement and adaptation of WtE technologies to meet evolving regulatory and environmental challenges[10].

This chapter delves into the role of WtE in enhancing energy efficiency and sustainability within the context of Italian regulations and global best practices, with a special focus on the application of CFD simulations. It examines the technological advancements, economic viability, and environmental benefits associated with WtE systems, alongside the regulatory mechanisms that govern their operation. By analyzing the energy conversion processes, system efficiencies, and the potential for integration with other renewable energy sources, this chapter aims to provide a comprehensive understanding of how WtE can be optimized to support sustainable development and contribute to a low-carbon future while adhering to stringent environmental and public health standards. The integration of CFD simulations into this analysis offers a deeper insight into how these systems can be finely tuned to achieve optimal performance and regulatory compliance.

2.2 Description of the pollutant formations and sustainability process

Waste-to-energy (WtE) systems, which convert municipal solid waste into usable energy, are increasingly recognized for their potential to address the dual challenges of waste management and energy generation. However, the combustion processes inherent in WtE facilities also pose significant environmental challenges, particularly related to the emission of pollutants. These pollutants include particulate matter (PM), nitrogen oxides (NOx), sulfur oxides (SOx), heavy metals like mercury and cadmium, and highly toxic compounds such as dioxins and furans. The release of these substances into the atmosphere can have harmful effects on air quality, human health, and the environment, requiring strict control measures to reduce their impact. The formation of pollutants in WtE systems is largely a result of the incomplete combustion of waste materials and the presence of certain chemicals in the waste stream. Dioxins and furans, for example, are unintentional by-products formed when organic materials containing chlorine are burned at temperatures that are not sufficiently high or are cooled too slowly. These compounds are highly persistent in the environment and can

accumulate in the food chain, leading to serious health risks including cancer, reproductive and developmental problems, and immune system damage. Similarly, NOx and SOx are produced during combustion from the oxidation of nitrogen and sulfur present in the waste, contributing to smog formation, acid rain, and respiratory issues. Heavy metals, when vaporized during combustion, can settle on soil and water bodies, posing long-term environmental hazards and bioaccumulation risks.

To address these environmental and health concerns, WtE facilities are subject to strict regulatory controls designed to limit pollutant emissions. These controls are based on a combination of advanced technological solutions and best operational practices:

- Optimized Combustion: ensuring complete combustion by maintaining high temperatures (typically above 850°C) and sufficient oxygen supply helps to minimise the formation of unburned hydrocarbons, dioxins, and furans. The use of staged combustion, where the fuel is burned in phases, further reduces NOx formation.
- Flue Gas Treatment: After combustion, the flue gases are treated using a series of technologies to capture and neutralize pollutants before they are released into the atmosphere. Common methods include:
  - Electrostatic Precipitators (ESP) and Fabric Filters: These are used to capture particulate matter.
  - Selective Catalytic Reduction (SCR): This technology reduces NOx emissions by converting them into nitrogen and water using a catalyst and ammonia.
  - Acid Gas Scrubbing: SOx and other acid gases are neutralised using alkaline substances like lime or sodium bicarbonate.
  - Activated Carbon Injection: This process is particularly effective for capturing heavy metals and dioxins from the flue gas stream.
- Continuous Monitoring and Compliance: Modern WtE plants have continuous emission monitoring systems (CEMS) to ensure that pollutant levels are consistently below regulatory limits. This allows for real-time adjustments in plant operations to maintain optimal environmental performance.

Efforts to control pollutants from Waste-to-Energy (WtE) systems are intrinsically aligned with the United Nations Sustainable Development Goals (SDGs), which provide a comprehensive framework for promoting sustainable development and

ensuring a healthy environment for future generations [3], [6]. A deep analysis of WtE systems, encompassing both their environmental impact and technological advancements, can significantly enhance their contribution to several key SDGs. For instance, detailed studies on the emission control mechanisms in WtE facilities can directly support SDG 3: Good Health and Well-being by minimizing the release of harmful pollutants such as dioxins, furans, and heavy metals. By refining these processes, WtE plants can achieve lower emissions, leading to improved air quality and a reduction in the incidence of respiratory and other health-related issues, thus advancing global health objectives.

Moreover, an in-depth examination of the energy recovery processes within WtE systems can bolster SDG 7: Affordable and Clean Energy. By optimizing the efficiency of these systems, WtE can become a more reliable and sustainable source of renewable energy, reducing reliance on fossil fuels and contributing to a cleaner energy matrix. Ensuring that this energy is produced in an environmentally responsible manner through advanced pollutant control measures further enhances the sustainability of WtE as a critical component of global energy strategies.

In the context of SDG 11: Sustainable Cities and Communities, comprehensive analysis and optimization of WtE technologies are crucial for effective urban waste management. WtE systems that are designed and operated with a focus on minimizing environmental impacts can help cities manage their waste more sustainably, reducing the need for landfills, lowering associated emissions, and contributing to cleaner, healthier urban environments. This, in turn, supports the development of cities that are resilient, sustainable, and capable of accommodating growing populations without compromising environmental and public health.

Further, by integrating advanced studies on material recovery and waste processing, WtE systems can support SDG 12: Responsible Consumption and Production. Through the adoption of best practices and innovative technologies, WtE can play a pivotal role in the circular economy by converting waste into valuable energy resources, promoting responsible waste management, and minimizing the environmental impact of waste disposal. Rigorous control of pollutants ensures that this energy recovery process does not lead to environmental degradation, aligning with the principles of sustainable production.

Additionally, deep analysis of WtE systems' carbon footprint and their role in reducing greenhouse gas emissions is essential for advancing SDG 13: Climate Action. By optimizing the capture of energy from waste that would otherwise decompose in landfills and emit methane—a potent greenhouse gas—WtE facilities can significantly

contribute to climate change mitigation [4]. Effective pollutant control ensures that the environmental benefits of WtE are not negated by harmful emissions, thereby supporting global efforts to combat climate change. Lastly, reducing emissions of heavy metals and persistent organic pollutants like dioxins through meticulous monitoring and control in WtE systems is crucial for protecting terrestrial ecosystems, aligning with SDG 15: Life on Land. This not only safeguards biodiversity and ecosystem health but also ensures that land remains productive and safe for human use [2], [3]. By thoroughly analyzing and continuously improving WtE systems through rigorous research, advanced technological integration, and best practices, these facilities can significantly contribute to sustainable development in a manner that is well-aligned with global environmental and health goals [7]. The integration of these strategies within the WtE framework not only enhances the sustainability and efficiency of energy production but also ensures that WtE remains a viable and increasingly essential component of the global transition to cleaner, more resilient energy systems.

2.3 Waste-to-Energy case study

Waste-to-Energy (WtE) plant, which converts waste into usable energy such as electricity or heat. Waste is burned in a combustion chamber where primary air is introduced to sustain the process, and the chamber is lined with firebricks for insulation and durability. Heat generated during combustion is captured by overheating heat exchangers to superheat water into high-pressure steam, enhancing energy recovery efficiency. Secondary air is injected into the chamber to ensure complete combustion and reduce unburned pollutants, improving efficiency and environmental performance. The steam produced passes through a vaporizer heat exchanger, where it is utilized for energy production, such as driving turbines for electricity or providing heat for other applications. Thermocouples installed at critical points, like the combustion chamber ceiling, monitor and regulate temperatures to optimize performance and ensure safety.

The geometrical characteristics of the main combustion chamber of the WtE plant considered in this paper, particularly the first three channels of the combustion and post-combustion chambers, are reported in Figure 2.1 . Primary and secondary air inlets are painted in blue colour; the internal surface of the combustion chamber, covered with refractory bricks, is represented in grey; the benches of superheated steam are painted in orange and the benches of vaporizers tubes are yellow. The solid

combustion takes place over the solid combustion grid of the RDF, where the primary air is injected; on the other hand, the gaseous combustion occurs in proximity to the secondary air input area. The exhaust gases, whose trajectory is indicated by the green arrow in Figure 2.1, lap the walls of the post-combustion chamber. The main operating parameters of the plant are summarized in Table 2.1.

Table 2.1. The main operating parameters of the Waste-to-Energy plant are under study.

Characteristic	Value	[M.U]
Electric Power	≅ 11	MW
Steam mass flow rate	60	t/h
Turbine Inlet Temperature	400	°C
Maximum Pressure	60	bar
Fuel mass rate	≅ 12	t/h
Thermal Power	47	MW

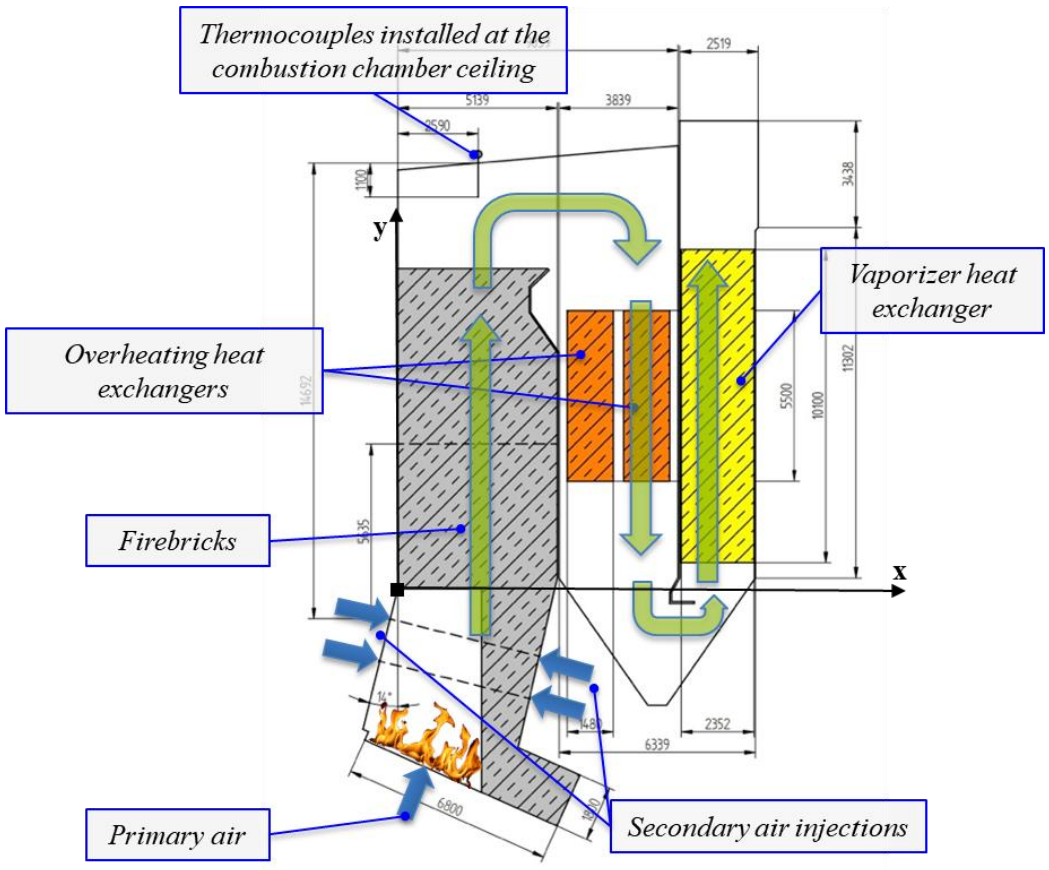

Figure 2.1. Geometrical characteristics of the main combustion chamber related to the plant, with dimensions specified in mm.

Experiments were conducted aimed at collecting temperature profiles inside the post-combustion chamber of the plant. A silicon carbide bar, equipped with four thermocouples, was introduced and kept within the combustion chamber for four days [1]. It was installed at about y=4.64 m from the reference system (about 5.64 m in the y direction from the last secondary air injection). During the experiments, temperature measurements were also collected from the thermocouples installed at the combustion chamber ceiling (at y=13.47 m, corresponding to a distance of about 14.47 m from the last secondary air injection zone), as indicated in Figure 2.1. Locations of temperature measurements are available in Table 2, according to the reference system in Figure 2.1. In particular, Points 1-4 refer to thermocouples installed on the silicon carbide bar, while Points 5 and 6 refer to thermocouples installed at the ceiling of the combustion chamber.

Table 2.2. Measurement point's location in the combustion chamber.

	Coordinate x (m)	**Coordinate y (m)**	**Coordinate z (m)**
Point 1	3.500	4.640	0.010
Point 2	3.500	4.640	0.620
Point 3	3.500	4.640	0.825
Point 4	3.500	4.640	1.400
Point 5	3.500	13.470	2.000
Point 6	3.500	13.470	3.500

To correctly define boundary conditions for analytical and numerical models [11], operative parameters were collected from on-board plant instrumentation and the daily averaged values with associated standard deviations were calculated, as summarized in Table 2.3.

In order to compare the performance of different modeling approaches, the daily averaged operating conditions available in Table 2.4 have been considered, while the daily averaged chemical composition of the RDF burnt on the same day is available in Table 2.5. In addition to the chemical composition, the Lower Heat Value (LHV), determined according to the UNI EN 15400:2011 and the UNI EN 15407:2011, is also available in Table 2.6.

Table 2.3. Daily average operating data of the plant together with standard deviation.

	Average daily value	Standard deviation
Volumetric flow rate of primary air $\left(\frac{Nm^3}{h}\right)$	43888	1188
Volumetric flow rate of secondary air $\left(\frac{Nm^3}{h}\right)$	35493	170
Exhaust flow rate $\left(\frac{Nm^3}{h}\right)$	93251	916
Ceiling temperature of the first radiant channel (K)	1080	26
Average temperature of the bar (K)	1181	106 (max value)
RDF mass flow rate $\left(\frac{t}{h}\right)$	12.4	1.3

Table 2.4. Daily chemical composition of the RDF.

	Methods	Average daily value	Expanded uncertainty
L.H.V (kj/kg)	UNI EN 15400:2011 UNI EN 15407:2011	17025	420
Humidity (%)	UNI EN 15414-3:2011	19.2	1.2
Ashes (%)	UNI EN 15403:2011	14.7	0.4
Sulfur (% dry basis)	UNI EN 15408:2011	0.21	0.02
Hydrogen (% dry basis)	UNI EN 15407:2011	7	1.1
Nitrogen (% dry basis)	UNI EN 15407:2011	1.7	0.2
Carbon (total) (% dry basis)	UNI EN 15407:2011	50.2	3.5
Volatile matter (% dry basis)	UNI EN 15402:2011	86.3	1.1
Carbon (fixed) (by calculation)	by calculation	<2	-
Oxygen (by calculation)	by calculation according to UNI EN 15296:2011	26.2	-

Table 2.5 Daily averaged temperature value measured.

	Daily averaged temperature, T_{avg} (K)	Standard deviation, σ (K)
Point 1	994.3	23.2

Point 2	1138.6	36.4
Point 3	1166.3	35.2
Point 4	1238.0	106.2
Point 5	1091.0	6.6
Point 6	1104.4	6.1

To estimate the uncertainty associated with temperature measurements carried out with the thermocouples installed on the silicon carbide bar, u_{SEN}, the following contributions were considered: i) sensor accuracy u_{ACC}: class I thermocouples (IEC 60584) were adopted, with accuracy equal to 0.4% of the read value in the used temperature range (> 375 °C); ii) sensor calibration u_{CAL}: in absence of the calibration certificate of the used instruments, it was assumed to be equal to the typical value provided by the national LAT (Accredia) laboratories (± 1.5 °C); iii) drift u_{DRIFT}: it is assessed by the long-term stability typical of the instrument and depends on the intensity of its use; it can reasonably be estimated at approximately 1.5 °C/year; iv) resolution u_{RES}, evaluated as $resolution/(2\sqrt{3})$; v) standard deviation of the measured data, σ. The uncertainty associated with the 4/20 mA converter/transmitter was considered negligible. The resulting expression for the standard uncertainty u_{SEN} is given by:

$$u_{SEN} = \sqrt{u_{ACC}^2 + u_{CAL}^2 + u_{DRIFT}^2 + u_{RES}^2 + \sigma^2} \qquad (2.1)$$

Since the contribution to the uncertainty value is related to u_{ACC}, u_{CAL}, u_{DRIFT} and u_{RES} is not larger than $0.1\,K$, the uncertainty u_{SEN}substantially coincides with the value of measurements standard deviation, which is indicative of data daily oscillation around the calculated average value [12]. To define the uncertainty associates to the average temperature of the thermocouples installed on the silicon carbide bar, only the standard deviation was considered, with a coverage factor equal to 2 for all the measurements [13].

2.4 Numerical model

2.4.1 0D mathematical model

Assuming thermodynamic equilibrium and steady conditions, the proposed 0D mathematical model is based on the lumped parameters approach and describes the gasification processes, the gaseous combustion, and the heat exchange taking place in the first vertical channel of the WtE plant dividing it into four control volumes as depicted in Figure 2, where a schematic representation of the different control volumes and the proposed general thermodynamic model is available.

In the VC0 control volume – which is representative of the first step of the chain in which the RDF is converted in syngas - the gasification process is described, according to the following global reaction:

$$CH_xO_yN_z + wH_2O + m(O_2 + 3.76N_2) = n_{H_2}H_2 + n_{CO}CO_2 + n_{CH_4}CH_4 + \left(\frac{z}{2} + 3.76m\right)N_2 \quad (2.2)$$

where $CHxOyNz$ represents the equivalent chemical formula of the feedstock where *x*, *y* and *z* represent the number of atoms of hydrogen, oxygen and nitrogen while w and m represent the mole number of water and oxygen for each mole of carbon [13]. The mass balance for carbon, hydrogen and oxygen is solved. Additionally, the thermodynamic equilibrium equation is solved for the Boudouard reaction, water shift, and methane oxidation [14], [15].

The VC1 control volume – on the top of the primary air inlet and in which the main heat exchanges are located - the heat exchange between syngas and the inner walls of the vertical channel employing the well-known heat exchangers equation.

The VC2 control volume – in which an injection of air is provided to provide the best gaseous combustion characteristics in the domain - describes the mixing of produced syngas with secondary air and successive gaseseous combustion, according to the following reactions:

$$H_2 + \frac{1}{2}O_2 \rightarrow H_2O \qquad r1 = k2[H_2][O_2] \qquad k_2 = 5.26 \times 10^{19} e^{-\frac{20600}{T}} \quad (2.3)$$

$$CO + \frac{1}{2}O_2 \rightarrow CO_2 \qquad r2 = k2[CO][H_2O]^{0.5}[O_2]^{0.5} \qquad k_2 = 3.16 \times 10^{12} e^{-\frac{21664}{T}} \quad (2.4)$$

$$CH_4 + 2O_2 \rightarrow CO_2 + 2H_2O \qquad r3 = k2[CH_4][O_2] \qquad k_3 = 2.552 \times 10^{17} e^{-\frac{11196}{T}} \quad (2.5)$$

$$CO + H_2O \leftrightarrow CO_2 + H_2 \qquad r_{vs} = k_{vs}\left([CO][H_2O] - \frac{[CO_2][H_2]}{k_{vs,eq}}\right) \qquad k_{vs} = 2.778 \times 10^3 e^{-\frac{1511}{T}}, \quad k_{vs,eq} = 0.022\, e^{-\frac{1511}{T}} \quad (2.6)$$

Finally, the VC3 control volume describes heat exchange between exhausts and inner walls of the post-combustion chamber, downstream the gaseous combustion region and up to the ceiling of the first channel, allowing energy recovery from the gaseous combustion of the syngas. For a detailed description of the 0D mathematical model, the interested reader refers to the previous work from Arpino et al. [11].

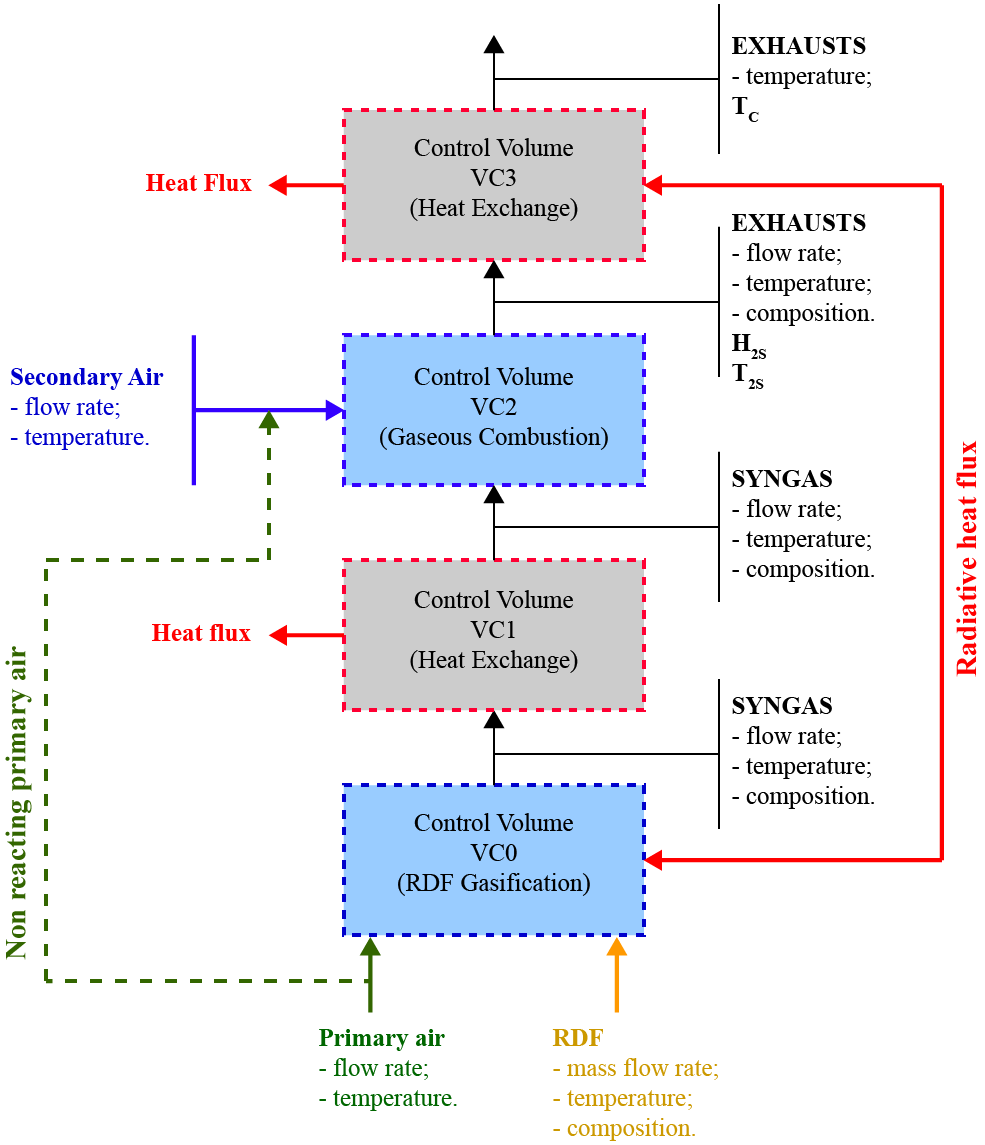

Figure 2.2. Control volumes identified for the construction of the lumped parameters model.

The thermodynamic model requires as input data: the flow rate and temperature of RDF, primary air and secondary air, alongside detailed information about RDF chemical composition. Outputs of the model include exhaust temperature at different

heights of the vertical channel calculated employing the heat exchangers equation and assumed to be uniform at a given height), the distance travelled by exhausts from the last secondary air injection, referred to as H_{2S} (m), and the temperature of exhausts in correspondence of H_{2S} location referred as T_{2S}. Figure 2.2 highlights the flow process of the VC2 and VC3 evaluation

2.4.2 CFD model

Computational Fluid Dynamic (CFD) represents a versatile and powerful tool that provides detailed insights into the complex processes occurring within Waste-to-Energy plants (WtE), allowing better design, improved efficiency, reduced environmental impact, and enhanced operational safety.

In this section, the 3D CFD mathematical and numerical model employed for the description of the WtE plant under investigation is presented. The computational domain employed for 3D CFD numerical simulations is available in Figure 3, where the primary inlet, secondary inlets, and exhaust outlet sections are highlighted in blue, red, and green colour, respectively. The boundary conditions at the primary inlet are determined from the 0D resolution of the RDF gasification process. Additional air enters the domain through the secondary inlets, facilitating gaseous combustion within the system. The 3D CFD model provides a complete description of pressure, velocity, and temperature fields in the combustion and post-combustion chamber of the plant by solving the well-known mass, momentum, and energy conservation equations [16]. Turbulence is modelled with the Unsteady Reynolds Averaged Navier Stokes (URANS) approach, solving the Realizable $k-\epsilon$ model [17], [18].

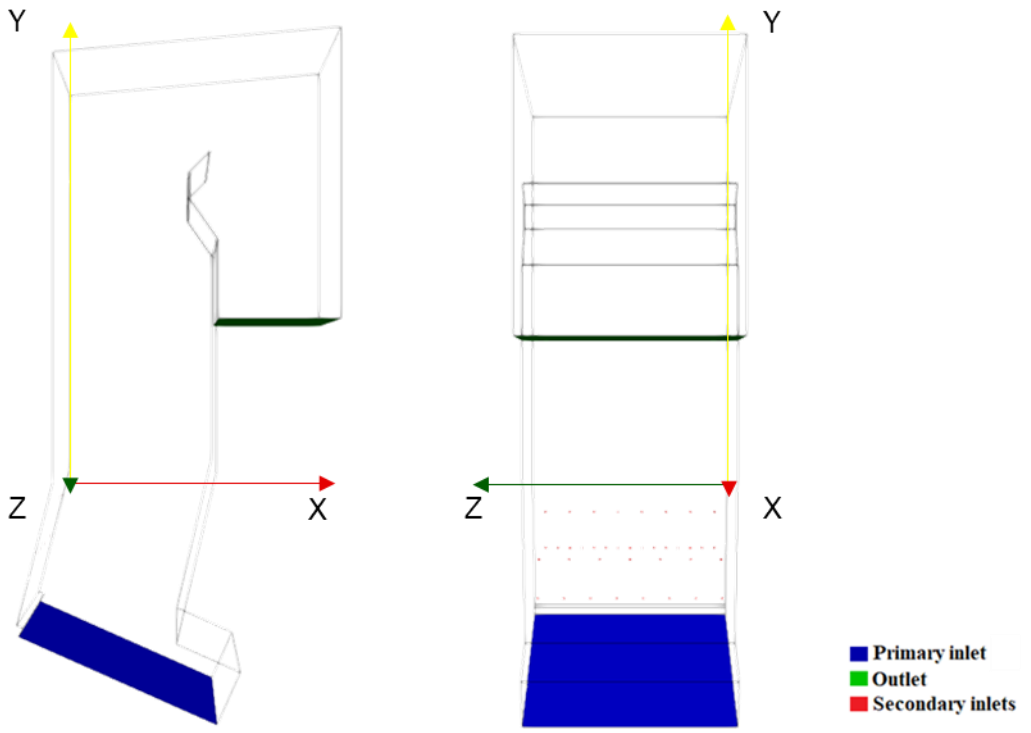

Figure 2.3. Computational domain employed for 3D numerical simulations.

Two different modeling approaches were chosen for 3D simulations, characterized by different detail levels: i) non-reacting CFD model; and ii) reacting CFD model. The non-reacting CFD model does not describe numerically the gaseous combustion of syngas. Conversely, an amount of equivalent heat source term, calculated from the resolution of the 0D thermodynamic model, is imposed in the domain in correspondence to the secondary inlet zone. The reacting CFD model numerically describes the gaseous combustion of syngas, providing detailed information about exhaust composition. For both the non-reacting and the reacting modeling approaches a mass flow rate of syngas at a given temperature is imposed at the primary inlet, obtained from the resolution of the 0D thermodynamic model. Common boundary conditions of the two modeling approaches are presented in Table 2.6, where p (Pa) is the pressure, $T_{sa}(K)$ and $T_{syn}(K)$ represent the secondary air and syngas inlet temperature, respectively, u $\left(\frac{m}{s}\right)$ represents the velocity vector, I is the turbulence intensity, l (m) is the mixing length calculated as the 7% of the characteristic length L (m) of the inlets of the combustion chamber, $\dot{V}$ and $\dot{V}_{syn}$ $\left(\frac{Nm^3}{h}\right)$ represent, respectively the syngas and secondary air mass flow rate entering the domain, k $\left(\frac{m^2}{s^2}\right)$

is the Turbulent Kinetic Energy (TKE), and ϵ $\left(\frac{m^2}{s^3}\right)$ is the turbulent dissipation rate, k $\left(\frac{W}{mK}\right)$ is the thermal conductivity, $\bar{h}$ $\left(\frac{W}{m^2K}\right)$ is the average heat transfer coefficient between exhausts and the inner wall of the combustion chamber, T_w (K) is finally the water temperature.

Table 2.6. Boundary conditions set for both modeling approaches

	Pressure	**Flowrate**	**Temperature**	**Turbulence**	
Secondary Inlets	$\nabla p = 0$	$\dot{V}_{sa} = 35493$	$T_{sa} = 290.2$	I = 0.1	l = 0.0049
Primary Inlet	$\nabla p = 0$	$\dot{V}_{syn}$=58078	$T_{syn} = 1304.8$	I = 0.1	l = 0.5
Outlet	p = 101325	$\nabla \mathbf{u} = 0$	$\nabla T = 0$	$\nabla k = 0$	$\nabla \varepsilon = 0$
Walls	$\nabla p = 0$	**u**=0	$-k\frac{\partial T}{\partial n} = = \bar{h}(T - T_w)$	standard wall functions	standard wall functions

Given the high temperatures reached within the first radiant channel, the thermal energy exchanged due to radiative effects plays a very significant role. Therefore, it is necessary to include radiative heat transfer between the hot flue gases and the chamber walls in the mathematical model. Assuming the internal walls of the combustion chamber to behave as a grey body, the general form of the radiative heat transfer equation (RTE) can be written as follows:

$$dI_\lambda(r,s) = -k_\lambda I_\lambda(r,s) + k_\lambda I_{b\lambda}(r) - \sigma_{s\lambda} I_\lambda(r,s) + \left(\frac{\sigma_{s\lambda}}{4\pi}\right) \int_{4\pi} I_\lambda(r,s^*)\Omega(s^*,s)d\Omega^* \quad (2.7)$$

Where I_λ $\left(\frac{W}{m^2}\right)$ represents the spectral radiation intensity at the point defined by the position vector r and in the direction indicated by the vector *s*, k $\left(\frac{1}{m}\right)$ is the absorption coefficient, σ_s $\left(\frac{1}{\mathrm{m}}\right)$ is the scattering coefficient, and Ω $\left(\frac{m^2}{sr}\right)$ represents the scattering function. The subscripts b and λ refer to blackbody and spectral quantities, respectively. More information about the blackbody model and the related radiation intensity can be found in the available scientific literature [19], [20] and is not included here for brevity. The finite volume Discrete Ordinates Method (fvDOM) from OpenFOAM was utilized to model the radiative heat transfer. This method discretizes the radiative transfer equation (RTE) over a finite number of discrete solid angles,

allowing for an accurate representation of radiative intensity in participating media. The fvDOM is particularly suitable for handling complex geometries and is computationally efficient [21], [22].

Two models were developed in this project, aiming to evaluate the thermo-fluid dynamic characteristics of the flow within the combustion chamber. The models are here depicted:

- **Non-reacting CFD model**: this approach reduces the computational cost of numerical simulations, resulting in quicker convergence. The counterpart is to obtain less detailed results. The heat rate released by gaseous combustion is modelled by adding a heat source term in correspondence to the volume highlighted in blue color in Figure 2.4, obtained by the 0D thermodynamic model [11]. For the specific operating condition under investigation, the equivalent heat power of 21.706 MW achieved by the combustion of fuel and comburent air is released in the computational domain, avoiding the resolution of the combustion mathematical model. The gas entering the computational domain is assumed to be the product of the syngas combustion. The thermophysical properties of the flue gas are determined based on a 0D lumped parameters model, which defines these properties by the composition of each specific mole species [23]. In particular, the specific heat at constant pressure $C_p\left(\frac{J}{kg\,K}\right)$of the flue gas has been calculated based on its composition and different temperature values and described by a second-order polynomial function as follows:

$$C_p(T) = a \cdot T^2 + b \cdot T + c \tag{2.8}$$

The same is considered to evaluate the density $\rho\left(\frac{kg}{m^3}\right)$ of the flue gas, which has been calculated as a seven-order polynomial function [24]:

$$\rho(T) = a' + b'T + c'T^2 + d'T^3 + e'T^4 + f'T^5 + g'T^6 + h'T^7 \tag{2.9}$$

The dynamic viscosity $\mu\,(Pa \cdot s)$ and the thermal conductivity $k\left(\frac{W}{mK}\right)$ are the same of the air conditions and expressed as function of the temperature [13] :

$$k(T) = 1.0942 \times 10^{-2} + 5.4985 \times 10^{-5} \cdot T - 3.6531 \times 10^{-9} \cdot T^2 \tag{2.10}$$

$$\mu(T) = 7.1902 \times 10^{-6} + 4.1787 \times 10^{-8} \cdot T - 7.09861 \times 10^{-12} \cdot T^2 \qquad (2.11)$$

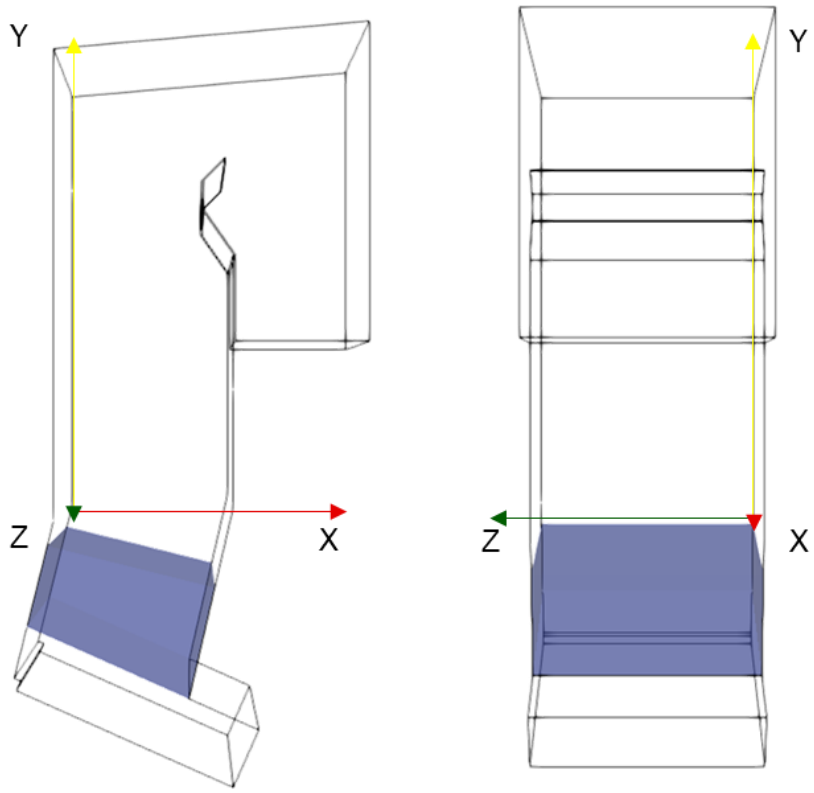

Figure 2.4. Representation of the boundary box for the heat source in the physical domain

- **Reacting CFD model**: the reacting CFD model numerically describes the gaseous combustion of the syngas. As this modeling approach is significantly demanding from the computational point of view, the combustion scheme has been chosen to save computational resources. It is represented by the three chemical equations: the partial methane reduction, the oxidation of carbon monoxide reduction and the shift reaction [25]. The conservation equation for a chemical species takes a general form as follows:

$$\frac{\partial}{\partial x_i}(\rho\, \tilde{u}_i \tilde{y}) = \frac{\partial}{\partial x_i}\left[\frac{\mu_T \partial \tilde{y}}{\sigma_y \partial x_i}\right] + \overline{R}_f \qquad (2.12)$$

where σ_y is the turbulent Schmidt number, $\tilde{y}$ (%) is the mass fraction of the chemical species, $\overline{R}_f \left(\frac{kg \cdot s}{m^3}\right)$ is the mass rate of creation or depletion by chemical reaction, $\rho \left(\frac{kg}{m^3}\right)$ is the density and $\tilde{u}_i \left(\frac{m}{s}\right)$ denotes the velocity component in the i-th direction [26].

The Arrhenius reaction scheme was chosen as a controller for the chemical reaction rate and the reaction parameters were defined through a literature review [25], [27], [28] of the theoretical and experimental chemical processes. According to the Arrhenius equation, the reaction rate constant is given by:

$$k_j = A_j T^{\beta_j} \exp\left(-\frac{E_j}{RT}\right)$$

where A_j represents the pre-exponential constant, β_J is a temperature exponent and E_J is the activation energy of the reaction. A complete description of these reactions and the parameters is available in the following:

$$CH_4 + 1.5O_2 \rightarrow CO + 2H_2O \qquad r_5 = k_5[CH_4]^{0.9}[O_2]^{1.1} \qquad k_5 = 2.0 \times 10^{15} e^{-\frac{35000}{T}} \qquad (2.13)$$

$$CO + \frac{1}{2} O_2 \rightarrow CO_2 \qquad r_6 = k_6[CO][O_2]^{0.5} \qquad k_6 = 2.0 \times 10^{9} e^{-\frac{12000}{T}} \qquad (2.14)$$

$$CO_2 \rightarrow CO + \frac{1}{2} O_2 \qquad r_7 = k_7[CO_2] \qquad k_7 = 8.11 \times 10^{10} e^{-\frac{77100}{T}} \qquad (2.15)$$

Equations (2.13, (2.14 and(2.15 describe the combustion inside the computational domain through the Eddy Dissipation Concept (EDC) combustion scheme imposed in OpenFOAM. The EDC model is based on the assumption that chemical reactions occur in small regions within the turbulent flow (eddies), characterized by high dissipation rates of turbulent kinetic energy, where the reactants are mixed at the molecular level, allowing chemical reactions to proceed. The boundary conditions for the chemical species were defined through the experimental campaign, described in the previous paragraph. The boundary conditions necessary to correctly describe the system, are presented in Table 2.7, in terms of chemical species involved in simplified reactions and temperature, where y_i is the mass fraction of the component i.

Table 2.7. Description of chemical boundary conditions of RDF gasification

	y_{CH_4}	y_{O_2}	y_{CO}	y_{N_2}	y_{H_2O}	y_{CO_2}	y_{H_2}	T
Secondary Inlet	0	0.23	0	0.77	0	0	0	300 K
Primary inlet	0.00018	0.0	0.0874	0.6120	0.1177	0.1782	0.0045	1560 K
Outlet	$\nabla y_i = 0$							$\nabla T = 0$
Walls	$\nabla y_i = 0$							standard wall function

The Eddy Dissipation Concept (EDC) was chosen as the turbulence-chemistry interaction model to allow an optimal compromise between execution time and performance [29].

2.4.3 Mesh Sensitivity Analysis

A grid sensitivity analysis was conducted for both the reacting and non-reacting models, by generating three different computational grids, with their main parameters detailed in Table 2.8.

Table 2.8: Main characteristics of the computational grids employed for the sensitivity analysis

Mesh no.	Number of cells	Non-orthogonality max	Skewness max
1	832,000	63.00	2.02
2	1,764,000	61.85	2.12
3	3,268,000	62.60	1.91

To conduct a comprehensive sensitivity analysis, the cell sizes were reduced uniformly across the entire domain by roughly doubling the number of cells at each refinement step, starting from a sufficient number of cells which was defined through a literature analysis [9], [30], [31]. Special attention was paid to regions near the walls, where the meshes were refined to capture the boundary layer effects accurately, considering that the y^+ was kept under 5 for both mesh 2 and 3. Additionally, the meshes were refined at the secondary inlet sections to precisely detect and analyze the interaction between the hot gases and the incoming cold comburent air. The grids were generated using the advanced meshing algorithm “snappyHexMesh” within the

OpenFOAM framework. This algorithm facilitated the creation of high-quality, hexahedral-dominant meshes that ensured precise representation of the complex geometries involved.

The finest grid was chosen by evaluating the average error according to the following expression:

$$Error(\%) = \sum_{i=1}^{n} \frac{|x_{ref,i} - x_i|}{\bar{x}_{ref}} \% \qquad (2.16)$$

The $x_{ref,i}$ is the variable from the reference grid and x_i are the i-variable of the grid chosen for the sensitivity analysis. The sensitivity analysis has been conducted in terms of temperature and velocity fields, extracting the variables of interest in the same points and zone of interest of the experimental campaign reported in Table 2.2 of Section 2 and the temperature and velocity alongside the fluid dynamic characteristics of the simulated gas. Furthermore, to have a complete evaluation of the grid performance, an extraction of the temperature and velocity was performed at the same height of the Silicon bar (y = 4.64 m) for the complete length of the combustion chamber in the x direction. The results of the comparison are available in Table 2.9. Only the average values of the errors between the reference grid and the analyzed grids are reported in the table, providing a concise overview of the grid performance.

Table 2.9. Sensitivity analysis conducted on the reacting and non-reacting model

		Ceiling Temperature	**Bar Temperature**	**Horizontal Temperature**	**Horizontal Velocity**
Non-reacting	Comparison Mesh 1-3	2.26%	2.97%	2.22%	28.45%
	Comparison Mesh 2-3	0.89%	0.66%	1.54%	0.82%
Reacting	Comparison Mesh 1-3	3.41%	4.21%	3.88%	33.11%
	Comparison Mesh 2-3	1.03%	1.88%	1.37%	2.15%

Due to the critical interaction between the cold air and hot gases at the secondary inlet zone, the temperature and velocity fields show problematic behavior near the wall. The first computational grid chosen for the sensitivity analysis was not refined enough to accurately capture the thermodynamic behavior of the flow within the combustion chamber. This inadequacy is clear from the average errors reported in

Table 2.9. While the grid shows a satisfactory response in terms of temperature comparison, its performance in capturing the velocity field is poor. The average errors between the reference grid and the coarser grids indicate that the initial grid (Mesh 1) fails to adequately resolve the complex flow characteristics and boundary layer interactions.

As shown in the table above, by improving the mesh quality, especially in regions with high gradients and complex flow patterns, the sensitivity analysis ensures a more reliable representation of the physical phenomena. This approach highlights the importance of grid refinement in achieving accurate and dependable simulation results.

As expected, the reacting model shows higher errors due to the complexities introduced by resolving chemical reactions on the computational grid. However, the grids generated for the sensitivity analysis demonstrate strong performance across both the reacting and non-reacting models. Therefore, "Mesh 2", consisting of 1,764,000 cells, was selected for further analysis to balance accuracy. An x-y clipping of the selected grid at the middle section is available in Figure 2.5.

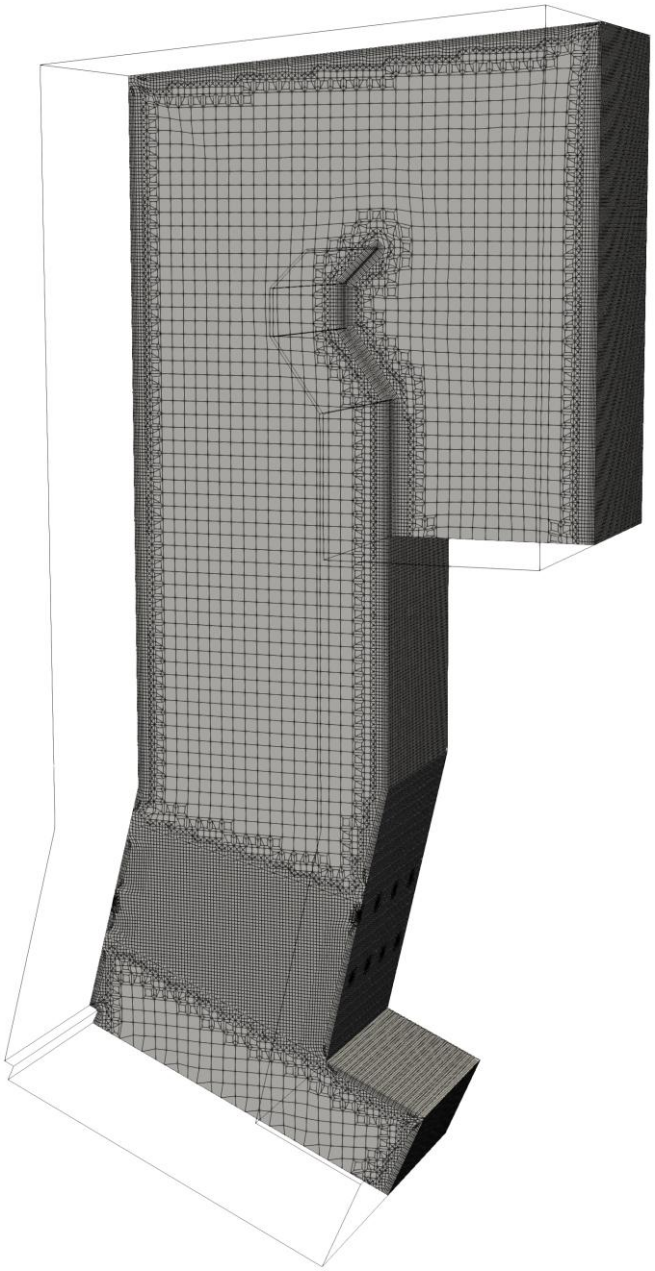

Figure 2.5 Computational grid selected to carry out the numerical simulations, composed of 1,764,000 cells.

2.5 Results and Discussion

The numerical model has been validated through the experimental campaign against the temperature data, collected at six points of the combustion chamber, as described in section 2.4. Although numerical simulations were performed to reproduce

the operating conditions of the plant in the reference period, the results achieved by the three models present different levels of detail.

A comparison between numerical and experimental data is reported in Figure 2.6 and Figure 2.7, together with the measurement uncertainties. Figure 2.6 presents a comparison of temperature profiles within a Waste-to-Energy (WtE) plant registered with the silicon carbide bar, highlighting the differences between experimental measurements and predictions from various numerical simulation models. The experimental data, depicted by black circles with error bars, serve as a reference for evaluating the accuracy of the models. The reacting model, shown as a dash-dot line, initially predicts a rapid temperature increase, which then levels off, following a trend that closely matches the experimental data points. This model seems to capture the dynamic behavior of the combustion process more accurately, reflecting the complex interactions and reactions occurring within the plant. In contrast, the non-reacting model, represented by a dashed line, also predicts an initial rise in temperature but deviates from the experimental results, particularly at lower positions along the Z-axis, indicating potential limitations in accounting for reactive processes or heat transfer mechanisms. The 0D model, illustrated by a solid black line, offers a simplified prediction, maintaining a constant temperature around 1300 K throughout the entire profile. This approach significantly overestimates the temperature compared to both the experimental data and the other models, suggesting that it lacks the necessary detail to accurately represent the varying thermal conditions within the system. The closer alignment of the reacting model with the experimental data highlights its effectiveness in simulating the real conditions of the WtE plant, whereas the discrepancies observed in the non-reacting model and the overly simplified 0D model emphasize the challenges in accurately modeling the thermal and reactive behaviors in such complex systems. This comparison underscores the importance of selecting and refining simulation models to achieve reliable and realistic predictions, which are essential for optimizing plant performance and minimizing environmental impact.

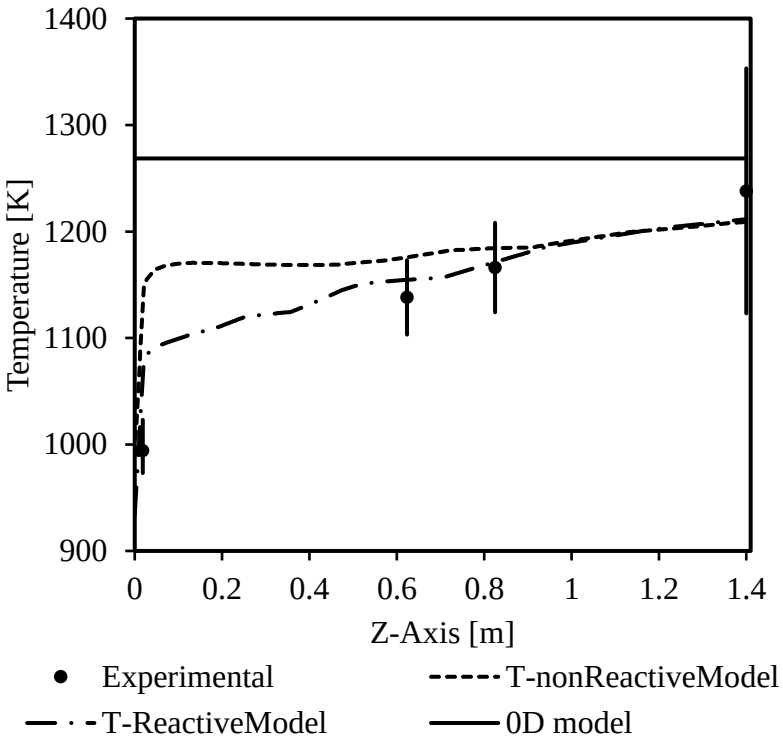

Figure 2.6. Comparison between 0D model, non-reacting model, reacting model, and experimental data at y=4.64m

Table 2.10. Local percentage error on measurement points and average percentage error, on the x-z plane at y=4.64m

	0D model	**Non-reacting CFD model**	**Reacting CFD model**
Point 1 (z = 0.01 m)	27.61%	20.70%	9.20%
Point 2 (z = 0.62 m)	11,46%	4.79%	1.90%
Point 3 (z = 0.825 m)	8,79%	2.11%	0.57%
Point 4 (z = 1.4 m)	2,46%	3.49%	2.76%
Average percentage error	12.58%	7.77%	3.61%

Similar to the previous comparison, Figure 2.7 compares the ceiling temperature predictions from different numerical models with experimental measurements within a Waste-to-Energy (WtE) plant. The experimental data, represented by black circles with error bars, provides a benchmark for evaluating the accuracy of the models. The reacting model, shown as a dash-dot line, predicts an initial rapid increase in

temperature closely aligning with the experimental data points, particularly at higher positions along the Z-axis. This model appears to effectively capture the complex reactive processes that influence the ceiling temperature, offering a realistic representation of the thermal environment within the plant. In contrast, the non-reacting model, depicted by a dotted line, also shows an initial temperature rise but generally underestimates the ceiling temperature compared to both the reacting model and the experimental data, especially in the mid-range of the Z-axis. This suggests that the non-reacting model may not fully account for the reactive dynamics and heat transfer mechanisms that are critical in this context. The 0D model, represented by a solid line, predicts a constant temperature just above 1100 K throughout the entire profile, which, while slightly closer to the experimental data than in some other comparisons, still fails to capture the nuanced variations observed experimentally. The 0D model's oversimplified approach results in a less accurate representation of the temperature profile, missing key details that are evident in the experimental data.

The overall comparison underscores the effectiveness of the reacting model in simulating the actual conditions within the WtE plant, as it more closely follows the experimental measurements, while the non-reacting model and the 0D model show significant discrepancies. These differences highlight the importance of using detailed reactive models to accurately predict the thermal behavior in such systems, as they are crucial for optimizing plant operation and ensuring compliance with environmental regulations.

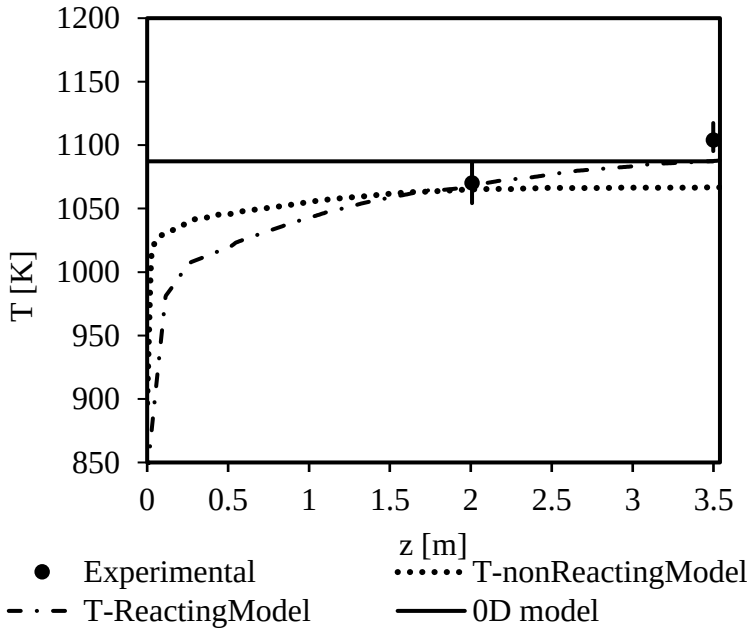

Figure 2.7. Comparison between 0D model, non-reacting model and reacting model and experimental data at y=13.47 m.

Table 2.11. Local percentage error on measurement points and average percentage error

Conv	**0D model**	**Non-Reacting Model**	**Reacting Model**
Point 5 (z = 2.00 m)	1.56%	1.21%	0.66%
Point 6 (z=3.50 m)	1.53%	4.50%	1.51%
Average percentage error	1.55%	2.85%	1.09%

The average error is reported in Table 2.11. A visual comparison of the temperature and the velocity field is available in Figure 2.8 and Figure 2.9. In the first one, while the left field is much more uniform, the right field presents an extremely high temperature in correspondence with the secondary inlet zone, which represents the ignition point of the combustion. Differently, in the second one, the non-reacting field presents a much more crushed profile on the wall of the combustion chamber, considering that the combustion generates an intense turbulent condition which significantly affects the velocity field of the application.

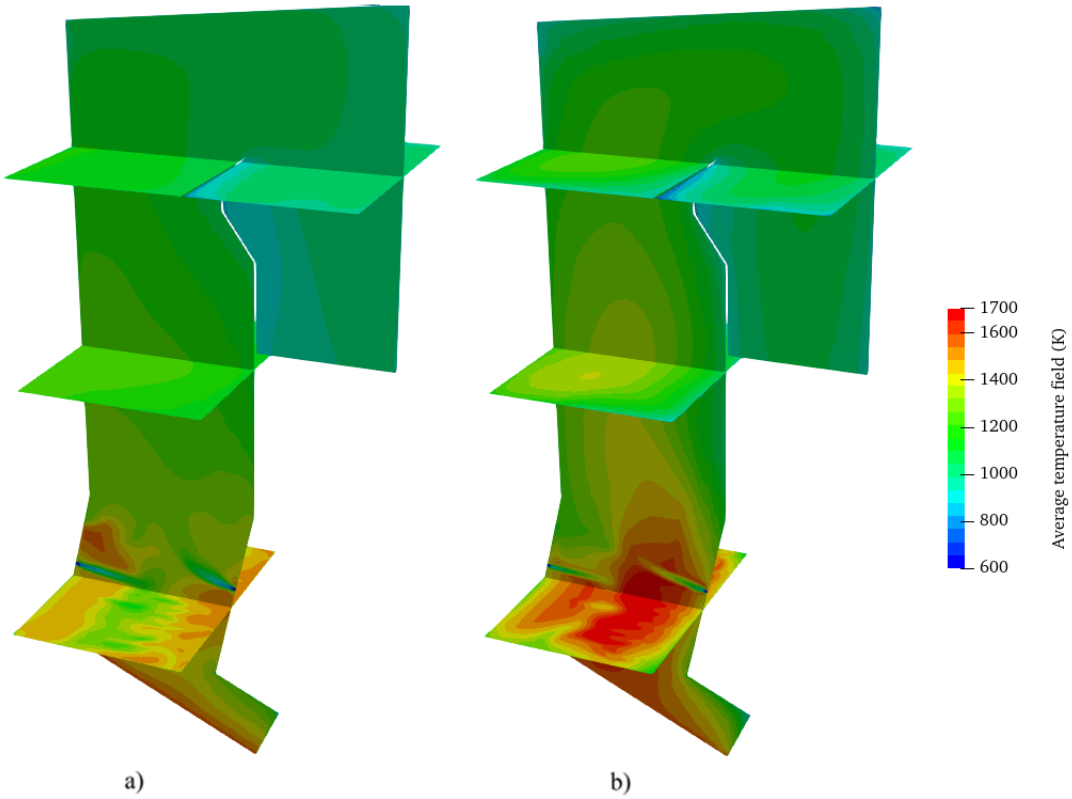

Figure 2.8. Representation of the average temperature field obtained with a) non-reacting model, b) reacting model.

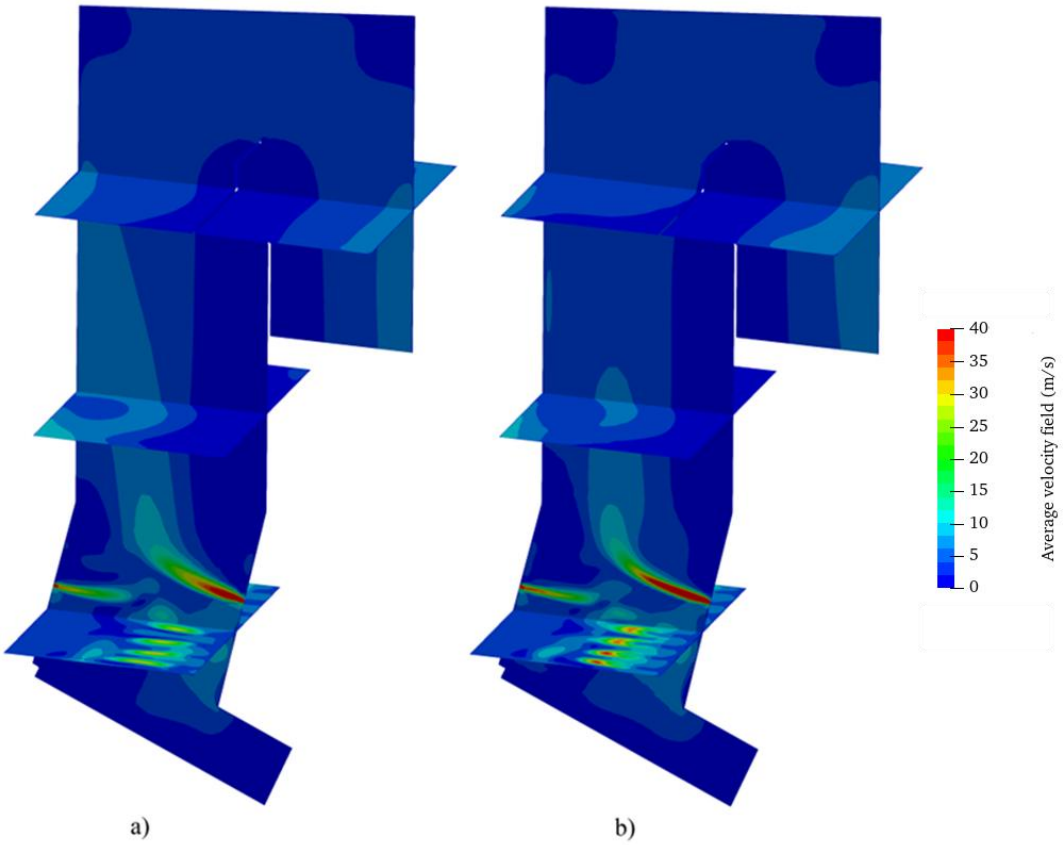

Figure 2.9. Representation of the average velocity field of the two CFD simulations, a) non-reacting field, b) reacting field.

The proposed thermodynamic models have been applied to the description of the combustion chamber operating conditions. Waste-to-energy plants have very strict regulations on operating conditions and exhaust gases at outlet sections. Limitations are imposed in terms of exhaust residence temperature after 2 seconds from the last comburent air injection, T_{2S}, and have been defined to avoid the emission of dioxins into the atmosphere. This temperature has been evaluated employing the three modelling approaches discussed in this paper. In particular, while the temperature distribution has been assumed one-dimensional with the thermodynamic model, to numerically evaluate the T_{2S} temperature with 3D CFD simulations, fluid particles have been followed in the combustion chamber, to get the position and the distribution after 2 seconds from the last secondary air injection plane.

The difference between non-reacting and reacting 3D CFD models resides in the thermodynamic properties of the fluid inside the combustion chamber. While exhaust composition is assumed to be constant with the non-reacting CFD model, thermodynamic properties locally depend on composition when the reacting 3D CFD model is employed. This provides a significant difference in the spatial distribution of the fluid particles as it can be observed in Figure 2.10 and Figure 2.11, which shows the distribution of selected fluid particles in the combustion chamber two seconds after the last air intake.

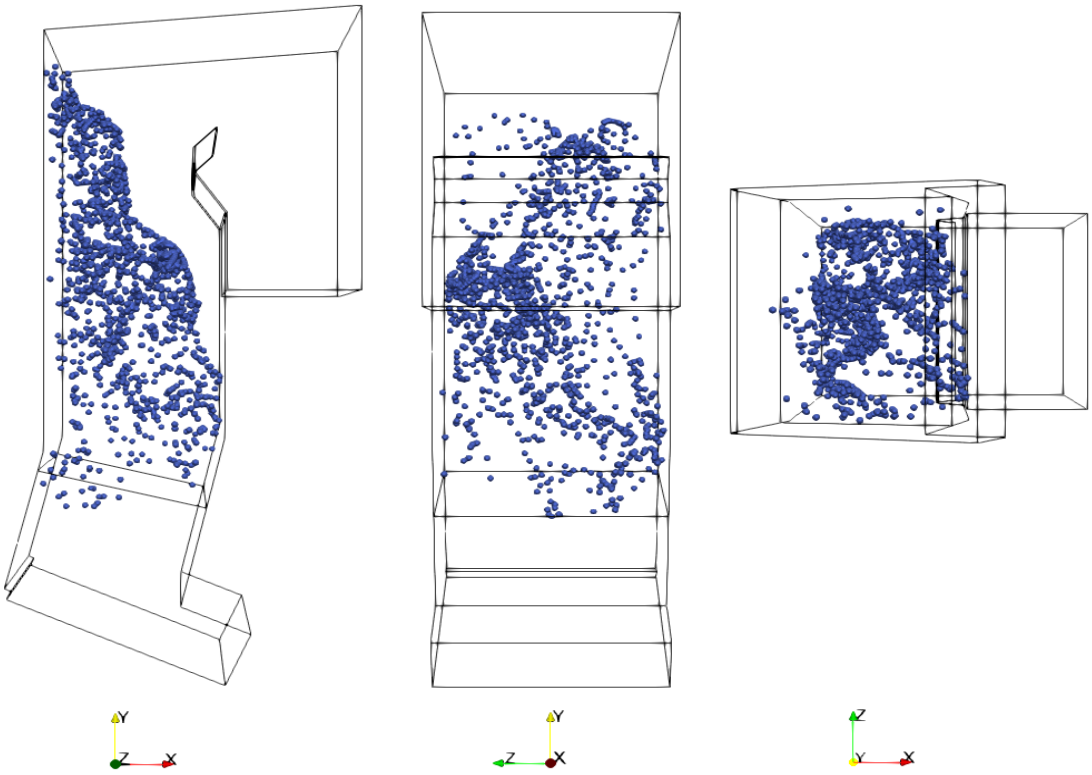

Figure 2.10: Distribution of selected fluid particles in the combustion chamber two seconds after the last air intake for the non-reacting CFD model.

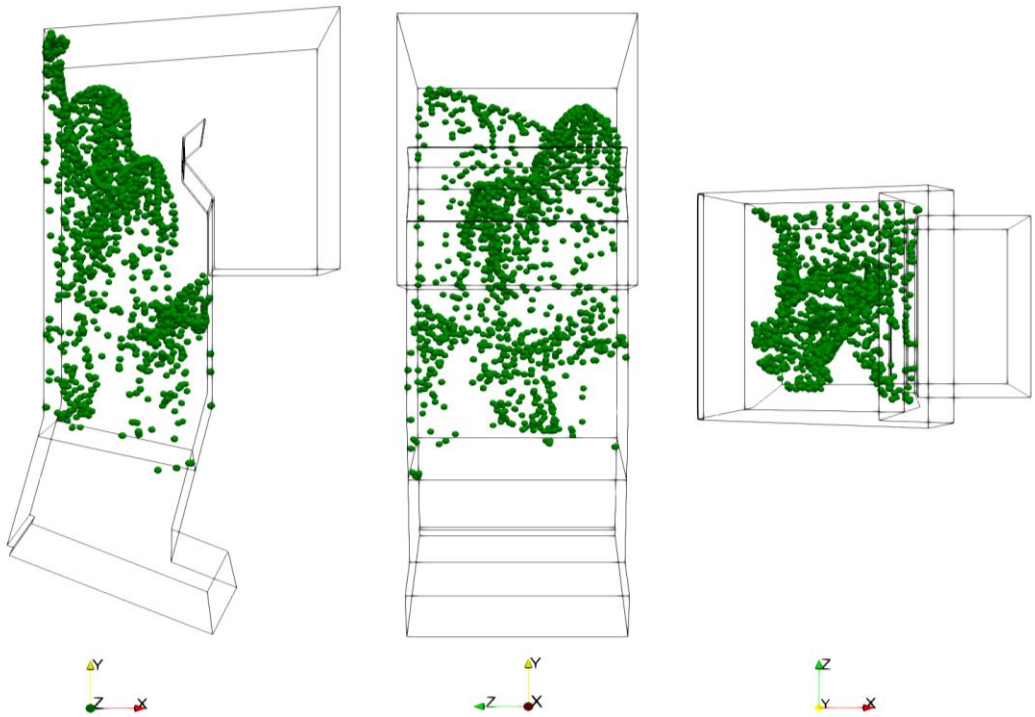

Figure 2.11: Distribution of selected fluid particles in the combustion chamber two seconds after the last air intake for the reacting CFD model.

The two figures show a modest difference in the centre zone, in which the distribution of particles seems to be moved upward for the reacting model, as can be seen from the y-z cut in the centre of the two figures. The T_{2S} temperature is evaluated as the average temperature after two seconds from the last air intake. A comparison among the three models in terms of calculated T_{2S} temperature is presented in Table 2.12.

Table 2.12: Comparison of average T_{2S} temperature predicted with the three different numerical models.

Model	T_{2S} temperature (K)
0D	1256.7
Non-reacting	1162.8
Reacting	1211.5

The comparison of the three results highlights the capability of the numerical models to predict the temperature of the particles after two seconds from the ignition point. The Table 2.12 can be summarized as follows:

- The lumped parameter model (0D) consistently demonstrates the highest temperature compared to the other models, as it is founded upon the resolution

of the global chemical reaction outlined in section 3. When considering solely the chemical resolution of the global reaction, the thermodynamic equilibrium given by the conservation of the chemical species defines a significantly elevated temperature;

- The reacting-model registers a temperature T2s between the 0D model and the non-reacting model because it considers the resolution of the local combustion in the computational domain, but at the same time the products of the combustion are transported inside the combustion chamber and are affected by the global transport;
- The non-reacting model shows the lowest temperature T2s in the comparison since an equivalent heat power (as a source term) is imposed in the secondary air inlet zone. In particular, by avoiding the combustion of the chemical reagents, a lower local temperature is registered, as reported in the comparison in Figure 2.8. For the same reason depicted for the reacting model, the particles are affected by the same transport effect and consequently to a drop of the temperature after two seconds in the chamber.

2.6 Conclusions

This study presents a detailed evaluation of numerical strategies for modeling a Waste-to-Energy (WtE) plant, comparing a 0D lumped parameters model with two distinct Computational Fluid Dynamics (CFD) approaches. The primary aim was to assess the strengths and limitations of each model, highlighting their applicability for different analytical purposes. The 0D lumped parameters model proved to be an effective compromise between computational efficiency and reliability, particularly for situations where only a general temperature estimate is required without the need for detailed thermodynamic fields. This model is well-suited for scenarios with limited computational resources, offering quick, indicative results. It is based on balance equations for thermodynamic variables and assumes chemical equilibrium between species, without relying on empirical or semi-empirical correlations. Additionally, this thermodynamic model can define input parameters for a more detailed, non-reacting 3D CFD simulation of the combustion chamber's first vertical channel, showcasing its versatility in connecting simplified and advanced analyses.

An experimental campaign, lasting four days, was conducted to determine the chemical composition of Refuse-Derived Fuel (RDF) and measure the temperature within the combustion chamber at six different points. This experimental data provided

a critical benchmark for validating the numerical models. The combustion temperatures predicted by the models were compared with measurements taken at various heights within the chamber, ensuring a thorough validation process. A comprehensive comparison of the three numerical approaches—ranging from the simplest lumped parameters model to the more complex reacting CFD model—was performed. The results confirm that each model is capable of effectively predicting and analyzing temperature distributions within the combustion chamber.

The analysis highlights that both the lumped parameters model and CFD approaches are valuable tools for evaluating complex processes in WtE plant combustion chambers, with the choice of model largely dependent on the specific research goals. While the 0D model may slightly overestimate temperatures and lacks detailed fluid dynamics information, its low computational demands and fast execution make it ideal for preliminary assessments. On the other hand, the non-reacting and reacting CFD models, though more computationally intensive, offer detailed insights into fluid behaviour and chemical reactions within the combustion chamber, making them essential for thorough performance evaluations and optimization.

From a sustainability perspective, WtE plants play a critical role in reducing landfill use and converting waste into usable energy, contributing to circular economy initiatives. Efficient WtE operations can help reduce greenhouse gas emissions from waste disposal while recovering energy and reducing reliance on fossil fuels. In this context, the use of modelling tools such as CFD and lumped parameter models can significantly improve the sustainability of WtE processes. By enabling more accurate and efficient designs, these models help optimize combustion efficiency, reduce emissions, and improve energy recovery, all of which are key to enhancing the environmental performance of WtE facilities.

The lumped parameters model, with its low computational requirements, supports rapid assessments and early-stage decision-making, helping engineers design more sustainable systems without the need for high energy and resource expenditure in complex simulations. CFD models, despite being more resource-intensive, offer deep insights into fluid dynamics and chemical processes that can lead to more precise control over combustion, enabling the reduction of pollutants such as NOx and particulate matter. By refining the combustion process, CFD simulations can contribute to minimizing environmental impact and maximizing energy recovery efficiency.

In conclusion, this study underscores the importance of selecting the appropriate modelling approach for the efficient analysis of WtE plants. Integrating both lumped

parameters and CFD models allows us to balance computational efficiency with detailed insights, supporting the development of more sustainable WtE systems. As these tools advance, they will continue to play a crucial role in optimizing plant operations, reducing emissions, and improving the overall sustainability of energy-from-waste technologies.

CHAPTER 3. Metrological system for a sustainable transport sector

3.1 Introduction

Monitoring energy usage and accurately accounting for energy consumption are vital for advancing the Sustainable Development Goals (SDGs), particularly those related to affordable and clean energy (SDG 7), sustainable cities and communities (SDG 11), and climate action (SDG 13). Precise metering enables effective energy utilization, aids in understanding consumption patterns, and identifies opportunities for conservation and cost efficiency. Energy accounting, on the other hand, provides a structured approach to measuring, reporting, and managing energy performance, allowing governments, businesses, and communities to make well-informed decisions regarding energy efficiency and the adoption of renewable energy sources. By combining these practices, it becomes possible to reduce carbon footprints, promote sustainability, and contribute to global efforts to combat climate change.

In recent years, there has been remarkable progress across various industries, driven by economic and environmental policies. One sector that has experienced rapid transformation is transportation, largely due to the increasing use of eco-friendly fuels. This shift has created the need for new approaches and techniques in the field of metrology to effectively handle the unique characteristics of green fuels. Evaluating the current state of metrology is crucial, as precise metering and emissions accounting are essential for monitoring progress and assessing the impact of these changes.

To address these needs, a comprehensive analysis of flowmeter performance in the transportation and maritime sector has been conducted. Currently, a variety of flowmeters, such as orifice plate flowmeters, are widely employed due to their simplicity, adaptability, reliability, and cost-effectiveness. While these devices are suitable for general engineering applications, they may not always provide the accuracy required for the transport sector's evolving needs, especially in measuring green fuels. The quality of these measurements directly impacts the efficiency of new engines in passenger cars, trucks, and ferries. Flowmeters traditionally used in the

transport sector often fall short in this context, as green fuels present unique challenges due to their varying properties and flow rates[32].

In transportation and naval operations, integrating advanced flowmeters and energy accounting systems is crucial for enhancing energy efficiency and sustainability. Flowmeters, which measure the rate of liquid or gas flow, are indispensable for monitoring fuel consumption, emissions, and operational efficiency in vehicles, aircraft, and ships [33]. For example, in aviation, flowmeters provide real-time data on fuel usage, enabling airlines to optimize flight routes, reduce fuel burn, and lower greenhouse gas emissions [33]. Similarly, in maritime operations, flowmeters help monitor fuel flow in vessels, from small boats to large cargo ships, allowing operators to minimize waste, optimize engine performance, and comply with international emissions standards. Energy accounting within these sectors involves the methodical gathering, examination, and reporting of energy consumption data, integrating information from flowmeters and other monitoring tools [34]. This process enables transportation and naval operators to understand energy consumption patterns, identify inefficiencies, and develop targeted strategies to reduce energy use and emissions. For example, in the shipping industry, energy accounting can reveal trends in fuel consumption that may indicate inefficiencies in voyage planning or engine operation, prompting corrective actions that lead to significant fuel savings and reduced carbon emissions. As green fuels become more prevalent, special attention must be given to flowmeters' ability to accurately measure highly variable flow rates [34].

By combining the precision of advanced flowmeters with strategic insights from energy accounting, the transportation and naval sectors can achieve substantial progress toward sustainability. These practices not only support the achievement of the SDGs but also enhance operational efficiency, reduce costs, and bolster global efforts to combat climate change by adopting cleaner, more efficient technologies and practices.

A CFD numerical model has been developed and rigorously tested to evaluate the performance of an orifice plate flowmeter. This three-dimensional model has been employed as part of the European 20IND13 SAFEST project (SAFEST - EMPIR) to provide a comprehensive analysis of the interaction between the test liquid and the flowmeter, and to perform a sensitivity analysis on critical quantities of interest, such as pressure drop, velocity distribution, and turbulence effects. The primary objective of the present work is to assess the feasibility and importance of integrating advanced numerical techniques into the metrological sector as a strategic approach to enhance

measurement accuracy, reliability, and adaptability to new challenges, particularly in light of the growing adoption of eco-friendly fuels.

Integrating computational fluid dynamics (CFD) modelling within metrology offers several benefits. First, it enables the detailed visualization and understanding of complex flow patterns and phenomena that occur within and around the flowmeter, which are often difficult to capture through experimental methods alone. This deeper understanding facilitates the optimization of flowmeter design, allowing for more precise measurements under various operating conditions. Additionally, CFD simulations help identify and quantify the influence of different parameters—such as fluid viscosity, temperature, and flow rate variability—on measurement accuracy, which is especially important when dealing with the unique properties of green fuels that can exhibit significantly different behaviours from conventional fuels. Moreover, the use of numerical modelling tools such as CFD in metrology reduces the dependence on extensive and costly physical testing by allowing a virtual assessment of multiple scenarios, including extreme conditions that are hard to replicate in laboratory environments. This can significantly accelerate the development of new flowmeter technologies and improve their adaptability to a broader range of applications, including those in the transportation and naval sectors. By leveraging these advanced techniques, the metrological community can better address the challenges posed by the transition to sustainable energy sources, ensure compliance with international standards, and contribute to the broader goals of sustainability, efficiency, and innovation. The outcomes of this work highlight the transformative potential of integrating numerical modelling with traditional measurement approaches to meet the evolving demands of modern industry and environmental policy.

3.2 Case study

This paragraph has been divided into two distinct sections, the first one outlines an experimental campaign conducted in collaboration with several National Metrology Institutes (NMIs) as part of a European research project aimed at improving the accuracy of flow measurements in power plants. This campaign involved testing an orifice plate flowmeter across a range of temperatures and flow conditions to understand the effects of installation and flow disturbances on measurement accuracy. Advanced measurement techniques, such as Laser Doppler Velocimetry (LDV), were used to ensure fully developed flow conditions and validate the experimental results.

The second section discusses the development and validation of a computational fluid dynamics (CFD) model to support and enhance the findings of the experimental campaign. The CFD model was designed to simulate the flow behaviour around the orifice plate, providing detailed insights into fluid dynamics, such as turbulence and pressure variations.

3.2.1 Experimental Campaign

The experimental campaign focused on developing and validating a model for the discharge coefficient of an orifice plate over various temperatures and Reynolds numbers. This experimental study was conducted under the European research project JRP "Metrology for Improved Power Plant Efficiency," and involved several National Metrology Institutes (NMIs), including Physikalisch-Technische Bundesanstalt (PTB), Sveriges Tekniska (SP) and Danish Technological Institute (DTI). The investigated case study focuses on a single-hole orifice plate flowmeter installed in a DN 100 (100 mm nominal diameter) pipe, which is commonly used in industrial flow measurement applications. These experiments involved varying flow rates, fluid types,

and operational conditions to ensure the model's robustness and accuracy in simulating actual flow behaviour. A representation of the power plant is available in Figure 3.1.

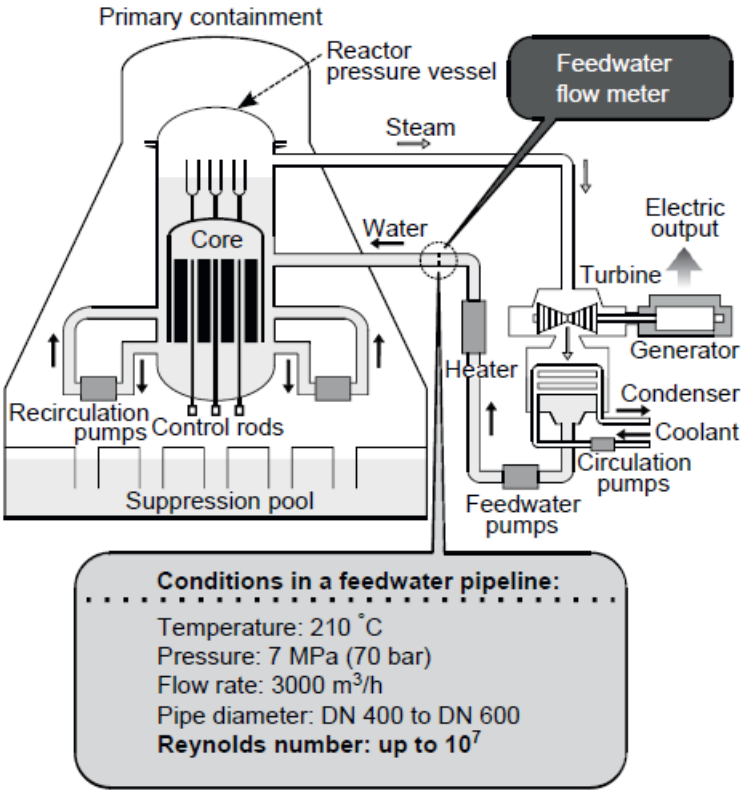

Figure 3.1. Sketch of the power plant used as reference in the experimental campaign.

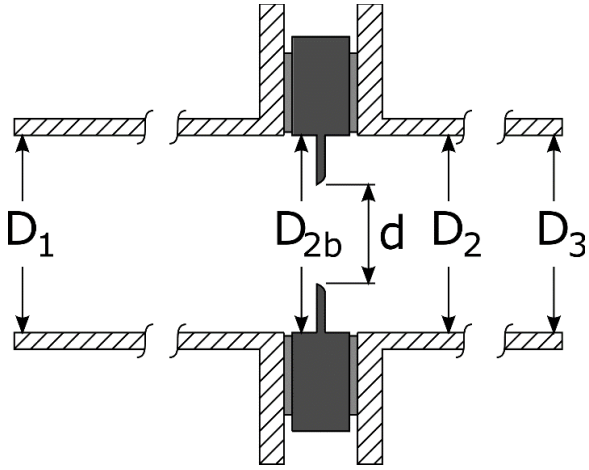

Figure 3.2 Nominal and measured diameters(mm) of the orifice plate–with a sharp edge, an annular chamber and corner tappings – and the resulting value of the diameter ratio

Differential pressure (DP) flowmeters, including orifice flowmeters, operate on the principle of Bernoulli, which states that the flow rate of a fluid is proportional to the square root of the pressure drop across a restriction, assuming steady flow and the conservation of energy. The flow rate is directly correlated to the differential pressure measured between the upstream and downstream sides of the orifice, as well as to the fluid's physical properties, such as temperature, density, and viscosity. Accurate flow measurement using orifice plates is governed by the guidelines provided in the International Standard ISO 5167 Part 2, which defines the geometric specifications, installation procedures, operating conditions, and metrological standards necessary for precise flow measurements. Since the diameter is essential for the evaluation of the discharge coefficient, the orifice plate was measured at various location across the diameter with a micrometer caliber in the experimental campaign conducted by the Technical Research Institute of Sweden (SP).

Table 3.1 Geometrical parameters of the single-hole orifice plate flowmeter

Geometrical parameter	Nominal	Measured
Orifice diameter, d (mm)	51.13	51.13
Pipe diameter, D_1 (mm)	102.26	101.84
Anular chamber diameter, D_{2b} (mm)	102.26	102.26
Pipe diameter D_2 (mm)	102.26	103.49
Pipe diameter , D_3 (mm)	102.26	102.28
Diameter ratio, β (/)	0.5	0.494

The mass flow rate $\boldsymbol{q_m}$ (kg/s) through an orifice plate can be determined using the following equation:

$$q_m = \frac{C \cdot \varepsilon \cdot \pi \cdot d^2 \cdot \sqrt{2 \cdot \Delta p \cdot \rho}}{4 \cdot \sqrt{1 - \beta^4}} \qquad (3.1)$$

where:

- **C** is the discharge coefficient (dimensionless), which depends on the Reynolds number and is calculated using the Reader-Harris/Gallagher (RHG) equation.
- **ε** is the expansibility factor (dimensionless), accounting for the compressibility of the fluid and provided by the second Reader-Harris equation.
- **d** (m) is the diameter of the orifice.
- **Δp** (Pa) is the differential pressure across the orifice.
- **ρ** (kg/m³) is the density of the fluid.

- **β** (dimensionless) is the diameter ratio, defined as the ratio of the orifice diameter to the pipe's internal diameter.

The discharge coefficient (C) and expansibility factor (ε) are crucial for accurately calculating flow rate. The discharge coefficient considers flow profile, pipe roughness, and Reynolds number effects, while the expansibility factor adjusts for the fluid's slight compressibility. The ISO 5167 standard offers detailed empirical correlations, such as the Reader-Harris/Gallagher (RHG) equation [35], to determine these parameters using extensive experimental data across various flow conditions. Research indicates that upstream and downstream disturbances, changes in flow regime, and fluid properties can significantly affect orifice flowmeter accuracy. Studies have also highlighted the importance of proper installation and calibration to minimize measurement errors and ensure compliance with international standards [36].

This experimental campaign was used as a reference for validating the developed numerical model; to this scope, just the measurements of the undisturbed flow scenario were considered. A representation of the flow meter and the expected velocity profile are reported in Figure 3.3:

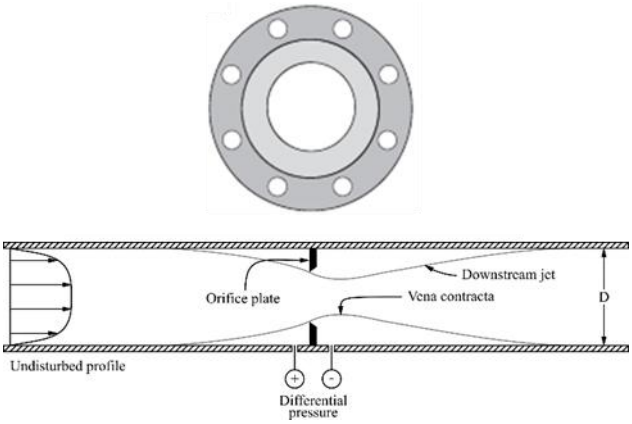

Figure 3.3. Overview of the orifice plate simulated (undisturbed flow).

Table 3.2 Fixed test plan including the resulting flow rates for Reynolds number $Re_D = 5 \cdot 10^5$

Dimension	Value
Temperature (°C)	20
Kinematic Viscosity ($x10^{-6}$ m^2 s^{-1})	1.0048
Flow rate (m^3 h^{-1})	14.5
Density (kg m^{-3})	998.23

The establishment of a fully developed flow profile is crucial for ensuring the comparability of flow measurements and validating the Reynolds number theory. To

achieve this, all participating National Metrology Institutes (NMIs) measured the undisturbed axial flow profile (primary component) at a standard temperature of 20°C. Additionally, it was confirmed that the maximum swirl angle of the secondary flow components remained below 21 degrees for the undisturbed flow profile at this temperature. This verification was facilitated by the use of an innovative Laser Doppler Velocimetry (LDV) window chamber, which allows for the measurement of the complete velocity profile, including all three flow components, across the entire cross-section of the pipe. The measured profiles were then compared against theoretical profiles, which are primarily based on empirical data, to ensure accuracy and consistency. To quantify the secondary velocities within the flow, the maximum swirl angle is used, as defined by Yeh and Mattingly [37] to measure the deviation of the secondary flow vector from the axial flow direction (primary component) [38]. The maximum swirl angle is calculated using the formula:

$$\phi_{MAX} = \arctan\left(\frac{|v|_{MAX}}{w_{vol}}\right) \qquad (3.2)$$

where $|v|_{MAX}$ represents the maximum magnitude velocity and w_{vol} is defined as the volumetric friction velocity.

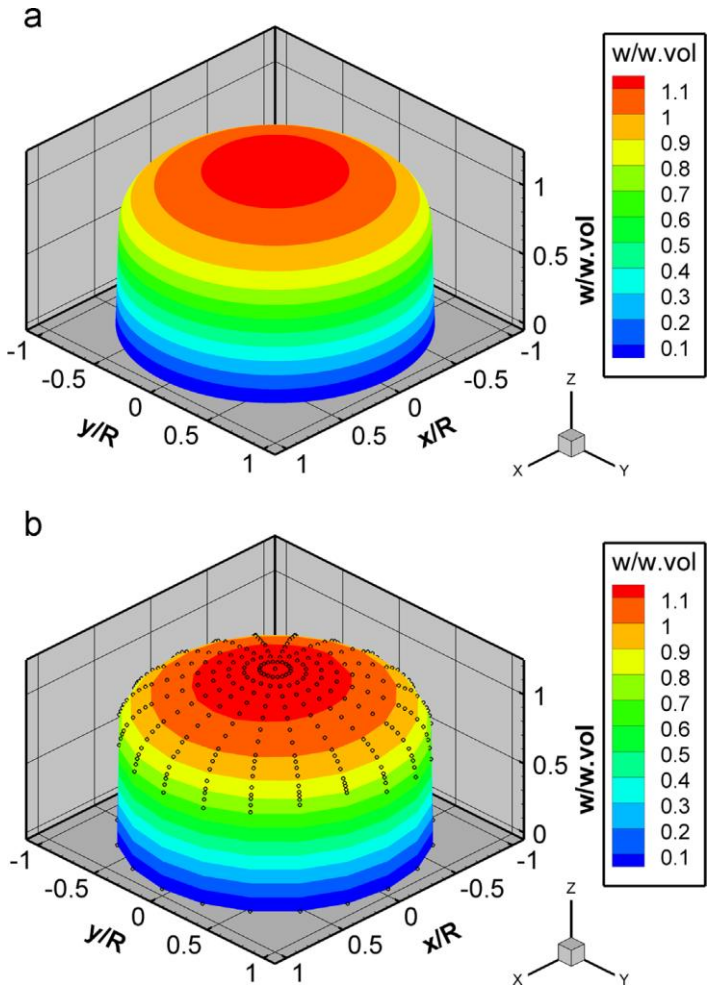

Figure 3.4 Comparison of the calculated and the measured velocity profile for $Re_D = 5 \cdot 10^5$at temperature of 20°C. (a) Calculated velocity profile.(b)Measured velocity profile including the measuring grid

The aim is to establish acceptable ranges or maximum thresholds for these flow indicators to characterize the velocity profile better. If the calculated flow indicators fall within these predefined limits, the flow can be considered to have a sufficiently developed turbulent profile. When dealing with parameters such as swirl and turbulence intensity in flow sensors, setting maximum values for the swirl angle and turbulence factor is common practice. However, determining the acceptable ranges for these parameters can be quite challenging due to the lack of established experience or guidelines in the field. In the context of flow sensors based on differential pressure measurement, specific requirements for acceptable flow conditions are detailed in ISO 5167. According to this standard, it is specified that the maximum deviation of the local axial velocity should not exceed 5% of the maximum local axial velocity of a fully developed, swirl-free flow profile after a 100-pipe diameter (D) inlet. This means

that there are clear guidelines to follow in order to ensure accurate and reliable flow measurements. The swirl angle should be less than or equal to 21 degrees.

3.2.2 Numerical model

A three-dimensional CFD numerical model was developed in the OpenFOAM environment using the pimpleFoam solver. The velocity and pressure fields in the computational domain were predicted by solving the mass and momentum equations under the assumption of three-dimensional, unsteady, turbulent, and incompressible flow (the governing equations are reported in Appendix A). The Unsteady Reynolds-averaged Navier-Stokes (URANS) [39] approach was employed to evaluate the performance of the flowmeter and the Shear Stress Transport (SST) k-ω [40] turbulence model was chosen as the most suitable model after a turbulence model sensitivity analysis , for predicting the velocity and pressure whithin the computational domain. Following the methodology proposed by Arpino et al. [30], the time step was controlled by evaluating the Courant number Co, which is reported in equation (3.3) for a mono-dimensional case.

$$Co = \frac{|u|\Delta\theta}{\Delta H} \tag{3.3}$$

where $|u|$ is the magnitude velocity of the flow (m/s), $\Delta\theta$ is the time step (s), and ΔH is the characteristic size of the mesh cell (m). Following the equation above-mentioned, once the grid dimension and the velocity of the case are fixed in the pre-processing phase, the time step is controlled then by the chosen Courant number. The implicit scheme resolution was chosen to perform the transient resolution of the numerical simulation. Furthermore, given that a 1% variation between Co = 1 and Co=2 [30], a larger value of the Courant number has been chosen to have a good balance between the results and processing time. Since the flow is fully turbulent, due to the restriction effect in the duct and the tested high flow rate in the scenarios, the analysis of the numerical results and the mesh sensitivity have been conducted related to time-averaged velocity and pressure fields. The analysis to establish the proper averaging time interval has also been performed by monitoring the time evolution of the magnitude velocity in two points of interest, which corresponded with the pressure taps. An extensive evaluation of the averaging field is reported in and Figure 3.6.

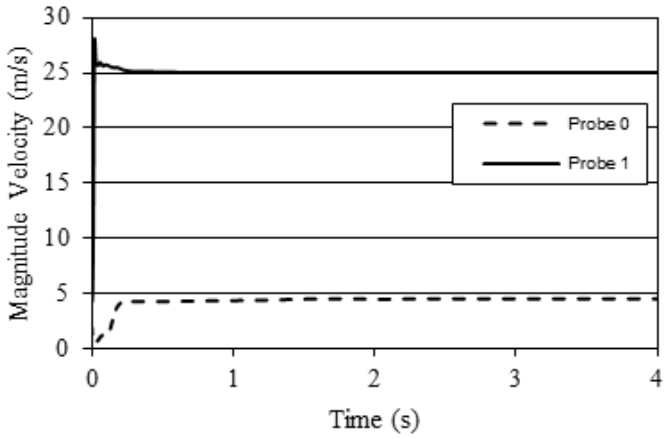

Figure 3.5. Progressive time-average evaluation of the velocity field employing the chosen computational domain

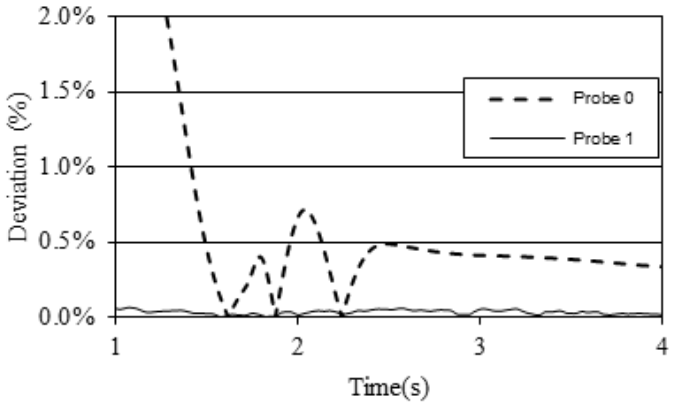

Figure 3.6. Percentage deviation of progressive average up to a given time level of 1% employing the Mesh 2.

As illustrated in Figure 3.6, the deviation from the median value drops below 1% after two seconds of simulation. Consequently, the average field utilized to assess the efficacy of the numerical model has been calculated from the second of processing, until the convergence of the residuals. The coordinates of the two points are available in Table 3.3**Error! Reference source not found.** and presented in Figure 3.7:

Table 3.3. Extraction points for the time-averaging analysis.

Points	Coordinate (m)
Probe 0	(-0.10226, 0, 0)
Probe 1	(0.05113, 0, 0)

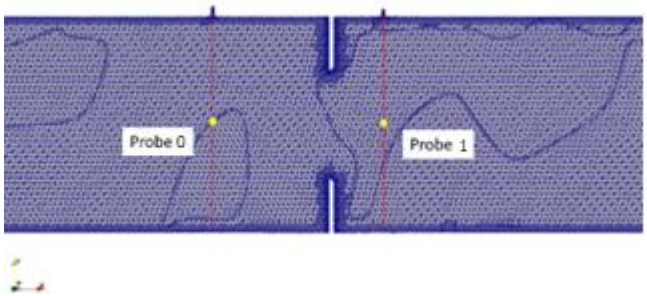

Figure 3.7. Location of the probes in the computational domain.

The grid, composed of 2.21 x 10^6 cells and determined based on a comprehensive mesh sensitivity analysis, was generated by using the OpenFOAM utility "snappyHexMesh" and refined by the orifice plate, where the location of the primary turbulent effects are located. Three computational grids were considered for the mesh independence analysis, whose main parameters are reported in Table 3.4.

Table 3.4. Details of the computational domains used in the sensitivity analysis

	Number of cells (x 10^6)	Max Skewness	Non-Orthogonality
Mesh 1	1.06	3.1	59.98
Mesh 2	2.21	3.1	59.98
Mesh 3	4.87	3.0	59.98

In 3D CFD, the choice of maximum skewness and non-orthogonality directly impacts simulation accuracy, stability, and convergence. Skewness measures how far a mesh cell deviates from an ideal shape, with lower values being critical to reduce interpolation errors and numerical diffusion. For most solvers, maximum skewness is ideally kept below 0.85, as higher values can lead to instability. Non-orthogonality represents the deviation of face normals from being perpendicular to the line connecting cell centers. It affects the calculation of fluxes and gradients, with values below 45° generally being manageable, though corrections are needed above this range. Complex geometries require a balance between these metrics, often achieved through refined meshing and solver adjustments to handle higher deviations. Proper control ensures better convergence and reliable results in simulations. The sensitivity analysis has been conducted by approximately doubling the cell size domain at each refinement step, from the coarsest (Mesh 1) to the finest (Mesh 3).

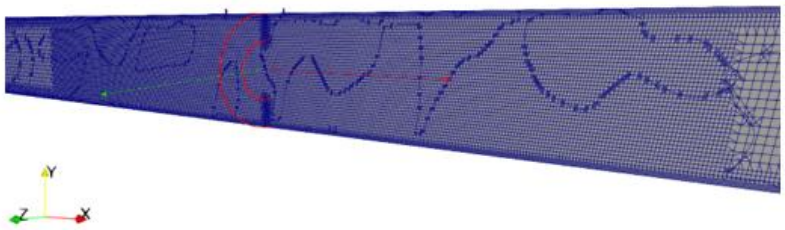

Figure 3.8. Clipping plane in x-y of the computational domain at z=0 (m).

An x-z clipping of the selected computational grid for the numerical simulation is presented in Figure 3.8. As previously stated in the ISO Standard 5167 Part 2, the pressure taps are located one diameter upstream and a half diameter downstream to the orifice plate to capture accurately the differential pressure across the section [41]. The comparison of the velocity and pressure profile has been conducted in the aforementioned sections. A comparison of the differential pressure and discharge coefficient is presented in Table 3.5.

Table 3.5. Sensitivity analysis of the computational grid considering the mesh 3 as a reference for the analysis.

	Differential Pressure (Pa)	**Discharge Coefficient**	**Average Error (%)**
Mesh 1	123,755	0.6410	5.1
Mesh 2	119,124	0.6157	1.4
Mesh 3	117,612	0.6091	/

The sensitivity analysis was carried out using Mesh 3 as the reference. Mesh 3 is the densest and most precise of the three computational domains that were tested. Table 3.5 shows that Mesh 1 is not dense enough to precisely capture the phenomena. It displays an average error of 5.1% for both the differential pressure and discharge coefficient. On the other hand, Mesh 2 shows a lower average error than Mesh 1 for both tested quantities.

The boundary conditions utilized for the numerical investigations are presented in Table 3.6 for the k and ω characteristics of the turbulence model and from Table 3.7 to Table 3.9, in terms of velocity and pressure for all the boundaries of the computational domain.

Table 3.6. Boundary conditions set for numerical model validation (k- ω model).

	k	**ω**

Inlet	I = 0.1	l = 0.007 m
Walls	standard wall functions	standard wall functions
Outlet	∇k = 0	∇ ω = 0

Table 3.7. Boundary conditions for the velocity and pressure coupling in case of scenario 1.

Scenario 1		
	Velocity (m/s)	**Pressure (Pa)**
Inlet	(0.489 0 0)	∇p = 0
Walls	(0 0 0)	∇p = 0
Outlet	∇v = 0	p = 0

Table 3.8. Boundary conditions for the velocity and pressure coupling in the case of scenario 2.

Scenario 2		
	Velocity (m/s)	**Pressure (Pa)**
Inlet	(2.456 0 0)	∇p = 0
Walls	(0 0 0)	∇p = 0
Outlet	∇v = 0	p = 0

Table 3.9. Boundary conditions for the velocity and pressure coupling in the case of scenario 3.

Scenario 3		
	Velocity (m/s)	**Pressure (Pa)**
Inlet	(3.912 0 0)	∇p = 0
Walls	(0 0 0)	∇p = 0
Outlet	∇v = 0	p = 0

In particular, I represents the turbulence intensity at the inlet, l denotes the mixing length calculated as l = 0.07 x L (where L (m) is the diameter of the pipe), v (m/s) signifies the velocity, p (Pa) denotes the pressure, k (m^2/s^{-2}) represents the turbulent kinetic energy and ω (m^2/s^{-3}) denotes the turbulent dissipation rate.

3.3 Results and Discussion

This section is divided into two parts. The first part focuses on validating the numerical model using experimental data.

1. The validation process has been realized using water as a test liquid, collaborating with the Technical Research Institute of Sweden, which furnished the experimental data of the orifice plate.
2. The validated numerical model has been used with two different biodiesels, closer to the transportation sector and whose characteristics of density and viscosity

The second part examines the parametric analysis of the validated numerical model to assess the performance of new test fluids and boundary conditions. In the last part of the result section, three different liquid tests have been performed in the numerical analysis, considering that the model should be able to predict the performance of the metrological meter in the transportation sector. The validation process has been realized using water as a test liquid, because of its availability and

3.3.1 Numerical validation and result

This section presents an extraction of the results of the experimental campaign. The experimental results have been employed in this paper to validate the numerical model described in section 3.2.2. In particular, measurements were taken in a range of temperature between 10 °C and 85 °C, while only the results of the experimental run with water at 20°C are reported in the following Table 3.10.

Table 3.10 Three different scenarios of the test plan were taken by the RISE with water as the test liquid.

	Scenario 1	**Scenario 2**	**Scenario 3**
Temperature (°C)	20	20	20
Kinematic Viscosity ($x10^{-6}$ m^2 s^{-1})	1.0048	1.0048	1.0048
Flow rate (m^3 h^{-1})	14.5	72.6	115.6
Density (kg m^{-3})	998.23	998.27	998.42

Based on the test results, as shown in Figure 3.9 the theoretical discharge coefficient calculated with the RHG equation shows an average error of 0.41% in comparison to the measured discharge coefficient. The measured discharge coefficient exhibited some interesting characteristics. In particular, it was observed that the measured values were consistently higher than the values predicted by theory. This observation is evident when examining Figure 3.9. One possible cause for this discrepancy is that the

edge sharpness of the orifice may have affected the experimental session in some way, or the surface roughness of the pipes may have been higher than expected, leading to higher discharge coefficient values. Measurements were also taken for larger Reynolds numbers (i.e., up to 6 x 10^6), and an extrapolation of the behaviour for undisturbed flow measurement has been evaluated also for very high Reynolds (1 x 10^7).

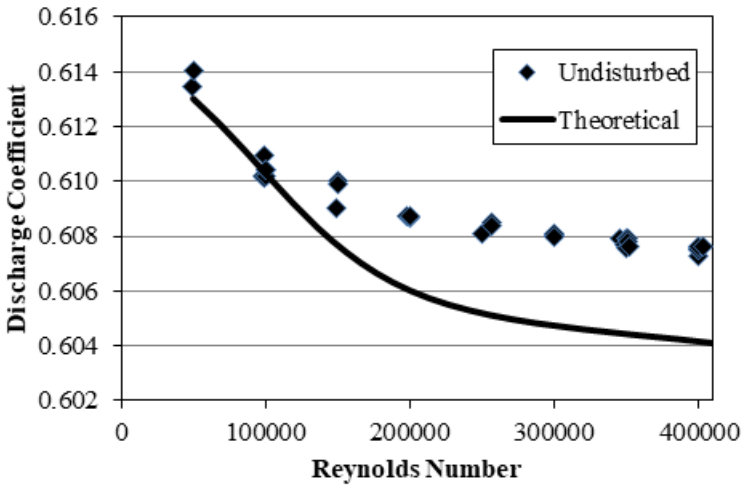

Figure 3.9 Results of the measurements for the undisturbed flow scenario at 20°C.

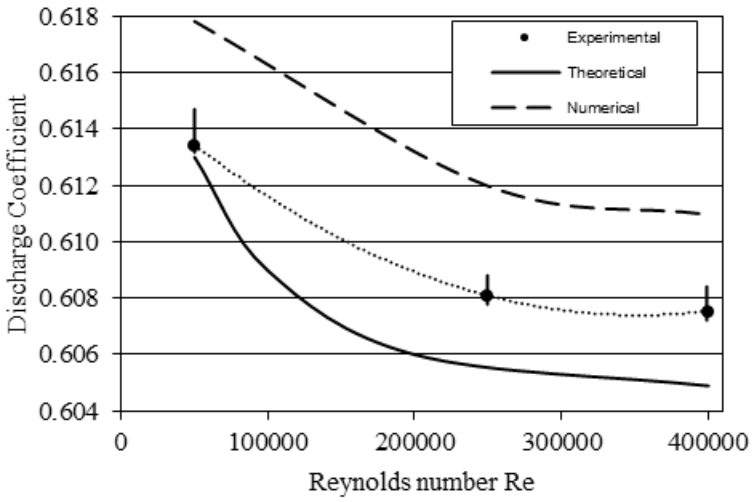

Figure 3.10 Results of the discharge coefficient from the undisturbed measurements at different flow rates and uncertainty are presented in the experimental point

To reproduce the experimental campaign and analyze the effectiveness of the numerical technique, just part of the entire experimental campaign described in Büker et al. [42] has been used for the validation of the numerical model. Three distinct scenarios have been evaluated for the analyzed case, to provide an experimental validation of the numerical results. For all the aforementioned scenarios, water has

been used as a test liquid and its characteristics are presented in Table 3.10. The numerical results were validated on three different Reynolds number values selected from the experimental campaign. The results discharge coefficient was evaluated using the RHG equation (Equation (3.1)) and the numerical differential pressure across the section. The result of the validation is available in Table 3.11. The experimental and numerical comparison highlights the model's capability to predict the discharge coefficient value for all the cases, defining a maximum error of 1.59% for the third scenario.

The results of the validation process demonstrate that the numerical model presented in section 3.2.2 can predict the differential pressure across the section of the orifice plate and consequently evaluate the flow rate in the computational domain.

Table 3.11. Comparison of experimental and numerical results.

	Discharge Coefficient Experimental	**Discharge Coefficient Numerical**	**Error (%)**
Scenario 1	0.6135	0.6178	0.71%
Scenario 2	0.6081	0.6156	1.25%
Scenario 3	0.6076	0.6172	1.59%

3.3.2 Parametric analysis and Variable flowrate

As the initial step, the validated numerical model was utilized for a sensitivity analysis concerning the liquid test. Given that one of the objectives of the SAFEST project is to assess the performance of the flowmeter when innovative fuels are used, two different types of bio-diesel were selected for the analysis. The fluid properties were provided by the National Metrology Institute of the Federal Republic of Germany, known as the Physikalisch-Technische Bundesanstalt (PTB), and they are summarized in Table 3.12, while the characteristics of water were reported in Table 3.10.

Table 3.12. Fluid properties of the two bio-diesel employed in the parametric analysis on the fluid test.

	Biodiesel-1	**Biodiesel-2**
Temperature (°C)	20	20
Kinematic Viscosity ($x10^{-6}$ m^2 s^{-1})	1.733	1.720
Density (kg m^{-3})	761.44	784.81

The same numerical model depicted in section 3.2.2 was used for the parametric analysis. A comparison of the discharge coefficient for the three tested liquid tests is provided in Figure 3.11. The discharge coefficient trends vary significantly between water and biodiesels. The water discharge coefficient shows linear behaviour, ranging from 0.62 to 0.61, while the discharge coefficient for the two biodiesel follows an exponential trend, ranging from 0.64 to 0.60. The numerical analysis consents us to evaluate the performance of untested liquid fuels. Based on the obtained results, it is evident that there exists a correlation between the two biodiesels, as demonstrated in Figure 3.11. This correlation is attributed to the similar thermodynamic characteristics of the two bio-diesels as reported in Table 3.12. Interestingly, the numerical analysis conducted with water showed unrelated results to the fuels test. Furthermore, the curves representing the discharge coefficient demonstrate a flattening trend as the density of the problem decreases, highlighting an important aspect of the behaviour of the numerical analysis that can be useful in the case of experimental tests with an orifice plate in the same β range.

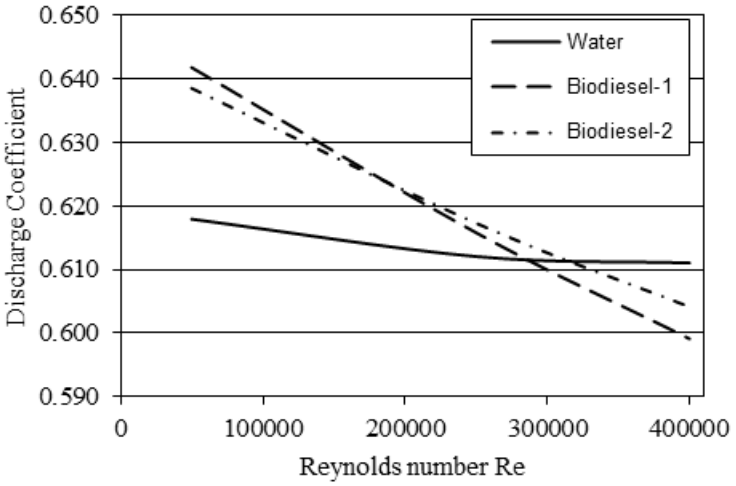

Figure 3.11. Numerical results of the discharge coefficient for three tested fluids and comparison of the trend in the same Reynolds number range.

Upon conducting a parametric analysis, it was observed that the tests performed with biodiesels resulted in notable discrepancies in the discharge coefficient curves compared to the anticipated outcomes specified in ISO Standard 5167. It was found that employing computational fluid dynamics (CFD) models can aid in rectifying the calibration of these measurement systems and consequently diminishing the divergence between the expected flow rate and the measured one. Effective energy accounting and metering are essential components of a sustainable energy strategy.

They provide the necessary data to optimize energy use, reduce costs, minimize environmental impact, and support the global transition to renewable energy sources. Through precise measurement and informed accounting, organizations can make significant progress toward achieving sustainability goals and ensuring long-term environmental and financial benefits. For sustainability purposes, the amount of carbon dioxide emitted by any source is connected to the estimation of the energy required and used during its operation, as summarized in the following equation:

$$\Delta Q_{measured} \propto \Delta C_d \propto \Delta CO_{2_{estimated}} \quad (3.4)$$

It was estimated that for this specific application for low Re and high Re values (respectively $1 \cdot 10^5$ and $4 \cdot 10^5$) the wrong calibration of the flowmeter affects the measurement of the ΔQ_m for 5% and consequently, the CO_2 estimation.

3.4 Conclusion

In this paper, we analyzed the performance of a numerical model for a single-hole orifice plate flow meter under various operating conditions. The 3D Computational Fluid Dynamics (CFD) simulations were validated using experimental data provided by the Research Institutes of Sweden (SP) as part of the European 20IND13 SAFEST project. The institute also supplied the geometry, dimensions, and boundary conditions for the cases studied. Numerical evaluations, conducted within the OpenFOAM environment, focused on assessing the flow meter's discharge coefficient and the differential pressure across the orifice. The CFD results demonstrated the numerical model's reliability and showed good agreement with the experimental data provided by the project partner.

However, further work is needed to accurately determine the dynamic flow rate at the inlet of the computational domain, as the current model has limitations in predicting flow rate with sufficient precision. Future research will aim to improve the model's accuracy, reducing the margin of error. Additionally, the next steps will focus on refining the model for dynamic charging conditions and testing it with novel liquid fuels currently being investigated by the SAFEST project partners.

Accurate flow metering is essential in industries that aim to optimize resource usage, reduce waste, and improve process efficiency. Flow meters are critical in applications such as energy generation, fuel transportation, and chemical processing, where precise measurement of flow rates can minimize energy consumption and material loss. Reliable flow metering systems help optimize operations, thereby reducing the environmental footprint of these processes.

Incorporating CFD tools in the design and analysis of flow meters, such as the orifice plate flow meter evaluated in this study, contributes to the sustainability of industrial systems. By allowing for the simulation of complex fluid behaviors without the need for extensive physical testing, CFD reduces material use and energy costs associated with building and operating experimental setups. Furthermore, the insights gained from CFD models can lead to better-designed systems with higher efficiency and lower emissions.

As the SAFEST project continues to explore novel liquid fuels, the use of CFD for optimizing flow measurement tools becomes even more crucial. These fuels often come with unique properties that necessitate precise measurement and control to ensure sustainable and efficient energy use. Improving the accuracy of CFD models for such applications not only enhances performance but also contributes to the broader goals of sustainability by promoting efficient resource management and reducing environmental impact.

In conclusion, this study highlights the importance of integrating CFD tools into the analysis and optimization of flow metering systems, especially as industries shift towards more sustainable practices. Accurate and efficient metering can play a vital role in reducing waste and emissions, while CFD simulations help streamline design processes, ultimately leading to more sustainable industrial operations.

II

INDOOR AIR QUALITY: MODELLING AND BENCHMARKING

CHAPTER 4. Aerosol dispersion: physics and numerical modeling

4.1 Introduction

Respiratory viruses primarily spread through the transfer of infectious particles among individuals, a process that underscores the importance of understanding both physical and biological mechanisms involved in viral transmission. These pathways illustrate how viruses navigate through their environment and successfully infect new hosts. Gaining a comprehensive understanding of these transmission routes is crucial for the formulation of effective preventive measures and for managing and mitigating the spread of viral infections. The transmission of respiratory viruses may occur through three basic routes [31], [43] that could be summarized as follows:

- **Spray transmission**: This type of transmission occurs when virus-laden droplets, which are particles larger than 100 μm in diameter, are emitted by an infected person. These droplets then land on the mucosal surfaces of a susceptible individual. This mode of transmission is traditionally referred to as large-droplet transmission.
- **Inhalation transmission**: it refers to the small respiratory droplets, also known as aerosol or airborne droplets, that are suspended in the air. These particles are typically below 100 μm in diameter and they are exhaled by an infected person. If inhaled by a susceptible individual, these droplets can potentially transmit infections.
- **Touch transmission:** Refers to both animate and inanimate surfaces that have been contaminated by virus-laden droplets, which are then touched by a person and can transfer the virus to their mucous membranes.

The airborne droplet route has been recognized as the primary pathway of infection transmission in indoor environments [33], [35], [36]. Ballistic drops owe their movement to the momentum gained when they are released [46] and rapidly settle in a range lower than 0.6 m from the source [31], therefore they are a source of contagion only for the subject in close proximity to the source (or by touch transmission in the

long-range). Conversely, particles with a diameter lower than 100 μm can remain suspended in the air for a prolonged time and travel from a long distance in an indoor environment [46], [47], [48], likely infecting multiple individuals sharing the same space of the infected. For these reasons, the commonly recommended safe distance of 1-2 m, widely adopted in most countries to reduce the spread of SARS-CoV-2, can be useful outdoors but is insufficient in indoor environments [46], [49]; rather, it is crucial to study the effects of ventilation and airflow patterns, as they strongly influence particles transport and distribution [50]. Natural ventilation effectively reduces air contaminants and improves indoor air quality [51]. However, it is avoided during the coldest and hottest months of the year due to the disparity between outdoor climatic conditions and the desired thermo-hygrometric comfort [52], [53]. Therefore, it is essential to investigate the effect of Heating, Ventilation, and Air Conditioning systems on indoor air quality and aerosol transport

4.2 Case studies and dissertation goal

The forthcoming sections will delve into the intricate dynamics of aerosol dispersion within indoor settings, shedding light on various case studies that significantly impact our daily experiences. From microscopic to macroscopic environments, we will thoroughly explore how particle behavior can fluctuate, leading to varying levels of exposure and risks for vulnerable individuals.

In Chapter 7, we will examine the dispersion and inhalation of particles by a susceptible individual in close proximity to an infectious speaker, evaluating the risk of SARS-CoV2 infection during a specific exposure period. Utilizing a three-dimensional transient numerical model validated by particle image velocimetry, our study reveals that large droplets pose minimal risk beyond 0.6 meters, while airborne droplets dominate at greater distances. We find that maintaining a distance of 0.75 meters for brief exposures reduces the risk to below 0.1%, but for longer exposures, this safety distance increases significantly.

Moving on to Chapter 8, our focus turns to the analysis of airborne droplet distribution emitted by an infected teacher in a university lecture room over a two-hour speaking session, while varying the air change rate of the HVAC system. This analysis underscores the limitations of increasing the air change rate of the HVAC system in improving indoor air quality and reducing the risk of infections in shared environments, such as lecture rooms. These spaces are particularly vulnerable to

infection transmission due to high occupant concentration, prolonged residence time, and the presence of speaking subjects.

The analysis in Chapter 7 and Chapter 8 will highlight the the limitations of the HVAC system as a means of reducing infection risks in indoor settings. As a potential solution for more targeted control of individual susceptibility, the adoption of personalized ventilation is proposed. This approach would allow for localized regulation of airflow for individuals without significantly impacting the overall airflow in the indoor environment. Chapter 8 delves into the evaluation of a newly designed portable personal air cleaner, assessing its effectiveness in reducing the transmission of respiratory pathogens in both close-proximity scenarios (such as face-to-face conversations) and shared indoor environments (such as the university classrooms discussed in Chapter 7).

4.3 Methodology

4.3.1 Numerical Eulerian/Lagrangian model

The droplet-laden flow evolving in the investigated indoor environments can be regarded as a dispersed dilute two-phase flow since the spacing between droplets is sufficiently large and the particle volume fraction sufficiently low ($<10^{-3}$) [54], [31]. Fluid-particle interaction is here solved by using an Eulerian-Lagrangian approach, modelling the air (i.e., the continuous phase) with an Eulerian approach and tracking the particles (i.e., the discrete phase) individually by solving a force balance equation (Lagrangian Particle Tracking, LPT).

Particles are assumed to be spherical. The trajectory of a single particle in a shear flow can be expressed by the Newton's Second Law [55], [56], [57]:

$$m_d \frac{d\boldsymbol{u}_d}{dt} = \boldsymbol{F}_{body} + \boldsymbol{F}_{surface} + \boldsymbol{F}_{interaction} \tag{4.1}$$

where $\boldsymbol{F}_{body}$ is the body force, $\boldsymbol{F}_{surface}$ is the surface force and $\boldsymbol{F}_{interaction}$ is the interaction force. Body force is given by the sum of gravity and virtual mass forces:

$$\boldsymbol{F}_{body} = \boldsymbol{F}_G + \boldsymbol{F}_{VM} \tag{4.2}$$

The virtual mass force $\boldsymbol{F}_{VM}$ in equation (4.2) arises due to the acceleration of the fluid surrounding the accelerating particle. This force can be neglected when the relative acceleration is small.

Surface force is the sum of drag, pressure, Basset, Saffman and Magnus forces, as described by the following equation:

$$\boldsymbol{F}_{surface} = \boldsymbol{F}_D + \boldsymbol{F}_{pressure} + \boldsymbol{F}_{Basset} + \boldsymbol{F}_{Saffman} + \boldsymbol{F}_{Magnus} \tag{4.3}$$

For particles with a small diameter, pressure, Safmann and Magnus forces can be safely neglected compared to drag forces. In addition, when the fluid density is much smaller than the particle density, the Basset force can also be considered negligible [57].

Finally, interaction force is the sum of Brownian motion force ($\boldsymbol{F}_{BM}$), particle-particle interaction force ($\boldsymbol{F}_{pp}$), and particle-wall interaction force ($\boldsymbol{F}_{pw}$):

$$\boldsymbol{F}_{interaction} = \boldsymbol{F}_{BM} + \boldsymbol{F}_{pp} + \boldsymbol{F}_{pw} \tag{4.4}$$

Brownian motion force can be neglected since the particles considered are of the order of microns in size. Particle-particle interaction forces must be considered for dense particle suspensions [57]; particle-wall interaction forces are important in dense flows, as well as in wall-dominated dilute flows [54]. These forces are assumed to be negligible in the proposed investigations. According to the above discussion, the droplet motion inside the airflow is described by solving the LPT equations below:

$$m_d \frac{d\boldsymbol{u}_d}{dt} = \boldsymbol{F}_D + \boldsymbol{F}_G \tag{4.5}$$

$$\frac{d\boldsymbol{x}_d}{dt} = \boldsymbol{u}_d \tag{4.6}$$

The drag force is given by Crowe et al. [54]:

$$\boldsymbol{F}_D = m_d \frac{18}{\rho_d \cdot d_d^2} C_D \frac{Re_d(\boldsymbol{u} - \boldsymbol{u}_d)}{24} \tag{4.7}$$

The droplet density has been considered constant and equal to 1200 kg m^{-3} as representative of the density of non-volatile components carried by respiratory droplets [58], [59], [60]. The Re_d is calculated as:

$$Re_d = \frac{\rho(|\boldsymbol{u} - \boldsymbol{u}_d|)d_d}{\mu} \tag{4.8}$$

whereas the drag coefficient, C_D, in equation (4.7) is evaluated as a function of the droplet Reynolds number:

$$C_D = \begin{cases} \dfrac{24}{Re_d} & \text{if } Re_d < 1 \\ \dfrac{24}{Re_d}(1 + 0.15 \cdot Re_d^{0.687}) & \text{if } 1 \leq Re_d \leq 1000 \\ 0.44 & \text{if } Re_d > 1000 \end{cases} \tag{4.9}$$

Droplet collisions are generally considered to be elastic, meaning that kinetic energy is conserved during these interactions. When analyzing the dynamics of these droplets, the equations of motion are approached with the assumption of one-way coupling. This suggests that the flow field significantly influences the motion of the droplets, dictating their trajectories and velocities. Conversely, the impact of the droplets on the airflow is considered negligible. Consequently, the complex interactions of droplet motion are primarily modeled with a focus on fluid dynamics, without accounting for significant changes in the flow caused by the droplets. This simplification facilitates clearer predictions of droplet behaviour within the broader context of fluid dynamics.

4.3.2 Droplet emission model

The emission of particles from the infected individual was modeled based on their breathing and speaking activities. Specifically, the rate of particle emission (ERN, particles per second) - which represents the number of particles exhaled by the infected individual per unit time and depends on particle size - was estimated for both speaking and breathing. These estimates were derived from experimental analyses conducted by Johnson et al. [61] and Morawska et al. [62]. A distribution of particles from 0.5 μm to about 1000 μm close to the mouth of an adult person while breathing and speaking, to evaluate the negligibility of the evaporation phenomenon, while the measurement process was notably intricate due to the rapid evaporation characteristic inherent in emitted respiratory particles. The experimental analysis took place within a dedicated wind tunnel, known as the Expired Droplet Investigation System (EDIS), wherein two distinct measurement techniques were employed to encompass the entire size range: an aerodynamic particle sizer (up to 20 μm) and a droplet deposition analysis (μm). For more comprehensive insights into the experimental apparatus and the adopted methodology, interested parties are directed to consult the papers mentioned above [61], [62].

In this section, a simplification of the particle number distribution was considered to make affordable numerical simulations. Thus, the original distribution [61], [62]

was fitted and simplified into five size ranges. The negligible contribution of spray-borne respiratory particles to the risk of infection [31], [63], [64] has led to the limitation of the considered size ranges to airborne respiratory particles (<90 μm). Volume distributions and emission rates (ERV, μl s^{-1}Ap) were computed under the assumption of spherical particle geometry. Considering the quick evaporation phenomenon of the particles after emission [65], [66], in the CFD model the post-evaporation number and volume distributions were considered and the volume particle distribution before evaporation (i.e., as emitted) was reduced to that resulting from the quick evaporation considering a volume fraction of non-volatiles in the initial particle of 1% [65]. This particle evaporation phenomenon reduces the particle diameter to about 20% of the initial emitted size. The particle number and volume distributions pre- and post-evaporation (fitted by five size ranges) adopted in the simulations and the corresponding number and volume emission rates are summarized in Table 4.1 for both the expiratory activities investigated.

As concerns the thermo-fluid dynamics fields in close proximity to the emitter subject, numerical values were validated by Cortellessa et al. [31] against the fields measured with the PIV technique.

Table 4.1 Particle number ($dN/dlog(d_d)$) and volume ($dV/dlog(d_d)$) distributions pre- and post-evaporation fitted by five size ranges as adopted in the simulations for breathing and speaking expiratory activities. Particle number (ER_N) and volume (ER_V) emission rates are also reported.

Expiratory activity	Pre-evaporation					Post-evaporation		
	Particle diameter (size range), d_d (µm)	**$dN/dlog(d_d)$** (part. cm^{-3})	**$dV/dlog(d_d)$** (µl cm^{-3})	**ER_N** (part. s^{-1})	**ER_V** (µl s^{-1})	**Particle diameter (size range), d_d (µm)**	**$dN/dlog(d_d)$** (part. cm^{-3})	**$dV/dlog(d_d)$** (µl cm^{-3})
breathing	2.4 µm (<1.9 to 3.2 µm)	0.312	2.33×10^{-9}	32.6	2.43×10^{-7}	0.5 µm (<0.7 µm)	0.312	2.33×10^{-11}
	4.1 µm (3.2 to 5.4 µm)	0.016	5.80×10^{-10}	1.6	6.11×10^{-8}	0.9 µm (0.7 to 1.2 µm)	0.016	5.80×10^{-12}
	7.1 µm (5.4 to 9.3 µm)	0.005	1.03×10^{-9}	0.6	1.09×10^{-7}	1.5 µm (1.2 to 2.0 µm)	0.005	1.03×10^{-11}
	16.0 µm (9.3 to 27.3 µm)	0.001	2.15×10^{-9}	0.2	4.52×10^{-7}	3.4 µm (2.0 to 5.9 µm)	0.001	2.15×10^{-11}
	35.8 µm (27.3 to 46.9 µm)	<0.001	3.44×10^{-13}	<0.1	3.63×10^{-11}	7.7 µm (5.9 to 10.1 µm)	<0.001	3.44×10^{-15}
	Total	N=0.078	$V=1.92\times10^{-9}$	33.4	8.65×10^{-7}	Total	N=0.078	$V=1.92\times10^{-11}$
speaking	4.6 µm (< 0.5 to 4.6 µm)	0.266	1.39×10^{-8}	217.6	1.14×10^{-5}	1 µm (< 1 µm)	0.266	1.39×10^{-10}
	9.0 µm (4.6 to 17.7 µm)	0.035	1.33×10^{-8}	20.3	7.81×10^{-6}	1.9 µm (1.0 to 3.8 µm)	0.035	1.33×10^{-10}
	23.2 µm (17.7 to 30.4 µm)	0.013	8.75×10^{-8}	3.1	2.05×10^{-5}	5 µm (3.8 to 6.6 µm)	0.013	8.75×10^{-10}
	45.5 µm (30.4 to 68.2 µm)	0.016	8.08×10^{-7}	5.7	2.83×10^{-4}	9.8 µm (6.6 to 14.7 µm)	0.016	8.08×10^{-9}
	78 µm (68 to 90 µm)	0.015	3.83×10^{-6}	1.8	4.48×10^{-4}	16.8 µm (14.7 to 19.2 µm)	0.015	3.83×10^{-8}
	Total	N=0.249	$V=7.71\times10^{-7}$	248.6	7.71×10^{-4}	Total	N=0.249	$V=7.71\times10^{-9}$

CHAPTER 5. Experimental characterisation of a side-mirror model in a wind tunnel

5.1 Introduction

The analysis of particle behaviour in indoor environments has highlighted the necessity for a comprehensive understanding of numerical tools in Lagrangian analysis. Turbulent particle-laden flows are prevalent across various sectors, including engineering, medicine, and environmental applications. Most studies have concentrated on developing empirical correlations among case studies; however, there is a pressing need for a deeper investigation into the local flow characteristics that govern global behaviour. Experimental tools and campaigns have significantly advanced our understanding of the local turbulence behaviour, which can provide valuable insights into the phenomena of single-phase flow [67]. From a research perspective, two key issues arise the modification of turbulence due to the presence of particles and the transport of particles by turbulent flows. These issues are directly linked to the dynamics and characteristics of turbulent particle-laden flows. Existing experiments and numerical simulations have substantially enhanced our understanding of these two aspects. However, since several non-dimensional parameters, such as particle Reynolds number Re_p, particle Stokes number St_p, particle volume fraction Φ_V, particle-to-fluid density ratio ρ_r, particle-to-turbulence length-scale ratio, etc., are involved [68], a full description of the underlying physics and mechanisms of this complicated problem is still lacking.

Computational fluid dynamics (CFD) has proven to be a powerful and reliable tool for predicting local fluid behaviour in turbulent, particle-laden flows. Despite this, there remains a gap in our understanding of how to set up multiphase flow simulations and how to select the most appropriate models to accurately capture the intricate interactions at play. The transport of particles within such environments is a complex phenomenon with significant relevance to various engineering, medical, and environmental applications. Examples include the automotive sector, indoor particle dispersion, and airborne pollutants in shared spaces [69],[70]. Developing a dependable design tool for predicting and understanding these flows is essential, as it

can significantly enhance the accuracy and efficiency of prototype analyses. Numerous studies have explored different strategies for analyzing particle-laden flows. For instance, Kim et al. [71] investigated the fluid dynamics of various side mirror geometries, assessing the impact of three configurations using the Particle Tracking Velocimetry (PTV) technique. Elhimer et al. [72] introduced an innovative technique for the simultaneous measurement of particle velocity in a three-dimensional turbulent flow, comparing the results from Particle Image Velocimetry (PIV) and PTV measurements. Additionally, Chen [73] conducted a numerical investigation to evaluate the performance of ventilation systems in indoor environments, aiming to identify the optimal CFD solution for particle dispersion analysis.

In this chapter, we will delve into an experimental campaign conducted in the TU Delft facilities focusing on the analysis of a simplified side mirror model through Particle Tracking Velocimetry (PTV). The experimental campaign aimed to the definition of a data set useful for the validation of numerical lagrangian models previously employed in Chapter 5 and Chapter 8. During the experimental campaign was possible to change the seeding particles, to perform a comparison between Bubbles and droplets characterized by different Stokes numbers and time response.

This research will be important for the next Chapter, which will focus more on the validation of such Lagrangian models.

5.2 Materials and methods

This section highlights the applied methodology and facilities employed in the experimental campaign in the TU Delft laboratories through Particle Tracking Velocimetry, a specific optic measurement system, which consented us to define the fluid-dynamic of a simplified side mirror model.

5.2.1 Wind tunnel and model

Experiments were conducted in a low-speed open-section wind tunnel (W-Tunnel) of the Aerodynamic Laboratories of the Aerospace Engineering Department of TU Delft. The wind tunnel is characterized by a square contraction ratio of 1:4 and a 0.4 × 0.4 m^2 cross-section and a maximum velocity of 35 m/s. The velocity profile was measured in the freestream region using the three-dimensional Particle Tracking Velocimetry technique (PTV). The side-view mirror model is immersed in the turbulent boundary layer in the freestream region concerning the model height at $\delta/H \approx 0.2$.

A representation of the experimental setup is available in Figure 5.1, in which the side mirror model is located on a black-covered supporting plate of 1m × 0.8 m × 0.01 m dimensions, placed forty centimetres out of the W-Tunnel exit. A 45° edge cut was created on the plate avoiding the separation of the fluid coming from the exit of the wind tunnel. Furthermore, the model has been positioned perfectly in the middle of the W-tunnel exit as clearly visible in Figure 5.1.

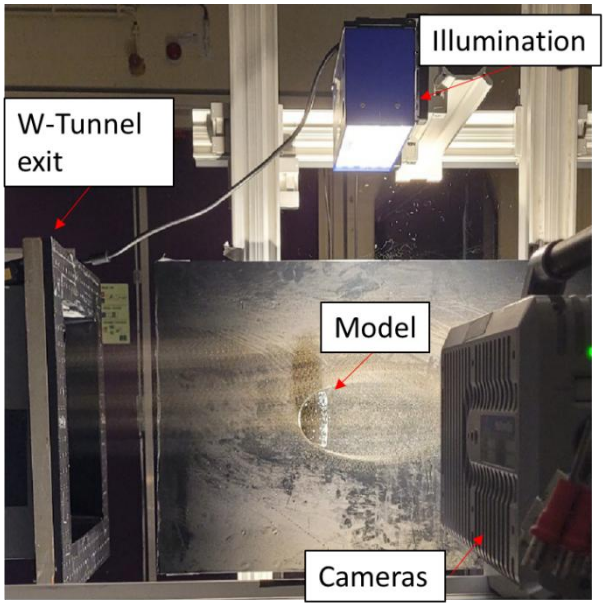

Figure 5.1. Configuration of the setup of the experimental campaign conducted in the W-tunnel.

A 0.3m × 0.3m × 0.3m measurement volume was selected for the experimental campaign to balance the optic characteristics and the measurement quality. The measurements were divided into two sections:

- **Upstream section**: aiming at the evaluation of the potential flow before the simplified model;
- **Downstream section**: aiming at the recirculation zone and wake of the model;

A translation of the whole measurement system has been performed from the upstream to the downstream analysis, aiming at the conservation of the optical and magnification characteristics of the experimental session.

Table 5.1. General characteristics of the case study for the three tracers employed in the experiments

Experimental characteristics	Value
Velocity of freestream	10 m/s

Seeding	Helium Filles Soap Bubbles Air Filles Soap Bubbles Water droplets
Reynolds number	$9 \cdot 10^5$
Height of the model	10 cm
Blockage ratio	1.4%

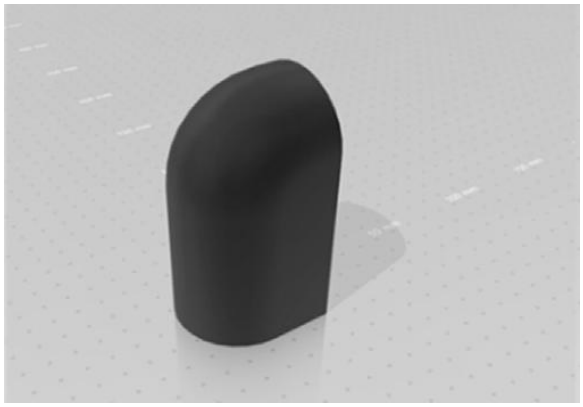

Figure 5.2 Representation of the side mirror model

Figure 5.2 shows the back face of the mirror models tested in the W-tunnel. The side mirror model, represented by a half cylinder with a quarter sphere on top, is the simplest configuration studied for the automotive sector [71]. The choice has been made to create a data set useful for the scientific literature and could be easily replicated considering the boundary conditions above presented.

5.2.2 Measurements system

The Particle Tracking Velocimetry (PTV) system is a complex system composed of various sub-systems working together for the acquisition of the trajectory of particles inside an illuminated volume. In particular, four different high-speed cameras were located at a distance of 0.7 meters from the measurement volume. The placement of the cameras on a beam structure allowed for smooth translation without altering the angle of the imaging systems. This design feature ensures that the quality of the images captured remains consistent, even after the translation of the system from the upstream capture to the downstream acquisition. Two Light Emitting Diodes (LED) illuminations were located on the top and the bottom of the models, to have a measurement volume completely bright and to avoid the possibility of shadowing

during the experimental sessions. The Programmable Time Unit (PTU) was connected to a Personal Computer (PC), the imaging systems and the LED units, aiming at the correct system coordination during the acquisition.

The LaVision fluid supply unit (FSU) controlled the generator, which managed the pressure of air, helium, and soap. The pressure of the three fluids was set at 2.0, 1.5, and 2.0 bar, respectively. The seeding rake was placed inside the wind-tunnel settling chamber. Unfortunately, the turbulence intensity (TI) of the seeding rake in the settling chamber was not explicitly measured, but it was found to be 1.9% two meters downstream of the seeding rake. The nominal diameter of tracer particles was 300 μm, with a maximum expected dispersion of 50 μm based on the work of Faleiros et al. [74]. A summarizing table containing the main characteristics of the imaging system is provided in Table 5.2.

Table 5.2. Optics and imaging characteristics of the four cameras and illumination settings

		Camera (1 – 3)	**Camera 4**
Optics	*Focal length*	60	50
	F#	24	28
Imaging	*Name*	Photron Fastcam SA1.1	Photron Fastcam SA-X2
	Pixel size (μm x μm)	20 x 20	20 x 20
	Acquisition frequency (Hz)	5400	12500
	Magnification factor	0.082	
		LED unit	
Illumination	*Pulse Energy (mJ)*	25	
	Wavelength (nm)	527	
	Spread angle (°)	40	

In a controlled wind tunnel testing environment, researchers utilized Helium-Filled Soap Bubbles (HFSB) and Air-Filled Soap Bubbles (AFSB) as high-intensity tracer particles. The Helium-Filled Soap Bubbles, which are lighter than air, provided valuable insights into airflow patterns and turbulence characteristics, while the Air-Filled Soap Bubbles served to illustrate the dynamics of fluid motion in different aerodynamic conditions. This combination of tracer particles allowed for a

comprehensive analysis of the wind tunnel's performance and enhanced the understanding of the fluid dynamics at play. The HFSB system comprised ten parallel wing rakes, each spanning a length of one meter. The HFSB system consists of 10 parallel wing rakes with 1-m length containing 20 nozzles 5 cm apart from each other. Thus, the seeding rake comprises 200 nozzles with seeding surfaces approximately 0.95 × 0.50m2. The generator is operated by a LaVision fluid supply unit (FSU), which controls the pressure of air, helium, and soap. The pressure of the three fluids is controlled and set at 2.0, 1.5, and 2.0 bar, respectively. The theoretical time response of the seeding particles/Bubbles was calculated considering the equation:

$$\tau_p = d_p^2 \frac{\Delta\rho}{18\,\mu} = d_p^2 \frac{\left(\rho_p - \rho_{fluid}\right)}{18\,\mu} \tag{5.1}$$

A summarizing table containing the time responsiveness of the particles and density is reported in Table 5.3.

Table 5.3. Summarizing table of the seedings characteristics and time response of particles

Particles	Diameter	Density	Theoric time response
HFSB	300-500 μm	$\rho_{HFSB} \approx 1.1\rho_{air}$	$\tau_p \cong 4.87 \cdot 10^{-5} s$
AFSB	300-500 μm	$\rho_{AFSB} = 2.4\frac{kg}{m^3} > \rho_{air}$	$\tau_p \cong 1.16 \cdot 10^{-3} s$
Water droplets	100-200 μm*	$\rho_W = 1000\frac{kg}{m^3}$	$\tau_p \cong 0.06 s$

5.2.3 Experimental procedure

The experimental procedure consists of 3 steps of movement, each consenting to get the fluid-dynamic of particles:

1. **Optical calibration**: is required to triangulate the position of each camera, defining a reference system in the 3D space. A geometrical calibration was performed during each acquisition of the experimental campaign using a calibration plate (Lavision Type 395-54 SSSP) in different positions and orientations of the measurement volume. The resulting disparity was quantified through the root mean square (RMS) of the fit, which was below 0.02 pixels. After the geometrical calibration, volume self-calibration [75] was performed. The initial error in the 1-pixel order was reduced to approximately 0.3 pixels after volume self-calibration was applied. The

optical transfer function is necessary to define and allow a reconstruction of the 3D particle acquisition and follow the movement during the measurement.

2. **Data acquisition**: two main acquisitions were captured during the experimental campaign, one aiming at the upstream section and one aiming at the recirculation zone. The field of view was divided into two distinct sections to avoid shadowing during the measurement and to keep the optic characteristics in a good range for the goal. After a brief check of the position of the side-mirror model and lightning systems, data were acquired through *DaVis 10* software. A set of five-thousands images were acquired at 2 kHz for both upstream and downstream sections, monitoring also the temperature and humidity of the wind tunnel.
3. **Data processing**: The use of high-scattering-efficiency HFSB can reduce the power needed for the light source in CVV systems and thereby minimize background reflection. However, the raw images still contain features due to light reflection from the solid surface. These were removed using a Butterworth high-pass filter applied to the time-history of pixel intensity. The resulting images were analyzed by the Lagrangian particle tracking algorithm STB implemented in LaVision DaVis 10. The triangulation error was chosen within the range of 0.5 to 1.5, as suggested by Schanz et al. [76] . To facilitate the analysis of the results and the calculation of the gradients, the Lagrangian description of the velocity obtained by STB is converted into an Eulerian description through the binning process. The algorithm used is based on the work done by Agüera et al. [77]. The measurement volume is divided into small cubic domains or bins, and in each of them, the velocity is averaged for all the particles that fall in the bin. Similar to the interrogation windows used for analyzing 3D PIV data, a certain amount of overlap between bins is enforced to increase the spatial resolution. The statistical convergence of the information inside each bin is verified by imposing that, for it to be considered valid, each bin has to contain at least 200 particles.

5.3 Results

In this section the results are discussed for the experimental campaign, highlighting the measurements for HFSB and AFSB. As mentioned in previous sections, post-

processing was necessary to obtain a complete measurement volume. The measurements were carried out in two different sections: the upstream section aiming at the side-mirror model potential flow and the downstream section looking at the recirculation zone. The volumes, which measure 0.225 m^3, are merged together obtaining a full measurement volume of 0.412 m^3.

5.3.1 Ensemble-averaged velocity fields

The analysis was conducted by defining the ensemble-averaged velocity field of Helium-Filled Soap Bubbles (HSFB) and Air-Filled Soap Bubbles (AFSB). The analysis is reported as follows:

1. **HFSB fields**: First, the time-averaged velocity field is considered to analyze the effect of the shape of the three considered models, averaging the captured images of five thousand images through a statistic convergence. Figure 5.3 and Figure 5.4 show the time-averaged streamwise velocity along the centerline vertical plane at y/H=0 for the upstream and downstream sections. Figure 5.4 highlights the main recirculation region at the back of the objects. The dimension and the shape of this region are found to be dependent on the shape of the object, as expected. Above the main recirculation region, the flow accelerates due to the finite dimension of the incoming air stream. Given the acquisition frequency f = 2 kHz, a particle moving with free stream velocity U_∞ = 10 m/s moves approximately 2 mm from one frame to another.

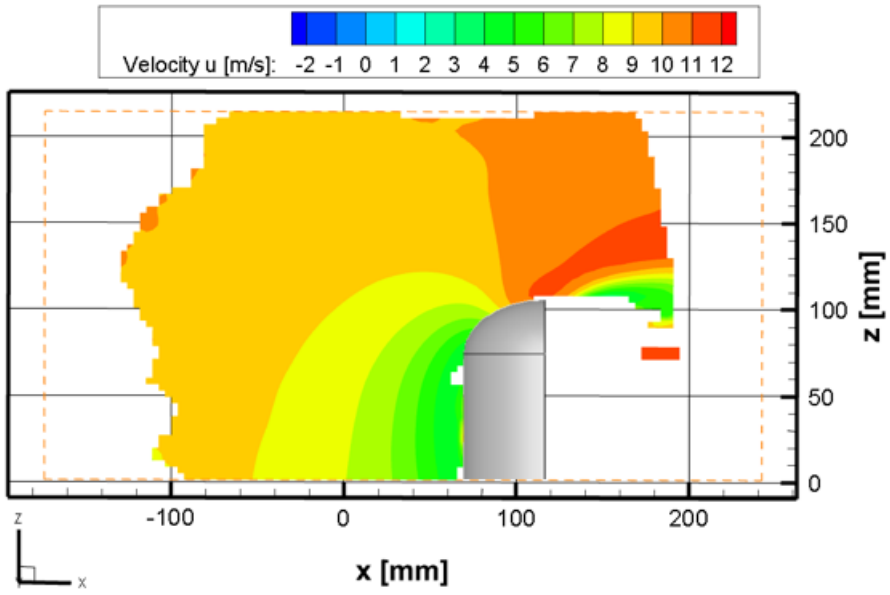

Figure 5.3. Upstream section of the measurement at y=0 mm for HFSB at 10 m/s

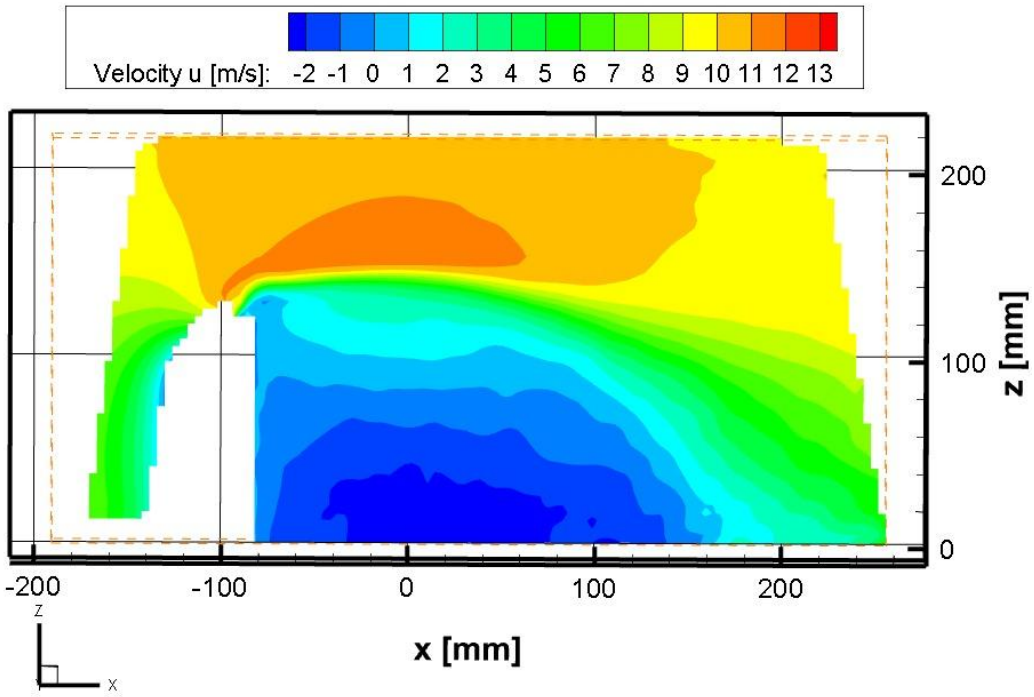

Figure 5.4 Downstream section of the measurement at y=0 mm for HFSB at 10 m/s

The upstream field was translated as 209.87 mm on the x-axis and 23.47mm on the z-axis to match the correct position of the two fields. The upstream section was translated on the z-axis due to the mismatching of the calibration operations. The results are reported in Figure 5.5, Figure 5.6 , Figure 5.7.

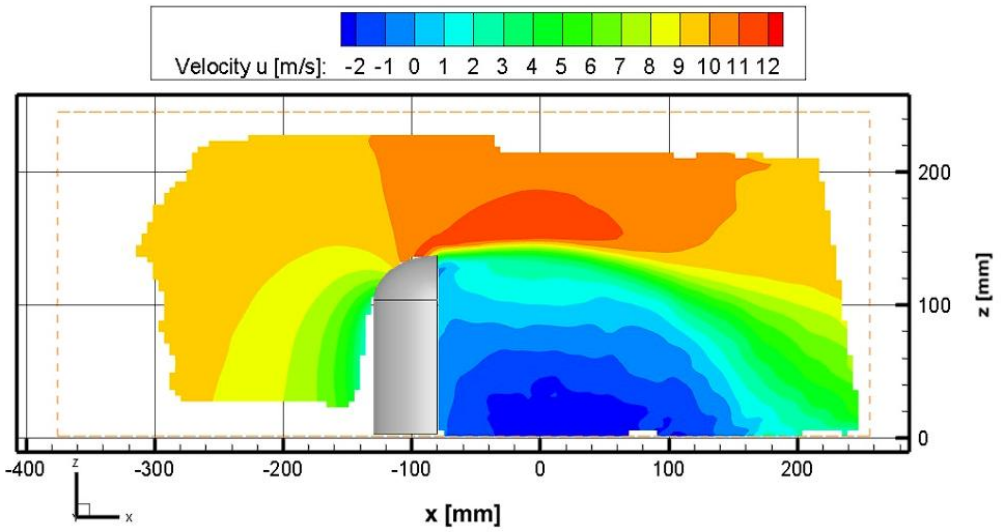

Figure 5.5 Ensemble averaged velocity field at y=0 mm for HFSB at 10 m/s

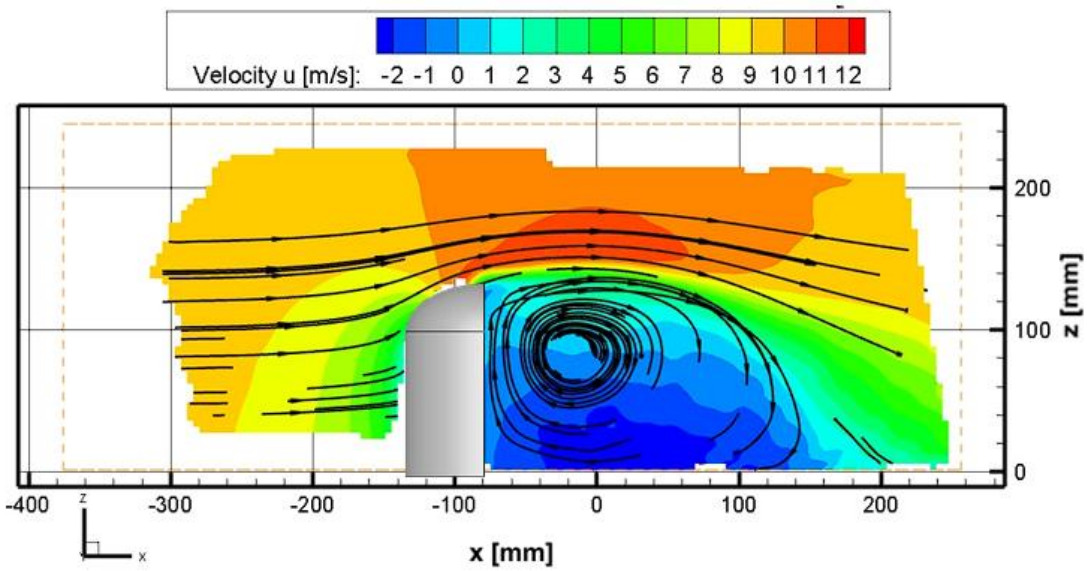

Figure 5.6 Streamlines of the averaged velocity field at y=0 mm for HFSB at 10 m/s

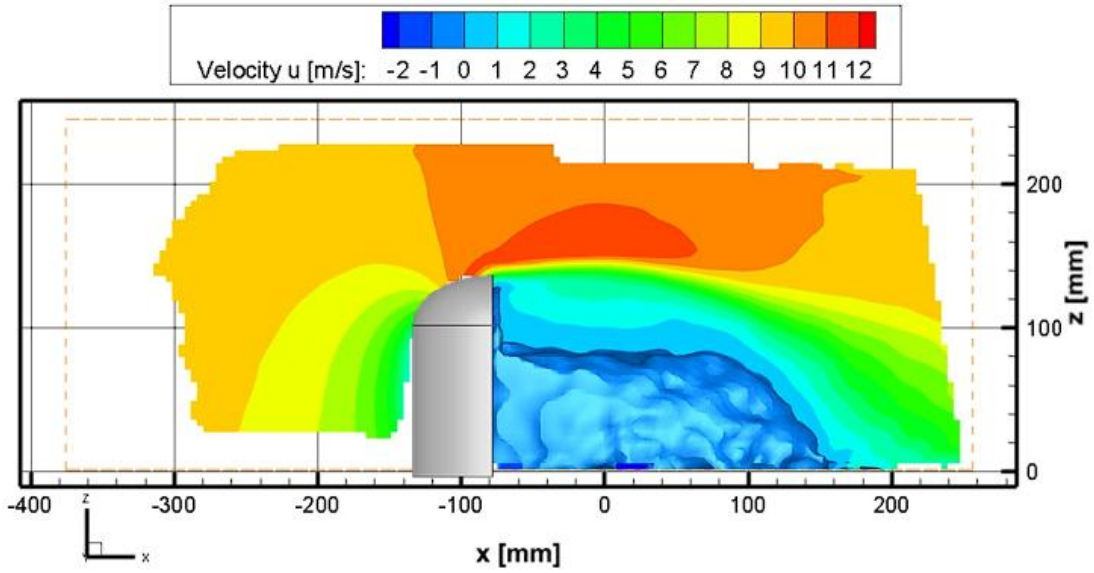

Figure 5.7 Iso-surfaces of V=0 of the averaged velocity field at y=0 mm for HFSB at 10 m/s

2. **AFSB fields:** the same process was provided for the Air Filled Soap Bubbles, which have the same pressure level of soap and fluid, but the bubble content is an air mixture. Twice of the density of the HFSB is registered for the AFSB, which is highlighted in Table 5.3. Summarizing table of the seedings characteristics and time response of particlesTable 5.3. Thus, the time response of the particles is two orders of magnitude different from the HFSB. Furtermore, as mentioned for the previous seeding, the measurement volume was measured in two distinct sections

and a combined volume was obtained through the translation of the upstream section. The same characteristics of the translation were used. Given the acquisition frequency f = 2 kHz, a particle moving with free stream velocity U_∞ = 10 m/s moves approximately 2 mm from one frame to another.

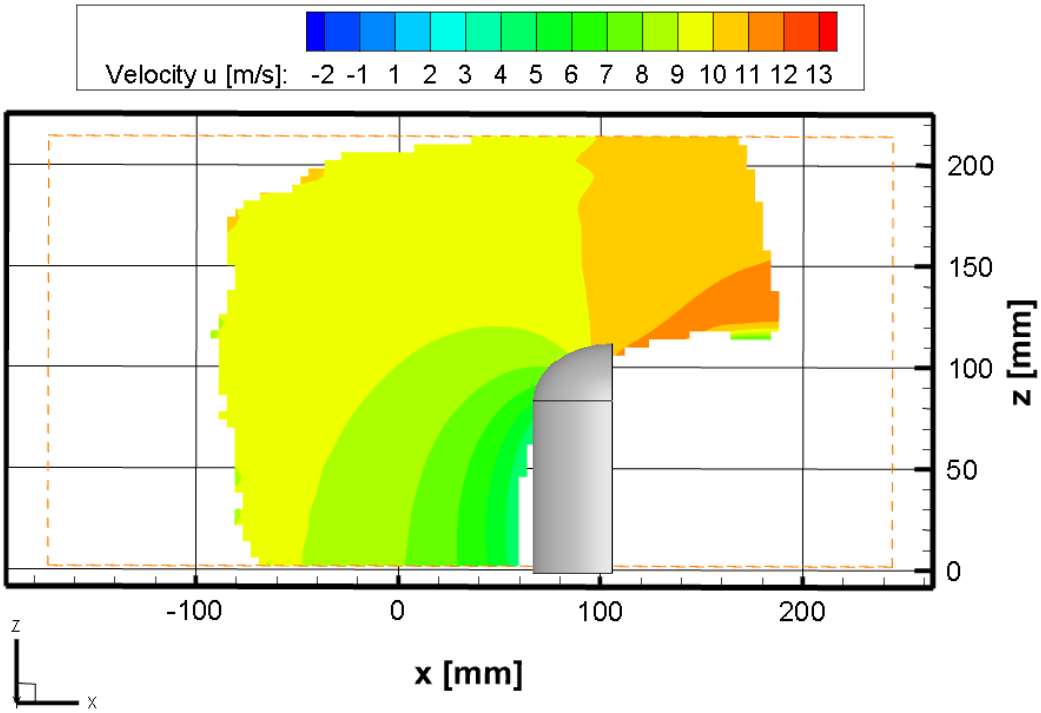

Figure 5.8 Upstream section of the measurement at y=0 mm for AFSB at 10 m/s

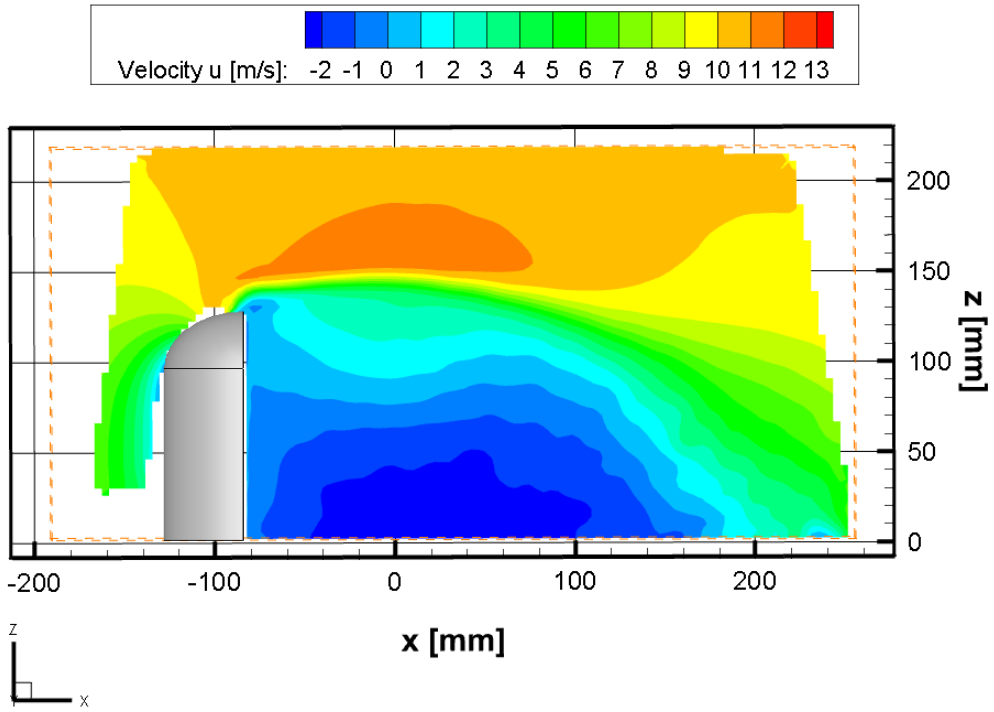

Figure 5.9 Downstream section of the measurement at y=0 mm for AFSB at 10 m/s

Due to a calibration disparity for the upstream and downstream sections, the upstream measurements were translated as 23.47 mm on the z-axis, while to get a correct matching of the two views, it was translated as 209.87 mm on the x-axis.

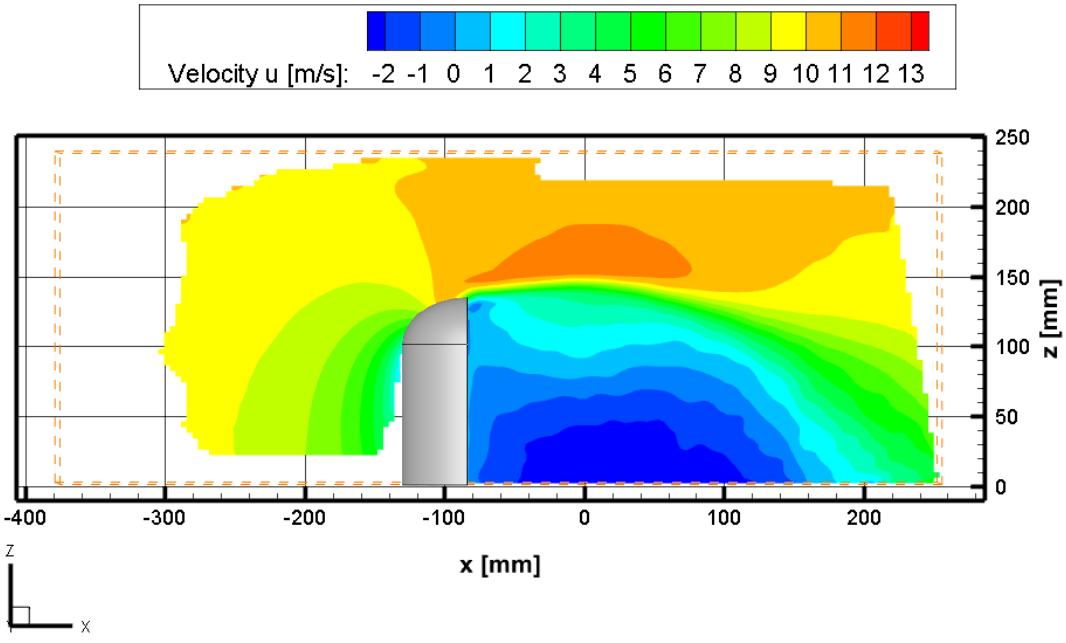

Figure 5.10 Ensemble averaged velocity field at y=0 mm for AFSB at 10 m/s

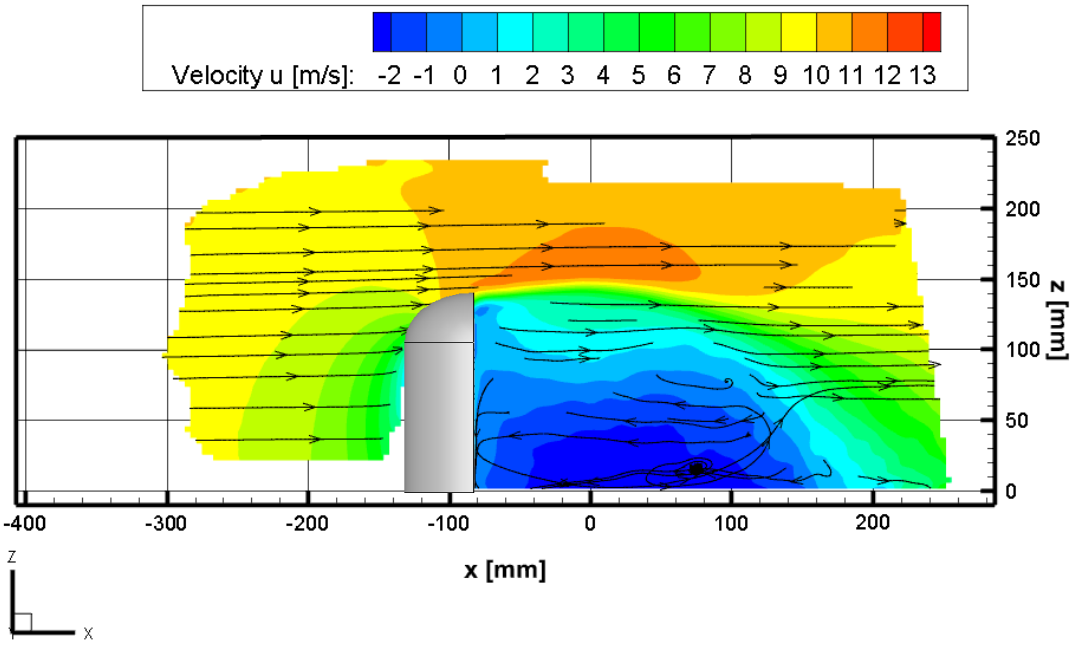

Figure 5.11 Streamlines of the averaged velocity field at y=0 mm for HFSB at 10 m/s

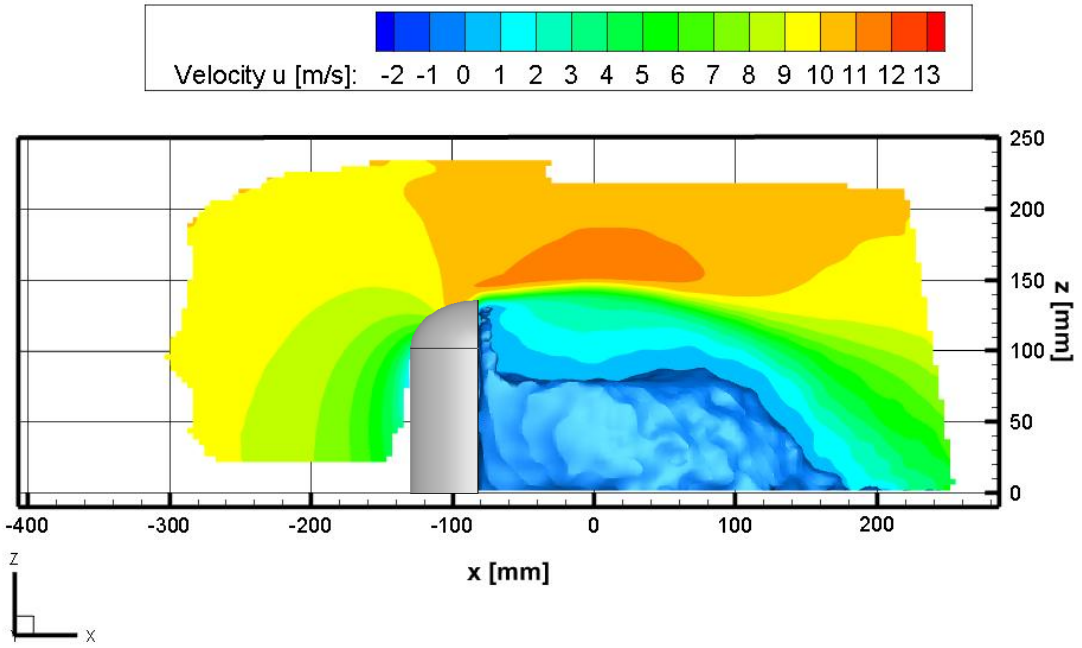

Figure 5.12 Iso-surfaces of V=0 of the averaged velocity field at y=0 mm for HFSB at 10 m/s

The measurements reported for the HFSB and AFSB in the previous figures have shown the capability of the measurement system to fully capture the phenomena, including the recirculation zone and fluid separation in the downstream section. These

measurements, characterized by appreciable uncertainty value, can be used in the validation of lagrangian models in CFD applications.

5.4 Conclusion

This section provides a comprehensive overview of the experimental activities carried out in the laboratories of TU Delft to assess the fluid dynamics associated with a simplified mirror model. The experimental campaign employed the innovative Particle Tracking Velocimetry (PTV) technique, which involved the use of four high-resolution cameras and a specialized seeding prototype developed by the Aerospace Department of TU Delft. The primary focus of the investigation was to analyze the intricate flow structure within a defined measurement volume of 0.3 x 0.3 x 0.3 meters, within which a 10 cm simplification of a mirror model was strategically positioned. To ensure optimal optical performance throughout the measurement campaign, the experiments included a thorough assessment of potential flow characteristics as well as the analysis of the wake produced by the mirror model. This was conducted over two distinct experimental sessions, allowing for comparative analysis and validation of the results. The findings from the PTV measurements were particularly significant, revealing the presence of a large-scale clockwise vortex in the longitudinal plane, which has implications for understanding the complex interactions of fluid around the mirror. Additionally, the experiments indicated a notable flow separation occurring at the upper section of the side mirror model, highlighting areas of potential instability and turbulence. The experimental results presented in this study provide valuable insights that can be utilized as boundary conditions and validation tools for subsequent numerical modelling efforts. In the following chapter, we will integrate the discussed PTV measurements with advanced computational fluid dynamics (CFD) models to facilitate the prediction of the Lagrangian distribution concerning the side mirror model, further enriching our understanding of fluid dynamics in this context.

CHAPTER 6. Analysis of a simplified car side mirror in a wind tunnel using Particle Tracking Velocimetry

6.1 Introduction

In the previous section, we presented the outcomes of an experimental campaign conducted in the laboratories of TU Delft. This investigation focused on a simplified mirror model, which was carried out within an open jet wind tunnel through the Particle Tracking Velocimetry (PTV) technique. The flow of particles in such environments is an intricate and multifaceted phenomenon that spans various fields, including engineering, medicine, and environmental science. Critical applications include assessing particle behaviour in the automotive sector, analyzing indoor particle dispersion, and understanding airborne pollutants in shared spaces. Given the complexity involved, it is paramount to establish a robust design-based tool capable of accurately predicting and comprehending these flow dynamics. Such advancements could significantly improve both the precision and efficiency of prototype-based analyses. Numerous studies have been documented in scientific literature, each exploring different strategies for analyzing particle-laden flows. For instance, Kim et al. [71] delved into the fluid dynamics associated with varying side mirror geometries. Their research meticulously evaluated the impact of three distinct configurations on fluid dynamics, employing the Particle Tracking Velocimetry (PTV) technique to obtain detailed insights. In another significant study, Elhimer et al. [72] pioneered an innovative method to measure particle velocities within a three-dimensional turbulent flow simultaneously. This work provided a comparative analysis of Particle Image Velocimetry (PIV) and PTV measurements, enhancing the understanding of their respective capabilities and limitations. Furthermore, Chen [73] conducted a comprehensive numerical investigation aimed at evaluating the effectiveness of ventilation systems in indoor environments. The primary goal of this research was to identify the most suitable computational fluid dynamics (CFD) solution for particle dispersion analysis, an endeavour that is crucial for ensuring optimal indoor air quality.

Indoor air quality studies and the dynamics of particle convection in enclosed environments present unique challenges due to their inherent complexity. Addressing these challenges requires applying diverse analytical tools to ensure accurate predictions and analyses. In light of this, integrating innovative concepts and analytical methodologies is essential for setting new standards and driving advancements across various sectors. Notably, a gap exists in the scientific literature regarding the Lagrangian benchmarking of CFD models validated through specific experimental campaigns. To address this shortcoming, a CFD Lagrangian numerical model will be systematically compared against the experimental data derived from this study. This process aims to validate the results and contribute to the broader understanding of particle dynamics in fluid environments.

6.2 Materials and methods

In this paragraph, the CFD methodology for the numerical analysis of the card side mirror model in a transient condition. The boundary conditions were determined through the experimental campaign presented in Chapter 5 In the open jet wind tunnel of the TU Delft. The idea behind the developed numerical model is to divide the analysis into two distinct sections, one aiming at the validation of the Eulerian fields, defining the correct fluid dynamic, and the validation of the Lagrangian field. The CFD Eulerian-Lagrangian model is presented in the following sub-section: the first section highlights the Eulerian model and the validation of the fluid dynamics by employing different CFD approaches. The

6.2.1 Eulerian model

The particle-laden flow evolving in the proposed scenario is solved with an Eulerian approach, modelling the air (i.e. the continuous phase) in an Eulerian framework by solving the well-known mass and momentum equations. [16] In this preliminary study, the characteristics of the Eulerian model are provided. The study utilized the open-source OpenFOAM code, based on the finite volume formulation, allowing us to modify the thermophysical and mathematical models to suit the investigated problem. For the fluid-dynamic evaluation of the side mirror case, three different approaches were tested:

- The Unsteady Reynolds-averaged Navier-Stokes (URANS) approach was employed to resolve the mass and momentum equations. The Shear Stress Transport (SST) k–ω turbulence model, as documented in [6], proved to be the

most appropriate model for accurately predicting the velocity and pressure within the computational domain. For brevity, this section does not document the specifics of the URANS turbulence model utilized, but such information can be found in [79].

- The **Detached Eddy Simulation (DES)** approach, which consents to reaching the results achievement by employing a URANS combined with the LES model [80]. Regions near solid boundaries and where the turbulent length scale is less than the maximum grid dimension are assigned the RANS mode of solution. As the turbulent length scale exceeds the grid dimension, the regions are solved using the LES mode. Therefore, the grid resolution is not as demanding as pure LES, thereby considerably cutting down the cost of the computation. The methodology is a numerically feasible and plausibly accurate approach for predicting massively separated flow at high Reynolds numbers. [81]
- The **Large Eddy Simulations (LES)** approach is often employed to capture the turbulent flow features more efficiently by resolving large-scale eddies directly while modelling the effects of smaller scales using subgrid-scale (SGS) models, which are the most computationally expensive to resolve, via low-pass filtering of the Navier–Stokes equations [82]. The Smagorinsky filter was chosen to analyze the side mirror model in the computational domain, assuming that the small scales' energy production and dissipation are in equilibrium. [82]. LES complements the Lagrangian framework by providing a detailed representation of the flow field that can be coupled with particle tracking or droplet dynamics, which are key aspects of Lagrangian studies. The interaction between particles and the resolved turbulence structures enhances the accuracy of simulations in applications like spray modeling, pollutant dispersion, and multiphase flows. By focusing on large-scale eddies and using appropriate SGS models, LES allows for a more computationally feasible simulation of complex turbulent flows in Lagrangian contexts.

The pressure-velocity coupling was solved with the Pressure Implicit with Splitting of Operators (PISO) algorithm, enabling the processing of fully transient phenomena with a real-time step. The control of the time step is provided by defining the Courant number following the numerical approach described by Arpino et al. [30]. An averaged field approach has been considered to perform the numerical analysis, while the numerical model is fully transient. Six probes have been placed in the upstream and downstream sections of the model to understand

the averaging field's starting time. Thus, after four seconds of simulation, the velocity deviation in the considered probes was under 1.5% and the average velocity field was calculated for ten seconds.

The boundary conditions of the numerical simulations are presented in Figure 6.1, considering that a symmetry boundary condition was set to replicate the exact conditions of the numerical campaign:

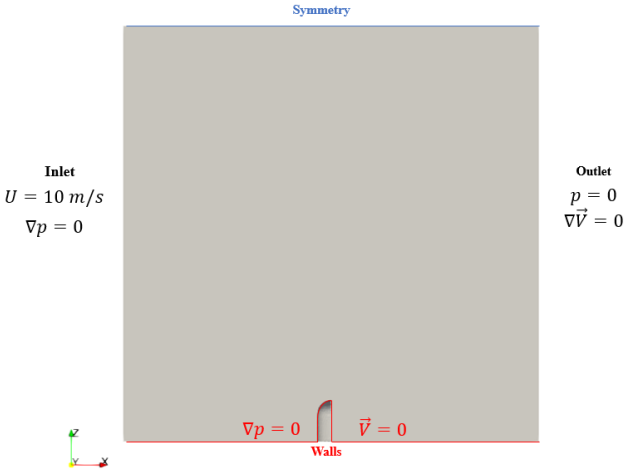

Figure 6.1. Boundary conditions of the three-dimensional numerical simulation.

The hexahedral-based structured grid was defined and used to simulate the side mirror model case, whose clipping is shown in Figure 6.3**Error! Reference source not found.**. The computational domain was generated by employing the OpenFOAM tool "snappyHexMesh". The mesh was selected based on a comprehensive sensitivity analysis, to get a proper evaluation of the grid size and grid characteristics. The sensitivity analysis was conducted by doubling the number of elements in each step, as presented in Table 6.1

Table 6.1. Characteristics of the three meshes used for the sensitivity analysis

	Mesh 1	**Mesh 2**	**Mesh 3**
Number of elements	$1.21 \cdot 10^6$	$2.08 \cdot 10^6$	$4.46 \cdot 10^6$
Maximum Skewness	0.96	0.96	0.97
Average non-orthogonality	37.24	36.92	36.66

A refinement box in the side mirror model zone was generated, locally generating a doubling mesh size to better describe the phenomena. The mesh was selected by comparing the three aforementioned meshes, on the stagnation streamline and on the

top of the side mirror. The extraction lines are highlighted in Figure 6.2 and the results of the sensitivity analysis are reported in Table 6.2:

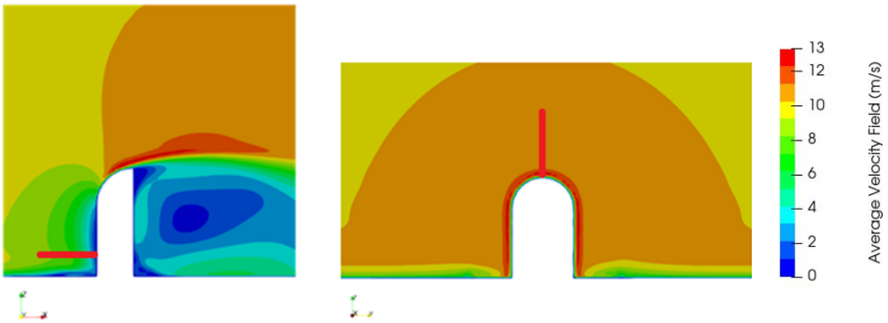

Scenario 1 Scenario 2

Figure 6.2. Average velocity field for the numerical simulations and line of extraction

The sensitivity analysis was performed by evaluating the average error from mesh 3, which was considered the reference for the sensitivity analysis. The average error was calculated as reported in Equation (6.1):

$$Error = \sum \frac{\left|u_{mesh\ x,i} - u_{mesh\ 3,i}\right|}{u_{mesh\ 3,i}} \tag{6.1}$$

Table 6.2. Sensitivity analysis conducted on the three tested computational domain

	Comparison 3-1	**Comparison 3-2**
Scenario 1	8.2%	3.5%
Scenario 2	3.4%	0.9%

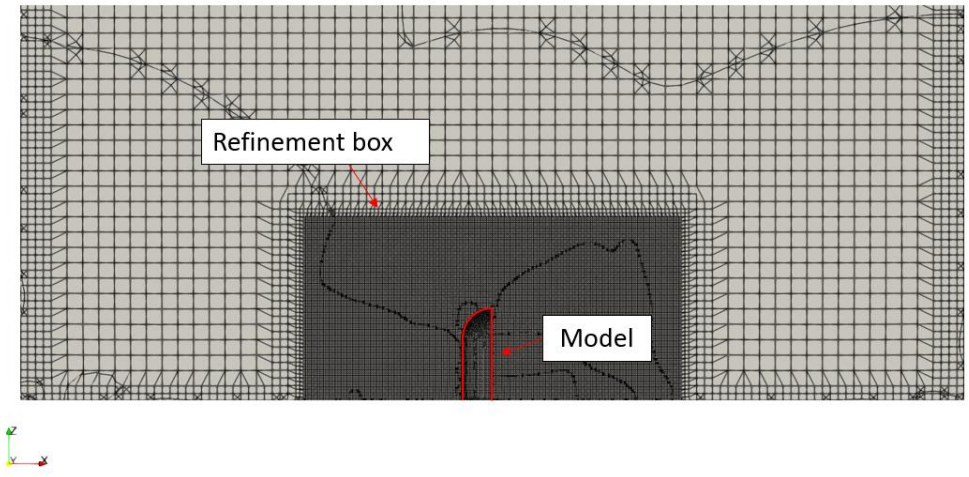

Figure 6.3 A clipping of the chosen mesh for the numerical analysis

The velocity field is averaged after four seconds of simulation, generating a static velocity field on which the particle-laden is mounted.

6.2.2 Lagrangian model

The proposed Lagrangian model is based on the findings highlighted in Chapter 4 and especially in the applied methodology reported in the sub-section 4.3. The particles are injected in a semi-steady-state velocity field, which is obtained by simulating the Eulerian model and achieving an average field in which the particles would evolve. The Lagrangian model is developed based on the characteristics of the Helium-Filled Soap Bubbles and Air-Filled Soap Bubbles reported in Chapter 5, while the injector's characteristics were taken considering the prototype rake used within the experimental campaign. In Table 6.3 the characteristics of the real injectors are reported:

Table 6.3 Characteristics s of the seeding rake in terms of production of bubbles, number of rake and injectors.

Characteristics	Value
Bubbles production rate (Bubbles/sec)	30.000
Number of injectors	72
Number of injectors line	7
Height of the wings (m)	0.8

The numerical reproduction of the seeding rake is obtained considering the scale factor from the settling chamber and the wind tunnel exit, which was 0.4×0.4 m^2. A representation of the numerical seeding rake is provided in Figure 6.5 in the red dots, considering that the dimension of the injector is exaggerated for visual consideration. The position of the injectors is near the entrance of the computational domain, at 0.7m from the side mirror model (located in the origin of the domain), thus consenting the bubble to develop and follow the validated fluid-dynamic. The characteristics of the HFSB and AFSB in terms of time response, production and dynamic evolution in the flow can be found in [83] by Faleiros.

A representation of the real production of the HFSB and AFSB can be evaluated in Figure 6.4.

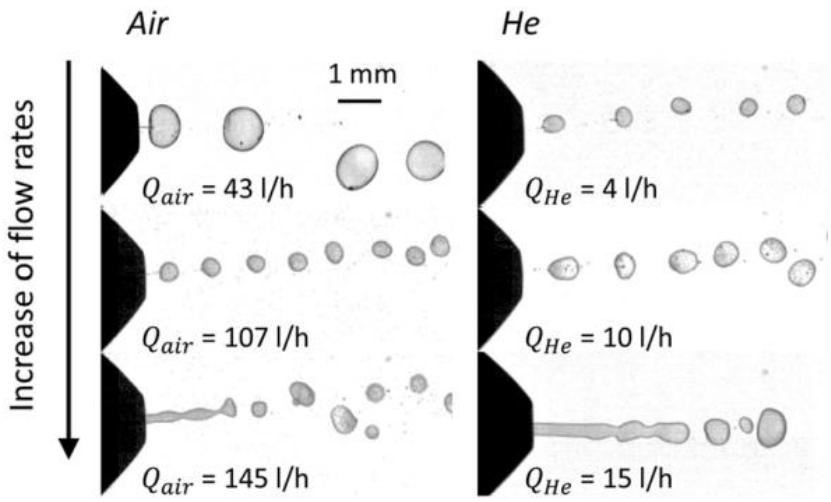

Figure 6.4 HFSB and AFSB production varying the flow rate of Helium and Air inside the bubble.

In this context some simplifications were needed to correctly evaluate the performance of the Lagrangian model:

- HFSB and AFSB were considered as solid particles of a defined diameter, with constant characteristics (defined in the sprayCloudProperites of the OpenFOAM file).
- The evaporation effect was neglected in the study;
- An elastic collision model was considered with a unitary elastic module (the collision between particles determines the full exchange of energy between the subjects)
- Gravity effects were considered in the model.

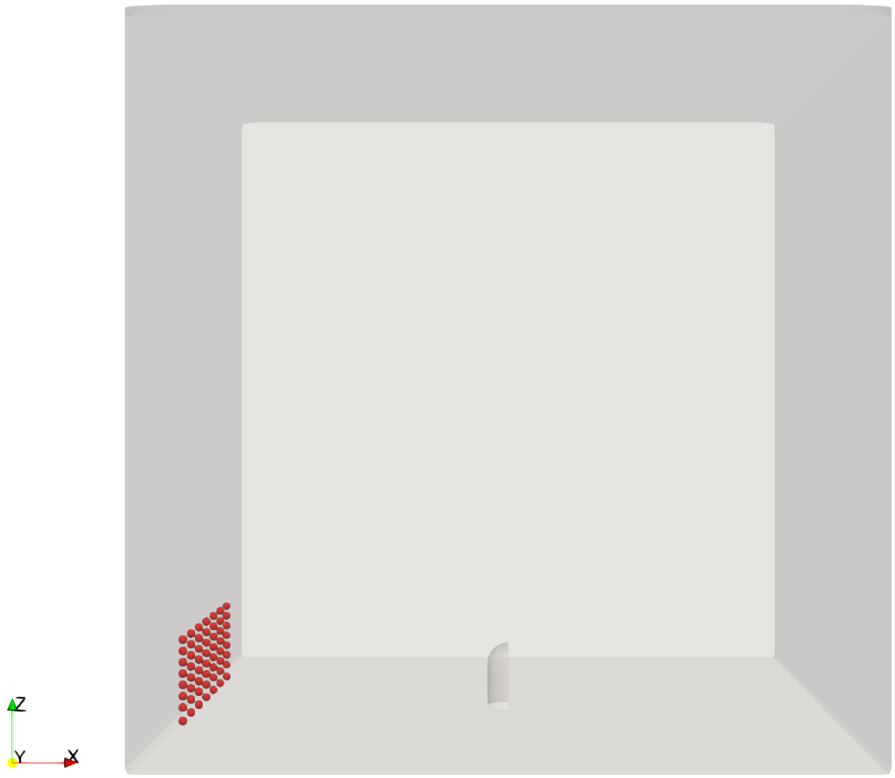

Figure 6.5 Numerical reproduction of the seeding rake in the computational domain, located at x=-0.72m

6.3 Results

In this results section, the Eulerian and Lagrangian results are reported in two distinct phases. The same structure of sub-section 6.2 is provided, dividing the fluid-dynamic validation from the particle behaviour. In the first step, the validation of the Eulerian field is provided through the averaged velocity profiles in the zone of interest, while the Lagrangian field is evaluated through statistic comparison in slices.

6.3.1 Eulerian results

The fluid-dynamic validation was carried out considering two velocity profiles in the middle and three-quarters of the height at y=0. In Figure 6.6 and Figure 6.7 A comparison of the three developed numerical models and the experimental data is provided. These two sections were selected based on the data available and for the importance of the data on the stagnation streamline, which is located at y=0. This

extraction plane is extremely important in a potential flow scenario and it was tested at two different heights of the z-axis, respectively at 0.075 m and 0.1 m.

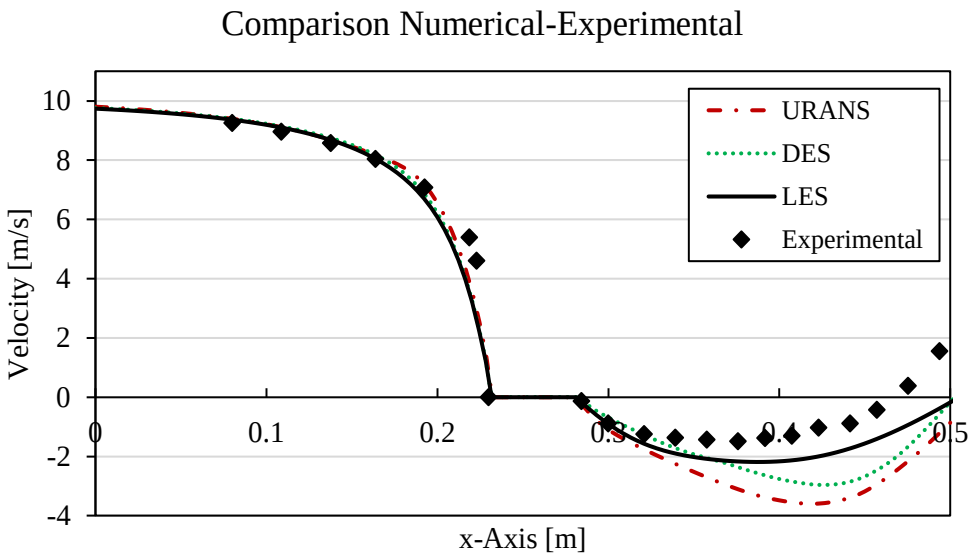

Figure 6.6 Comparison of the numerical CFD models and the experimental data at y=0 and z=0.075m

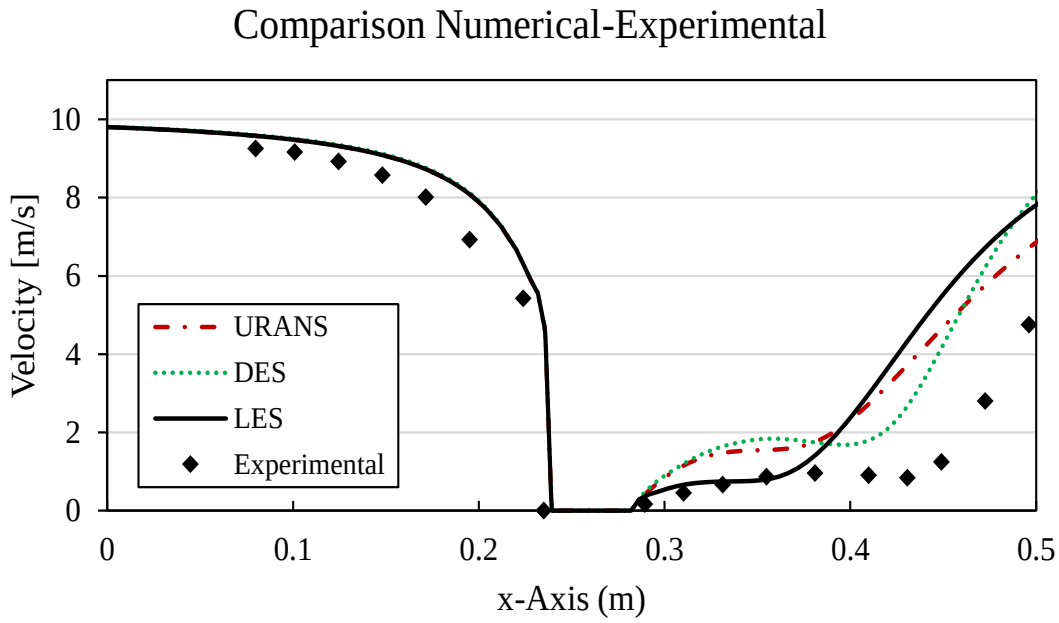

Figure 6.7 Comparison of the numerical CFD models and the experimental data at y=0 and z=0.1m

The data presented in the previously mentioned figures indicate that the Large Eddy Simulation (LES) model stands out as the most profitable numerical simulation for this study, particularly when compared to experimental measurements. While several models demonstrate a reasonable ability to predict the velocity field in the upstream

section—characterised as a potential flow—the most challenging aspect occurs within the recirculation zone. Specifically, it performs exceptionally well at the middle-height extraction point, although it encounters some difficulties at the three-quarter height extraction point. This challenge is attributed to the model's proximity to the separation zone of the side mirror configuration, where turbulent effects are more pronounced and harder to accurately simulate.

In terms of performance metrics, the LES model displays an average error of only 3.2% across both extraction planes. This level of accuracy allows us to confidently validate the LES model's efficacy in mimicking the fluid dynamics of the system being studied. In comparison, the Unsteady Reynolds-Averaged Navier-Stokes (URANS) and Detached Eddy Simulation (DES) models also make efforts to capture the fluid dynamics, but they do so with significantly larger error margins, indicating their limitations in this specific context.

6.3.2 Lagrangian results

The performance of the Lagrangian model was evaluated in two different aspects: the capability of the numerical simulations of replicating the experimental conditions of the presented experimental campaign and the statistic comparison of the Bubbles to occupy the same zone in a comparable time evolution. To perform the comparison two seconds of the acquisition phase and of the numerical simulations were considered. In the first phase, the qualitative results of the numerical simulations is reported, thus giving the idea of the particles evolving in the computational domain and the age of the particles after two seconds of simulations. The results of the CFD lagrangian model are highlighted in Figure 6.8 and Figure 6.9.

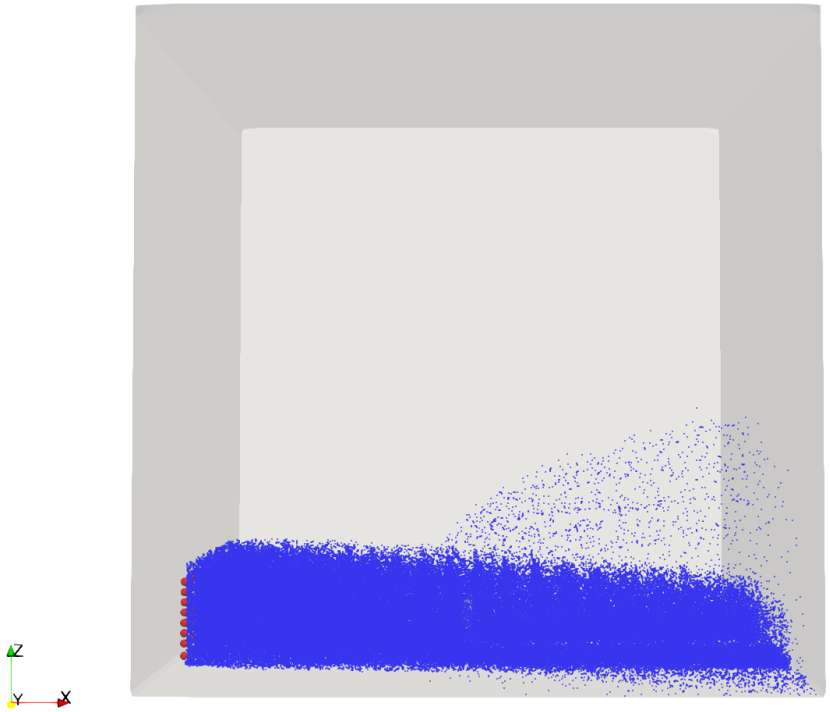

Figure 6.8 Position of the particles after two seconds of evolution in the computational domain

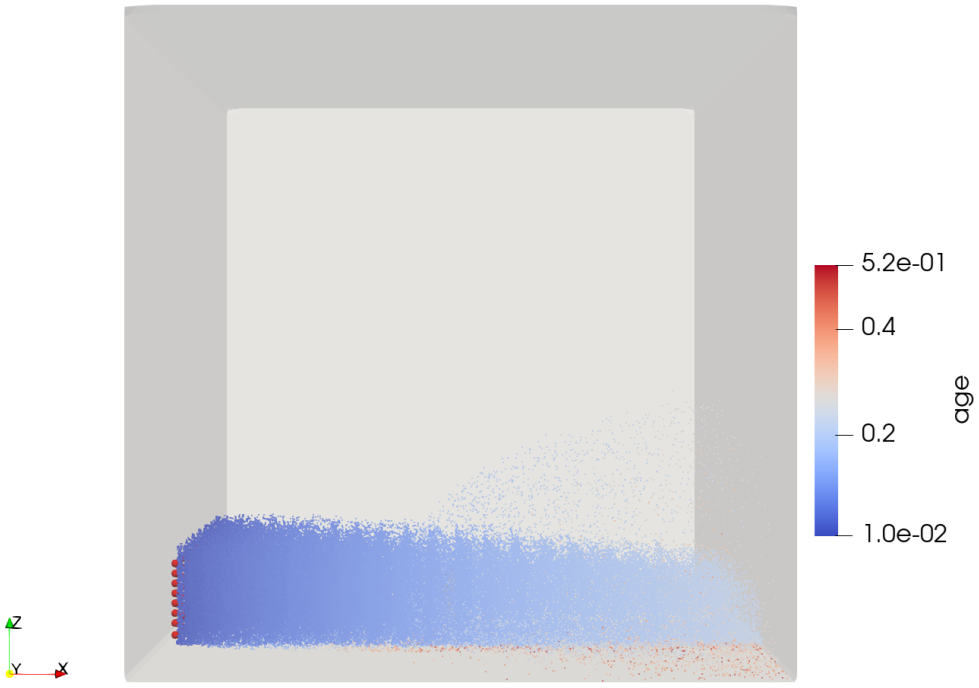

Figure 6.9 Age of the particles after two seconds of evolution in the computational domain.

A first statistic comparison is available in Figure 6.10, which provides the same measurement volume extracted with the PTV technique in the experimental campaign. The box dimensions are 0.5 × 0.3 × 0.25 m^3 to match the experimental measurement volume in the numerical result. The idea is to compare the number of particles statistically registered in the numerical simulation against the number of particles experimentally measured. This is an attempt to evaluate the performance of the numerical model, while it is not possible to follow each particle in the computational domain on each time step.

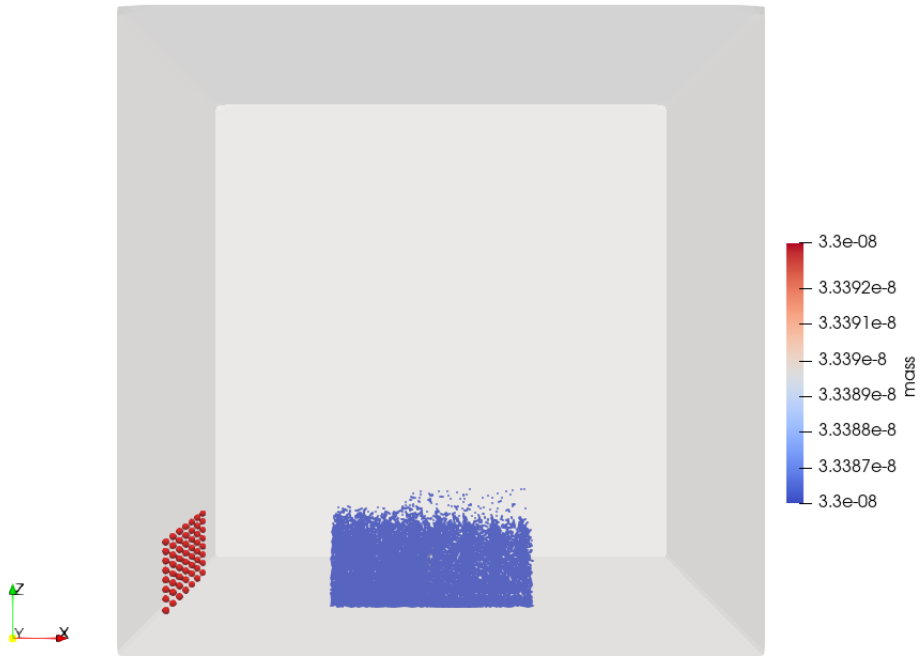

Figure 6.10 Evaluation of the measurement box surrounding the side mirror model, mirroring the experimental conditions of the wind tunnel

To fully understand the numerical model's performance, the mass and number of particles for both HFSB and AFSB for numerical and experimental measurements are compared. Table 6.4 highlights the comparison between the mass per unit volume and the number of particles in the considered measurement box, considering the average error registered validating the numerical results against the experimental data.

Table 6.4 Comparison of the numerical and experimental mass per unit volume and number of particles in the measurement volume.

	Experimental		**Numerical**		**Error**
	HFSB	**AFSB**	**HSFB**	**AFSB**	

Mass per unit volume (kg/m^3)	2.42E-06	4.84E-06	2.33E-06	4.66E-06	3.46%
Number of particles	5.21E+06	5.01E+06	4.96E+06	4.76E+06	4.8%

The data presented demonstrates the developed numerical Lagrangian model's effectiveness in accurately predicting the mass and number of particles within the validated fluid dynamics framework. The model achieves an average error of 4.1%, reflecting its strong performance across various conditions within the computational domain. This flexibility allows for extensive testing with different liquids and particles under various scenarios, facilitating a deeper understanding of the behaviour and movement of droplets and particles. These simulations give us valuable insights into how these elements interact within fluid environments.

6.4 Conclusion

In conclusion, this chapter has conducted a numerical investigation into the dynamics of particle-laden flow using a simplified mirror model within an open jet wind tunnel, utilizing the Particle Tracking Velocimetry (PTV) technique. Particle-laden issues are prevalent in various applications, including automotive design, indoor air quality assessment, and environmental monitoring. This study offers valuable insights into a complex, multidimensional phenomenon. The experimental findings align with previous literature, enhancing our understanding of PTV's capabilities in capturing detailed particle movement across diverse flow conditions. Additionally, this chapter has identified a gap in existing research concerning the Lagrangian benchmarking of Computational Fluid Dynamics (CFD) models validated through targeted experimental data. Addressing this gap in subsequent chapters will enable a systematic comparison between the CFD Lagrangian model and experimental data, ultimately aiding in the development of a robust design tool for precise particle flow analysis.

By focusing on particle flow behaviour, the Lagrangian model developed in this research aims to benchmark its performance by comparing Lagrangian results against the experimental findings from Chapter 6. The first section validates the fluid

dynamics by comparing velocity fields in the area of interest with various Eulerian models (URANS, DES, and LES). The second section presents a statistical comparison of particle distribution, considering the full view of the measurement volume obtained during the experimental campaign.

III

INDOOR AIR QUALITY: APPLICATIONS

CHAPTER 7. Aerosol dispersion in close proximity: a case study of two facing person

7.1 Introduction

The COVID-19 pandemic has drawn significant attention to the role of respiratory droplets in transmitting airborne diseases, underscoring their critical importance in public health. Respiratory activities such as breathing, speaking, coughing, and sneezing release droplets that can carry viral particles, making them potential vectors for disease transmission [84]. Traditionally, transmission pathways have been categorized into three primary routes: fomite, large droplet, and airborne droplet [85] [43]. Historically, the large droplet route has been mistakenly emphasized as the dominant transmission mode for respiratory infections.

Consequently, social distancing guidelines of 1–2 meters were introduced as preventive measures, to minimize exposure to large droplets. However, growing evidence suggests that these measures may overlook the importance of smaller airborne droplets, especially in indoor environments [86].

The distinction between large droplet and airborne transmission routes is crucial, particularly given that large droplets (>100 μm) tend to settle quickly due to gravity, limiting their infective range to close proximity [87].

In contrast, smaller droplets (<100 μm) can evaporate and shrink into droplet nuclei, allowing them to remain airborne and travel greater distances, potentially increasing the risk of transmission [85]. Recent studies, such as those by [86], have shown that airborne transmission dominates within the common social distancing range of 1–2 meters, particularly during respiratory activities like speaking and coughing. However, the simple analytical models used to evaluate these dynamics often do not account for the complex fluid mechanics involved in exhaled airflows, inhalation processes, and environmental factors that influence viral transmission.

The increasing recognition of airborne transmission challenges our current understanding of infection control and emphasizes the need for more advanced methodologies to evaluate and mitigate risks. Computational Fluid Dynamics (CFD) offers a promising approach in this regard. Numerical simulations enable detailed

modelling of the intricate fluid behaviours associated with respiratory droplets, encompassing their generation, movement, and evaporation under varying environmental conditions. This technology can play a crucial role in overcoming the limitations of traditional models, which often assume steady-state conditions and overlook the complexities of human breathing and airflow patterns [88] [89]. Beyond its immediate relevance to public health, the integration of CFD into the study of droplet transmission is aligned with broader sustainability objectives. As the world endeavours to create healthier indoor environments that minimize disease transmission, optimizing ventilation systems and building designs using CFD can improve air quality and energy efficiency. Furthermore, CFD models can aid in the design of sustainable, pathogen-resistant buildings by predicting airflow patterns, thereby reducing the dependence on energy-intensive ventilation systems. Additionally, these models enable real-time assessments of indoor air conditions, which can inform strategies to reduce the risk of airborne transmission without compromising environmental sustainability. Considering these factors, a more comprehensive approach to disease prevention and sustainability is imperative. This section provides a CFD-based analysis aimed at evaluating the infection risk associated with the respiratory activity of two facing subjects. The CFD models are based on the mathematical models outlined in Chapter 4, offering a deeper understanding of droplet dynamics and airborne transmission.

7.2 Materials and models

The proposed SARS-CoV-2 infectious risk assessment is characterized by an integrated approach, based on the following main steps:

- development of a three-dimensional Eulerian-Lagrangian numerical model to describe droplet spread once emitted by a speaking person in transient conditions; this is based on an Eulerian-Lagrangian approach, in which the continuum equations are solved for the airflow and Newton's equation of motion is solved for each droplet;
- measurements to define the boundary conditions and to validate the numerical model;
- definition of a droplet emission model including droplet diameters from 0.5 μm to 800 μm emitted by an adult while speaking;
- infectious SARS-CoV-2 risk assessment in a close proximity scenario by considering the contributions of the large droplet and airborne droplet routes

as well as the distance between the speaking infected subject and a susceptible subject.

The assessment has been performed in stagnant air conditions, which represents the worst scenario in terms of virus risk assessment as it could occur also in outdoor environments with negligible wind speed. A representation of the case study is reported in Figure 7.1:

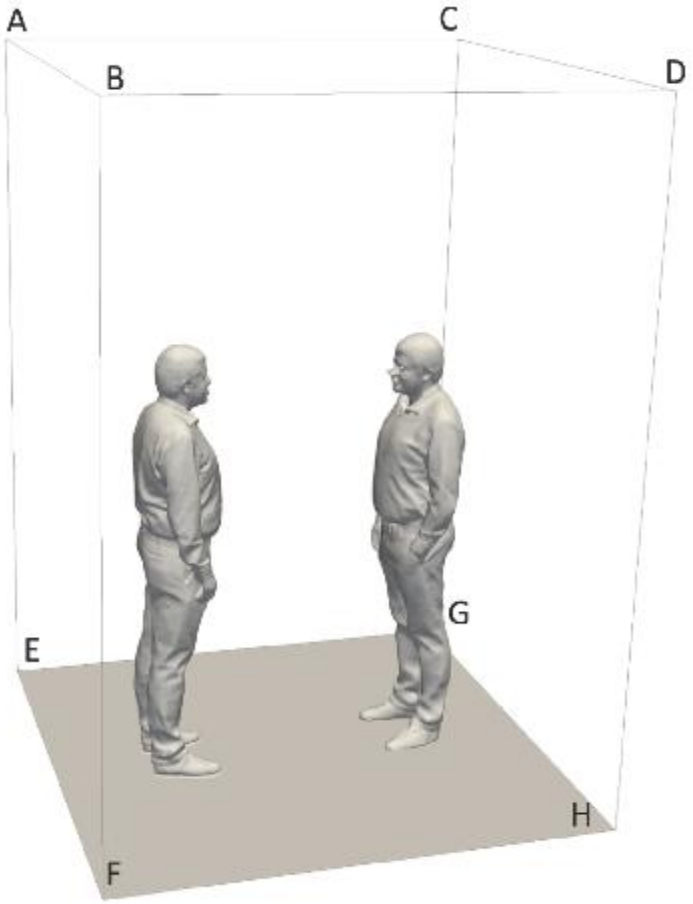

Figure 7.1. Representation of the computational domain in which the emitter is on the left and the receiver is on th right, while the external surfaces have been made transparent

A schematization of the surfaces of interest of the two studied subjects is presented in Figure 7.2: the emitter and receiver's mouth were modelled with the same dimensions a circle of 1.13 cm diameter- while nostrils and eyes surfaces were considered for the receiver, thus considering all the susceptible surfaces for the infection. Moreover, the sinusoidal boundary conditions of the emitter in Figure 7.2 are graphed. The velocity profiles were selected based on a proper literature review and in Figure 7.2 the velocity profiles of the breathing activity are reported alongside

the speaking velocity, represented by the two peak velocities in the first sinusoidal curve.

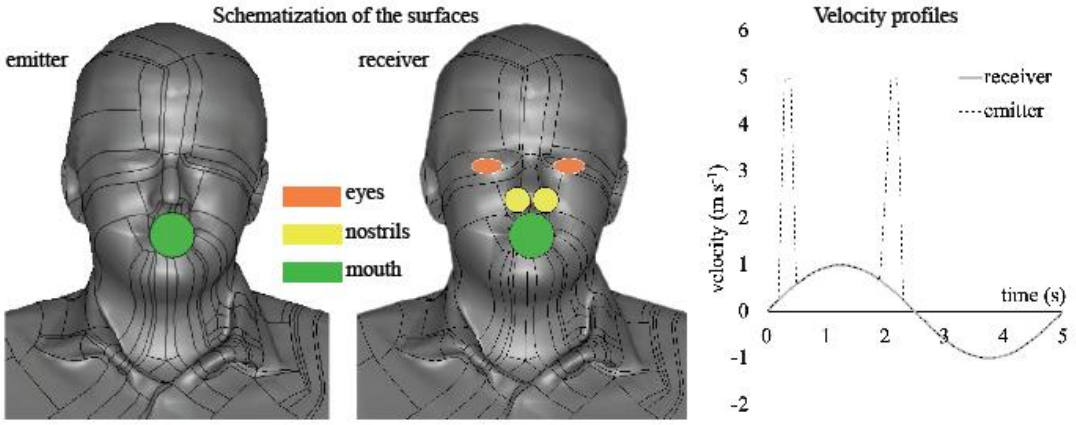

Figure 7.2 Schematization of the surfaces of interest for the emitter and receiver (eyes, nostrils, and mouth) and the transient velocity profile adopted as a boundary condition at the emitter and receiver mouths.

7.2.1 Particle Image Velocimetry experimental investigation

An experimental campaign was conducted in the laboratories of TU Delft to study the fluid dynamics of respiratory activity and validate the results of numerical simulations. The experimental setup included an sCMOS camera from LaVision (2560 x 2160 px) paired with a Nikon objective lens (35 mm focal length), an Nd:YAG Quantel laser (Evergreen, 200 mJ per pulse), and a smoke generator. A laser sheet, 2-3 mm thick, was positioned below the subject's mouth and passed through the mid-plane. The sCMOS camera was located 80 cm from the laser sheet at the height of the subject's mouth, with the objective's axis perpendicular to it. The image magnification was 0.05, providing a field of view of 30 cm (height) by 36 cm (width), and the resolution was 0.14 mm per pixel. Images were captured in frame-straddling mode (double frame, single exposure) at a rate of 10 Hz, with a time interval of 500 µs between frames. A sketch of the experimental setup is available in Figure 7.3.

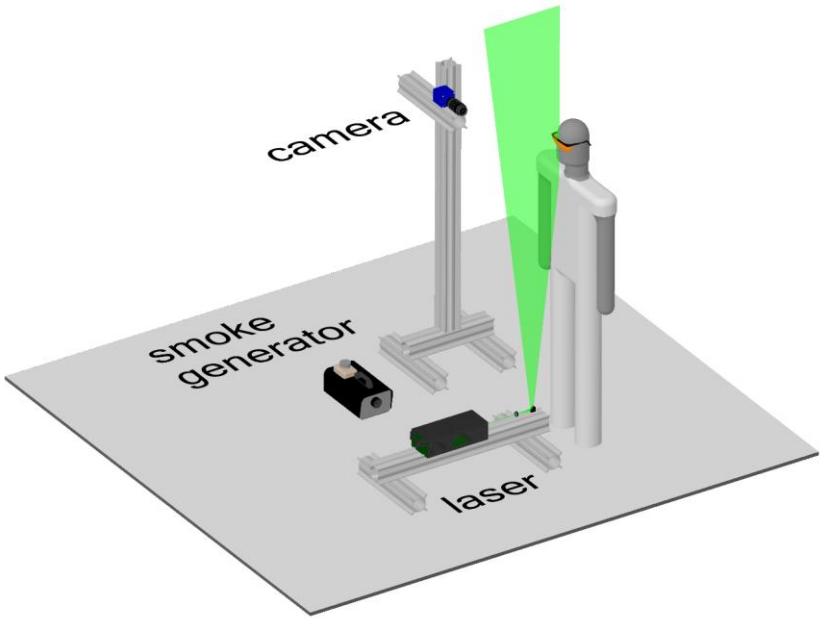

Figure 7.3 The Particle Image Velocimetry experimental setup conducted in the TU Delft facilities

The male subject, 32 years old, 1.84 meters tall, and weighing 80 kilograms, wore safety goggles and sat behind a black screen with a 5 cm diameter opening for exhaling. A 3 cm long cylinder with the same diameter was placed at the opening to position the head and block the laser light from below. The subject's head was positioned so that the nose lightly touched the upper surface of the cylinder, ensuring that breathing through the nose did not affect the measured flow velocities. The subject and the setup were enclosed in a black tent (approximately 15 m3) to contain the smoke. The smoke was generated by turning the smoke generator on for about 2 seconds with the tent closed, and then waiting for approximately 10 minutes for the smoke to spread evenly and for any flow disturbances caused by the smoke generator to become negligible. Three different respiratory activities were examined: inhaling through the nose and exhaling through the mouth, inhaling and exhaling through the mouth, and speaking. Each activity was recorded for 50 seconds (500 images), which included about five respiratory cycles. The images were analyzed using cross-correlation analysis with DaVis 8.4 software from LaVision. The final interrogation window was 48 x 48 pixels (7 x 7 mm2) with 75% overlap, resulting in approximately 160 x 200 vectors per image. The typical uncertainty of a PIV displacement measurement is 0.1 px [90]; because the velocity magnitude close to the mouth varied in the range of 1–5 m s^{-1} (3–18 px), the uncertainty of the instantaneous velocity is estimated to be within 0.5%–3%.

7.2.2 Droplet emission

The number of droplets exhaled by the infected subject as a function of the diameter per unit time, i.e. the droplet number emission rate (ER_N, droplet s^{-1}), was estimated starting from the number distribution of the droplets emitted by an adult person provided by [91] [92]. The droplet distribution was measured from 0.5 μm to about 1000 μm in close proximity to an adult person's mouth while speaking, to consider the droplet evaporation phenomenon negligible. Such measurement was extremely challenging; indeed, the experimental analysis was performed in a purpose-built wind tunnel (named the expired droplet investigation system, EDIS) applying two separate measurement techniques to cover the entire size range: an aerodynamic particle sizer (up to 20 μm) and a droplet deposition analysis (20–1000 μm). For the sake of brevity, the experimental analyses performed in that study are not exhaustively described here: interested readers can refer to the original papers for further details.

To make the simulations affordable, the droplet distributions [91] [92] were fitted through a simplified distribution. In particular, from the number distribution provided by [91], [92], the volume distribution was calculated considering spherical droplets, and then both number and volume distributions were fitted through simplified distributions made up of seven diameters (i.e. seven size ranges). Because the evaporation phenomenon occurs quickly as soon as the droplets are emitted [85] [93], in the present project, the post-evaporation number and volume distributions were considered in the simulation. To this end, the volume droplet distribution before evaporation (i.e. as emitted) was reduced to that resulting from the quick evaporation, which is the volume fraction of non-volatiles in the initial droplet, here considered equal to 1% [85]. Therefore, the droplet shrinkage due to evaporation reduces the droplet diameter to about 20% of the initial emitted size. Additionally, the shrinking effect is not homogeneous for the entire size range. In particular, as reported in the scientific literature [85] [93], the evaporation is slow for very small droplets (< 1 μm) and quite negligible for large droplets. Therefore, the following evaluation was made:

- The droplets < 1 μm after the evaporation (i.e. droplets < 4.6 μm at emission) were selected and grouped in a single size interval labelled as 1 μm droplet diameter size interval labelled as 1 μm droplet diameter;
- the droplets with a dimension of 4.6-90 μm are considered reduced with a a diameter of 1–19.2 μm after evaporation;
- neglected the evaporation for droplets > 90 μm at emission.

The resulting number and volume distributions are summarized in Table 4.1 and the resulting droplet number (ER_N) and volume (ER_V, pre-evaporation) emission rates are also reported, calculated by multiplying the number (or volume) concentration at each size by the expiration flow rate of a speaking subject while standing (1.0 L s^{-1}, average value measured for an adult by [94]. The total droplet number and volume concentrations are reported in Table 4.1: the total droplet number concentration (0.25 droplet cm^{-3}) is the same before and after evaporation, whereas a small variation was recognizable for the volume concentration (6.27×10^{-5} and 6.19×10^{-5} µL cm^{-3} before and after evaporation, respectively) due to shrinkage of droplets initially < 90 µm. In terms of the number concentration (or emission rate), the contribution of the airborne droplets is 98%, whereas it is only 1% and 0.01% in terms of volume concentration (or emission rate) before and after evaporation, respectively, thus confirming that a reduced number of large droplets mostly contributes to the total volume emitted.

7.2.3 Estimation of the dose received by the susceptible subject and infectious risk assessment

An estimation of the viral load carried out by the droplets exhaled by the infected subject was performed as the product of the droplet volume - under the assumption discussed in the previous section – and the corresponding viral load. The achievement of the infection risk assessment passes by the estimation of the viral load of an infected subject – which can vary in order of magnitude- and for a proper estimation, the viral load spectrum data has to be considered. Furthermore, the probability distribution function of c_v is a function of each c_v value and is represented by a probability of occurrence. Data on the viral load in sputum so far available in the scientific literature [95] [96] [97] can be fitted through a log-normal distribution characterized by average and standard deviation c_v values, as mentioned by the authors [98]. The large and airborne droplet doses of RNA copies (D_{large} and $D_{airborne}$) received by the susceptible subject for each c_v value were calculated as:

$$D_{large}(c_v) = \int_0^T \left(V_{d-large}(t) \cdot c_v\right) dt$$
$$D_{airborne}(c_v) = \int_0^T \left(V_{d-airborne-pre}(t) \cdot c_v\right) dt \quad (7.1)$$

where $V_{d\text{-}large}(t)$ and $V_{d\text{-}airborne\text{-}pre}(t)$ are the doses of airborne droplets inhaled and large droplets deposited as a function of the exposure time (t), and T is the total exposure time.

Nonetheless, considering the RNA's doses received by the susceptible subject, it must be regarded as that:

- the different pathogen concentrations as a function of the droplet diameter;
- the different effectiveness of the two transmission routes in causing infection.

It was found [99], that the concentration of viruses in airborne droplets varies depending on the droplet size, with pathogens being more prevalent in larger droplets, accounting for over 90% of the total. Additionally, a recent study by [64] highlighted the significantly higher dose of SARS-CoV-2 required to produce a similar physiological response when instilled in macaques' mucosa compared to the inhalation route. When combining these effects, the equivalent dose of RNA copies related to the deposition of large droplets is at least one-hundredth of the airborne droplets inhaled. Due to the lack of experimental data on the concentration of SARS-CoV-2 virus as a function of droplet size and the pathological response to SARS-CoV-2 virus instilled in humans' mucosa, the paper opted for a parametric analysis considering a dose of RNA copies related to the deposition of large droplets at one hundredth, one thousandth, and negligible (i.e. no large droplet contribution) concerning the inhalation of airborne droplets. In the scientific literature, the probability of infection has been deeply investigated [95] [96] [97], evaluating the:

$$P_I(c_v) = 1 - e^{-\frac{D_{total}(c_v)}{HID_{63}}} \quad (\%) \tag{7.2}$$

where HID_{63} represents the human infectious dose for 63% of susceptible subjects, i.e. the number of RNA copies needed to initiate the infection with a probability of 63%. For SARS-CoV-2, a HID_{63} value of 7×10^2 RNA copies was adopted based on the thermodynamic-equilibrium dose-response model developed by Gale (2020). Nonetheless, the individual risk of infection (R) of the susceptible subject is calculated by integrating all the possible c_v values, the product between the conditional probability of the infection for each c_v ($P_I(c_v)$) and the probability of occurrence of each c_v value (P_{cv}):

$$R = \int_{c_v} (P_I(c_v) \cdot P_{cv}) dc_v \quad (\%) \tag{7.3}$$

7.3 Results and discussion

In this section, the results of the experimental campaign and the numerical model were reported. The virus risk assessment is performed as a function of the distance between subjects, after defining in the experimental campaign the fluid dynamic of the respiratory activity of subjects. Numerical models developed based on the mathematical model depicted in Chapter 4, are reported in this section and a validation of the modelling activity was conducted through experimental data. Furthermore, based on the integrated approach between thermo-fluid dynamic modelling of exhaled droplets and viral load, an infectious risk assessment is presented for a close proximity scenario represented by a speaking infected subject (emitter) and a susceptible subject (receiver) in the case of a face-to-face orientation and stagnant air conditions.

7.3.1 Particle image velocimetry measurements and numerical results

As reported in Section 7.2.1, an experimental campaign has been carried out at TU Delft's laboratories through the Particle Image Velocimetry technique. PIV measurement results for a mouth-breathing case study provided the necessary information to determine the velocity boundary conditions used in the computational fluid dynamics (CFD) numerical simulations. Experimental (PIV) and numerical (CFD) velocity contours obtained in the sagittal plane, by synchronizing the instant of time for breathing at which the maximum velocity values are reached, are presented in Figure 7.4, whereas PIV and CFD vertical velocity profiles in the sagittal plane at a distance from the emitter mouth equal to 0.10 m and 0.32 m are compared in Figure 7.5. The numerical and experimental peak velocity reported in Figure 7.5 differs by 6% and 7%, respectively measured at a distance of 0.10m and 0.32m. Thus, the CFD numerical model depicted in the previous section could be considered validated for risk assessment purposes.

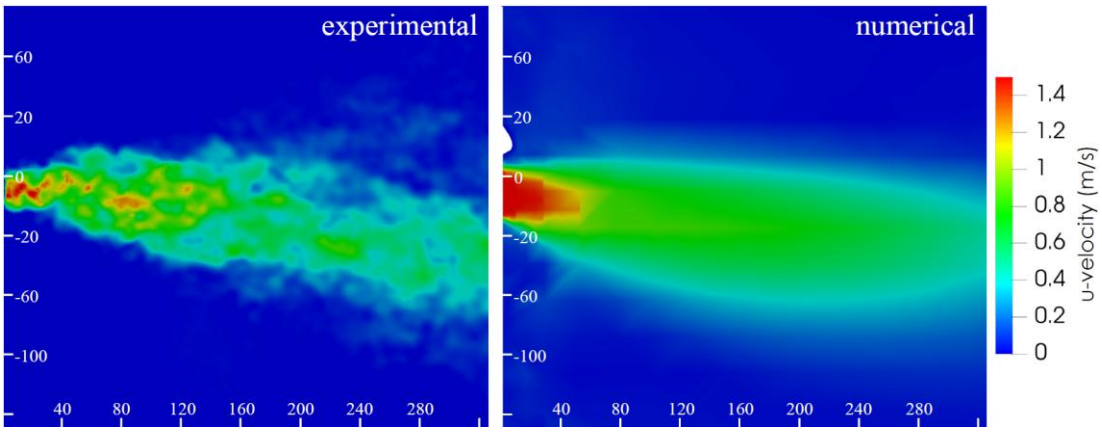

Figure 7.4 Experimental and Numerical velocity contours obtained in a sagittal plane in the instate time of maximum velocity. Scales bars are reported in mm.

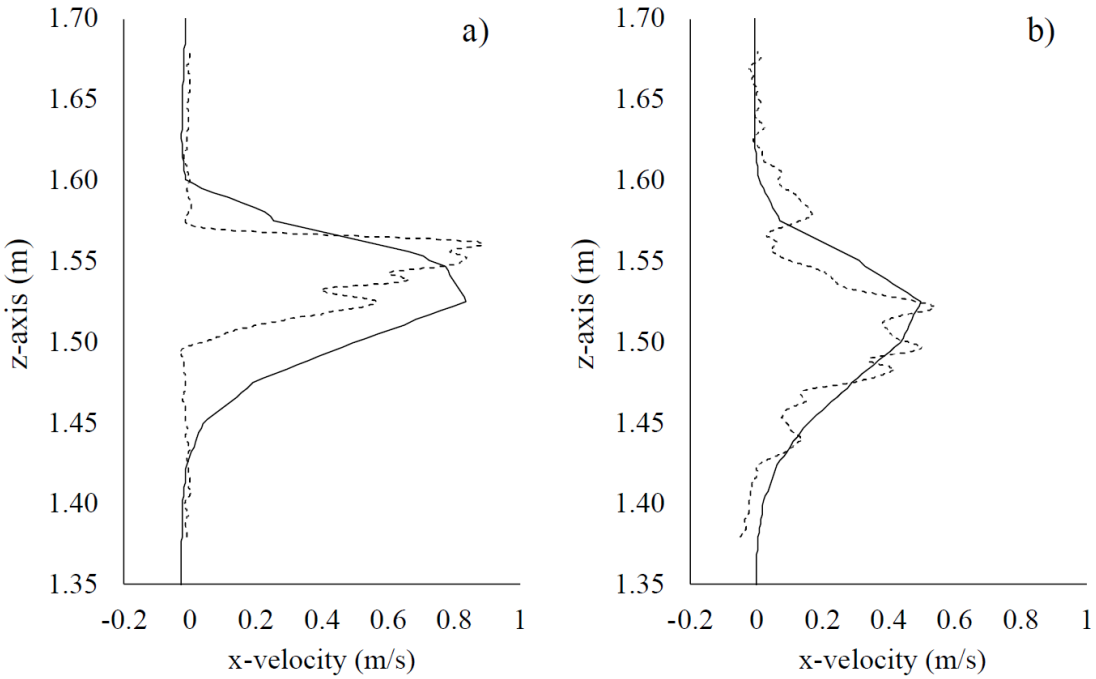

Figure 7.5 Experimental (particle image velocimetry, dotted lines) and CFD (solid lines) velocity profile comparison obtained in a sagittal plane at a distance from the emitter mouth equal to 0.10 m (a) and 0.32 m (b).

7.3.2 Droplet dose received by the susceptible subject

As an example of droplet trajectories and spread, alongside the flow fields obtained through the numerical simulations, Figure 7.6 shows the velocity contours and droplet movement for 5 seconds in six different time steps (reported at the top of every extraction plane).

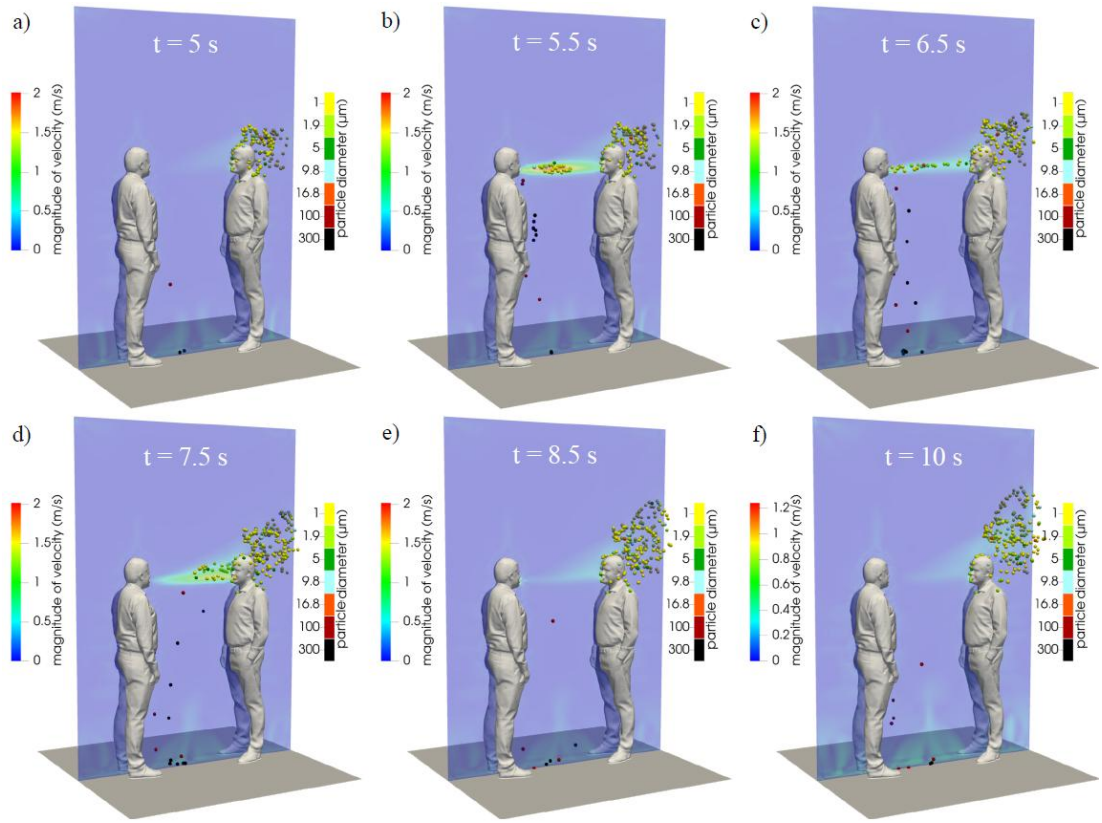

Figure 7.6 Numerical velocity contours during a single breath at a distance of 0.76 m between people: six selected computational times (5, 5.5, 6.5, 7.5, 8.5, and 10 s) are shown

As mentioned in the previous sections, the reported case study represents the interaction between two subjects at a 0.76m mouth distance. For this distance, large droplets fall to the ground without reaching the susceptible surfaces of the receiver, while the receiver partly inhales the airborne droplets. Indeed, airborne droplet movement is deeply affected by the air velocity field and the buoyancy force can't be neglected in this phenomenon. In fact, from the analysis of the three-dimensional transient air velocity field shown in Figure 7.6, it can be observed that when the air velocity from the emitter is low (Figure 7.6a, d, e, f), the effect of buoyancy is evident. At the same time, forced convection dominates when air velocity from the emitter is high. Figure 7.7 shows airborne and large droplet doses (i.e. $V_{d\text{-}airborne\text{-}pre}$, $V_{d\text{-}airborne\text{-}post}$, and $V_{d\text{-}large}$, μL) as a distance function for an exposure time of 1 min. Data were obtained by performing numerical simulations of 15 min and averaging the obtained volumes over an observation time equal to 1 min. The data indicates that larger droplets are most prevalent within a distance of less than 0.6 meters. However, beyond this distance, there is a noticeable decrease because the larger droplets are unable to reach the surfaces of susceptible individuals due to their inertial trajectories.

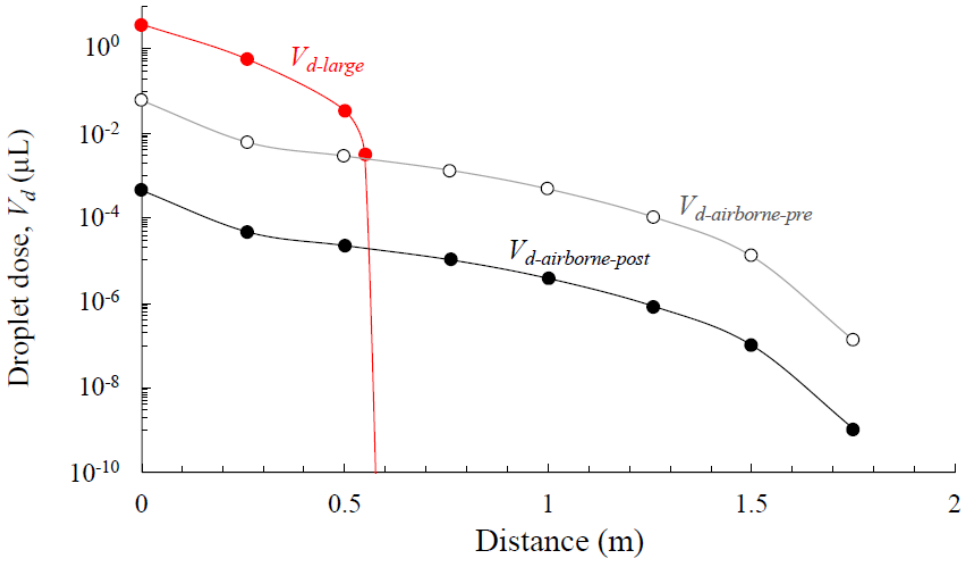

Figure 7.7 1 minute (Vd-large) and airborne droplet doses (Vd-airborne-pre and Vd-airborne-post) received by the susceptible subject by deposition and inhalation respectively

The reported graph shows also the dose of non-evaporated airborne droplets (reported as $V_{d\text{-airborne-pre}}$), thus getting direct information about the infectivity in the interaction process between subjects. For distances greater than 0.6 meters, only the airborne droplet contribution to the total dose received by the infected person is observed. The trajectory of large droplets is mainly affected by their inertia, and this effect is negligible for distances greater than 0.6 meters. The spread of airborne droplets is influenced by the spread angle of the exhaled flow. Specifically, at short interpersonal distances (approximately less than 0.76 meters) from the emission point, where the exhaled airflow angle is still narrow, the dose of airborne droplets decreases according to the 1/L rule, with L representing the interpersonal distance. Meanwhile, for interpersonal distances in the range of 0.76–1.75 meters.

7.3.3 Risk infection assessment as a function of the interpersonal distance

A representation of the risk infection (R) assessment as a function of distance between the infected subject and susceptible subject, for different exposure times of 10 seconds, 1 minute and 15 minutes. The study examines the impact of both deposited large droplets and inhaled airborne droplets. Specifically, it analyzes the risk contribution of the dose of RNA copies associated with the deposition of large droplets. This analysis considers the deposited dose to be equivalent to one hundredth,

one thousandth, or negligible (i.e. no large droplet contribution) in comparison to the dose of RNA copies resulting from the inhalation of airborne droplets.

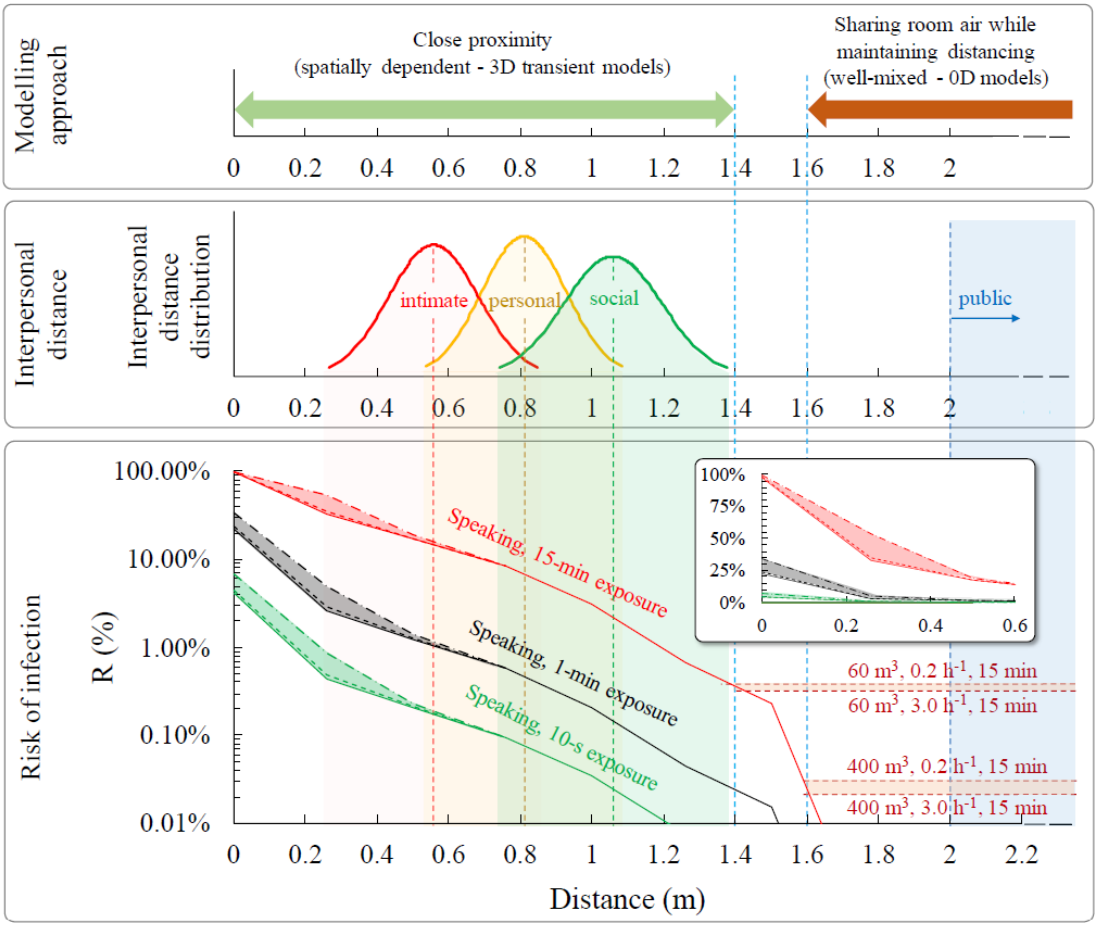

Figure 7.8 Infection risk (R, %) of a susceptible subject as a function of the time of exposure and interpersonal distance from the infected subject.

For close distances (<0.6 m), where large droplets dominate, the infection risk for a 15-minute exposure ranges from over 90% at a few centimetres to over 10% at 0.6 m. The study emphasizes that airborne droplets significantly contribute to infection risk, even at close distances. For example, at 30 cm, the risk ranges from 30% to 50%, depending on the RNA dose from large droplet deposition. This finding challenges the assumption that large droplets dominate infection risk at short distances, showing that airborne droplets remain a major factor. For shorter exposures (e.g., 1 min), the risk ranges from 1% to 30%, and from 0.1% to 7% for 10-second exposures, mainly due to inhaling airborne droplets.

At distances beyond 0.6 m, the infection risk decreases substantially, particularly with increased interpersonal distance and reduced exposure time. For example, the risk drops below 0.1% at 1.5 m for a 15-minute exposure, aligning with the Centers for

Disease and Control Prevention's (CDC) six-foot rule but questioning the WHO's 1-meter guideline. However, the study clarifies that these findings are relevant to environments without viral load accumulation. Indoors, infection risk remains possible, even with distancing. The research also evaluated infection risk when sharing room air in small and large indoor spaces, finding that the risk levels off at 1.4–1.6 m, marking the boundary where simplified models are effective. For practical applications, Zhang et al. (2020) observed typical indoor behavior, finding short-duration close proximity (15 s) with a distance of 0.81 m, resulting in minimal infection risk. Only prolonged close contact significantly increased risk. The study also considered interpersonal distances in different cultural contexts, with varying levels of infection risk based on proximity and duration of exposure. For intimate distances (0.56 m), the risk exceeds 1% after 1-minute exposures, while at personal distances (0.81 m), the risk remains low for short exposures but increases for longer ones. At social distances (1.06 m), a significant risk emerges only after 15 minutes of exposure.

The authors suggest that these findings could help regulatory authorities implement more effective mitigation strategies based on the specific context. They also highlight limitations in their study, such as the need for further validation of their models, consideration of surface transmission, and the effects of turbulence on droplet transmission. Despite these limitations, the study's results are supported by previous research and offer valuable insights into infection risk modelling.

7.4 Conclusions

In this chapter, the behaviour of airborne particle transmission in a close contact scenario was evaluated through three-dimensional CFD models. The results of this study highlight the dominant role of airborne droplets (< 100 μm) in infection risk, even at close interpersonal distances (< 0.6 m), indicating a significant risk of transmission at intimate distances (average 0.56 m). Larger droplets contribute to the infection risk only at very close distances, below 0.6 m, as they rapidly settle onto surfaces and lose relevance at greater separations. At personal (0.81 m) and social (1.06 m) distancing, the infection risk is solely attributed to airborne droplets, underscoring their importance in scenarios where larger droplets no longer pose a threat due to gravitational settling.

Additionally, the duration of exposure emerges as a critical factor in infection risk. At intimate distances, even short exposure times (e.g., 10 seconds) result in non-negligible infection risks, whereas at social distances, prolonged exposure (15 minutes

or more) is required for the infection risk to become significant. This finding emphasizes the need to consider proximity and duration when assessing transmission risk.

A possible threshold for safe close-proximity interaction is around 1.5 m, which reduces the infection risk to approximately 0.1%, even during prolonged exposures of 15 minutes. This threshold also marks the boundary beyond which simplified well-mixed models can be used instead of complex, spatially dependent three-dimensional transient CFD analyses. The study demonstrates that similar infection risk values are obtained for short-range close-proximity interactions and long-range shared air exposures when interpersonal distances range between 1.4 m and 1.6 m, further supporting the adoption of 1.5 m as a standard safe distance for close-proximity interactions.

CHAPTER 8. Personal portable air cleaner for the reduction of airborne transmission of respiratory pathogens

8.1 Introduction

The COVID-19 pandemic has emphasized the crucial role of indoor environments in the spread of respiratory viruses. This is primarily due to airborne transmission, the main route for many respiratory infectious diseases[31] . Infected individuals release virus-laden respiratory particles into the air, which can reach high concentrations and lead to secondary infections in susceptible individuals sharing the same enclosed space, even when not in close proximity to the infected person. Unfortunately, public health authorities, such as the WHO and CDC, recognized this transmission route quite late, despite researchers being advised about its significance [44], [84], [100], [101]. Valuable support to reduce the SARS-CoV-2 airborne transmission in indoor environments is represented by the building ventilation. Buonanno et al. [102] recently reported the very first proof of the effect of ventilation against COVID-19 airborne transmission in a large-scale experiment. Enhanced control and precision of HVAC systems do not provide an overall improvement of airborne particle transmission in the indoor environment. Arpino et al. [103] offered insights into the impact of increased ventilation strength during a two-hour lecture given by an infected individual in a lecture room. Their findings revealed that while ventilation does influence the overall distribution of particles in the room, simply enhancing ventilation is insufficient to control the spread of airborne transmission. As a result, this chapter presents an evaluation of a patented portable air cleaner designed to reduce airborne transmission of respiratory pathogens. The device was tested in two different configurations, demonstrating the effectiveness of the fluid dynamic shield. Materials and methods

In this section, an insight into the characteristics of the personal air cleaner is provided, delving through the geometric and the provided airflow characteristics. The device was also numerically tested in two different scenarios of close contact and

shared environment. The goal is to understand if the cleaning device would be able to protect a subject in different scenarios, especially in critical conditions.

8.1.1 Personal air cleaner

The personal air cleaner with patent number 102022000010346 is designed to offer clean air directly to the user's breathing zone, creating a protected space with significantly lower pollutant and respiratory pathogen levels compared to the surrounding room environment. This compact device is based on personalized ventilation and is designed for portability. In Table 8.1, you can see a schematic of the device, highlighting the key dimensions that affect its functionality. The device is battery-powered and draws in air from the surroundings through an inlet. The incoming air then passes through a filtration system that removes airborne and respiratory particles with 100% efficiency, using commercial filters such as HEPA or electrostatic filters for typical respiratory particle sizes. The purified air is released back into the environment through three distinct sections: high-velocity vertical and horizontal sections, as well as a low-velocity section with a high swirl motion.

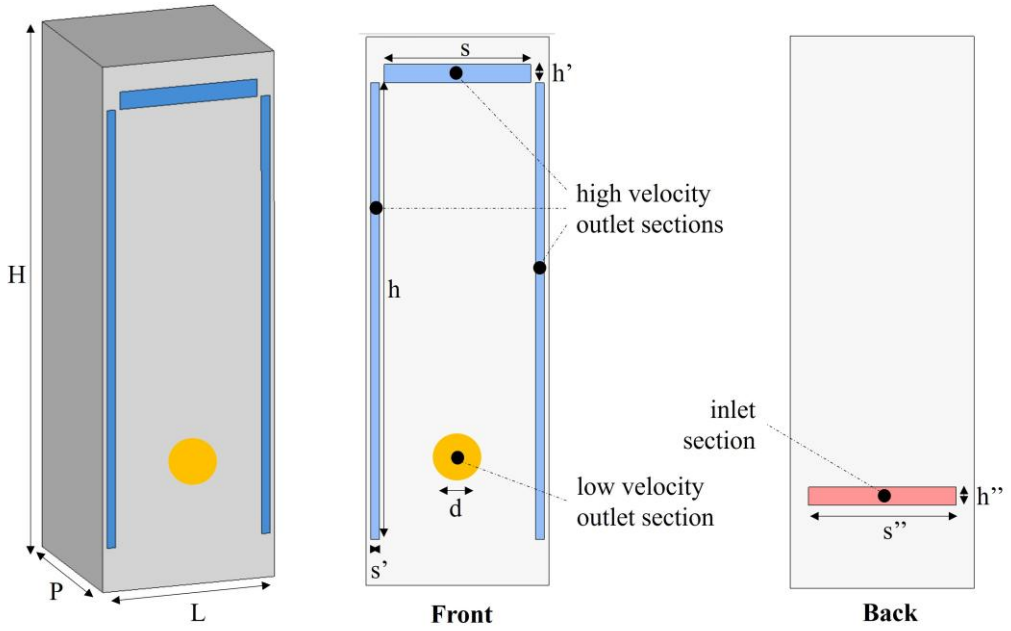

Figure 8.1 Schematic of the portable personal air cleaner.

The portable personal protection device was designed to have a rectangular shape with measurements of 10×10×30 cm. Table 8.1 provides an overview of the main geometrical and operational features of the device. It consists of three high-velocity sections that collectively produce a flow rate of 35.6 $m^3 h^{-1}$, while the low-velocity

section has a flow rate of 2.0 $m^3 h^{-1}$. Consequently, the average air velocities are 3.0 m s^{-1} and 1.8 m s^{-1}, respectively.

Table 8.1 - Main geometric characteristics of the portable personal air cleaner.

Geometrical parameter	size (cm)
length of the air cleaner, L	10
depth of the air cleaner, P	10
height of the air cleaner, H	30
diameter of the low-velocity outlet section, d	2
height of the high-velocity side outlet sections, h	25
width of the high-velocity side outlet sections, s’	0.5
length of the high-velocity upper outlet section, s	8
width of the high-velocity upper outlet section, h’	1
length of the inlet section, s’’	8
width of the inlet section, h’’	1

The air purifier was created to ensure maximum protection when placed on a table or desk at a recommended distance of about 40 cm from the individual. The device's functionality relies on the complex fluid dynamics generated by the specific outlet sections. The clean air jets from the high-velocity sections form a fluid-dynamic shield that creates a sheltered microenvironment capable of shielding an individual from airborne and respiratory particles. Simultaneously, the low-velocity section injects clean air into this microenvironment, enhancing individual protection by preventing particles from re-entering from the surrounding room environment. The low-velocity air flow rate was designed to prevent user discomfort, as the lower outlet velocity and swirl motion result in a very low final airflow velocity reaching the user. Similarly, the high-velocity air flow rates were designed with release angles that do not directly reach the user. Table 8.2 provides a qualitative representation of the release angles and fluid flow directions, while Table 8.2 summarizes the values of the release angles of the jets at the air cleaner outlet sections: here, α represents the upper jet direction with respect to a horizontal plane, while β1 and β2 represent the side jet directions with respect to a vertical plane.

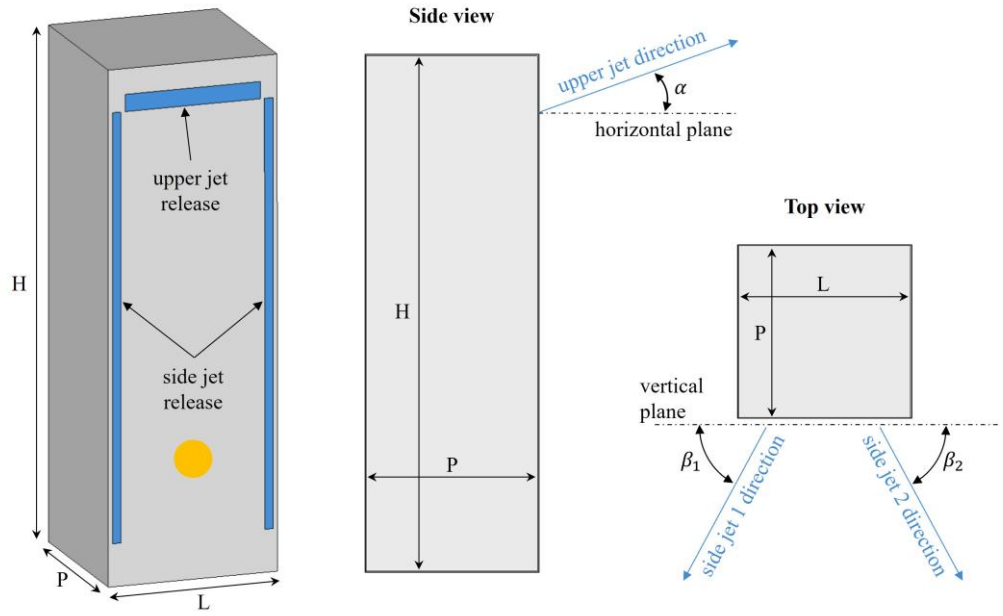

Figure 8.2. Release angles and directions of the air flows exiting the high-velocity sections.

Table 8.2 - Release angles of the jets at the air cleaner outlet sections.

outlet sections	α	β_1	β_2
upper jet release	50°	-	-
side jet 1 release	30°	45°	-
side jet 2 release	30°	-	45°

8.1.2 Personal air cleaner in proximity scenario

The effectiveness of the portable personal protection device was thoroughly examined using the CFD numerical model, as detailed in the previous section and developed by Arpino et al. [31] This model accurately reproduces velocity, temperature, and pressure fields in close proximity scenarios, as well as a susceptible individual's emission, distribution, and inhalation of pathogens. Figure 8.3 depicts the computational domain chosen for assessing the performance of the portable personal air cleaner in close proximity scenarios. This domain simulates an indoor environment where two individuals are seated facing each other at the same table: in this scenario, one subject is infected (the emitter in Figure 8.3), while the other (the receiver in Figure 8.3) is protected by the device. The study was carried out in a time-varying regime to faithfully reproduce the respiratory process (inhalation/exhalation of infectious

respiratory particles) and assumes that the infected subject is speaking loudly toward the susceptible subject, representing the most critical situation. Specifically, face-to-face interactions between subjects (infected emitter and susceptible receiver) of the same height, situated at a distance of 80 cm, were investigated. The susceptible subject was modelled as a mouth-breather, inhaling infectious respiratory particles through the mouth.

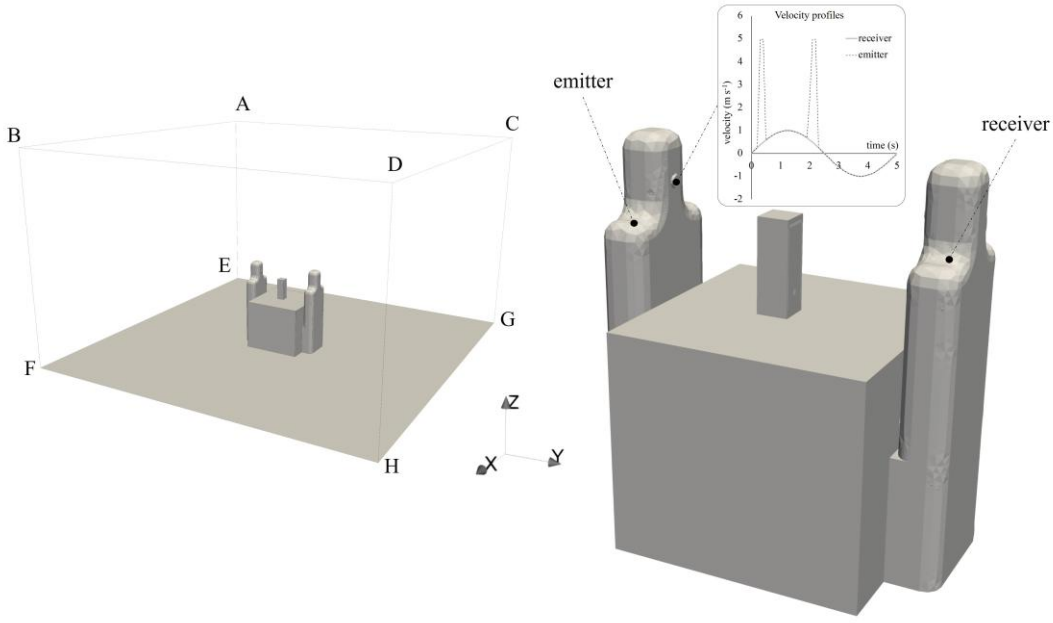

Figure 8.3 - Computational domain considered for close proximity simulations: emitter, receiver, air cleaner, and external surfaces are highlighted.

CFD analyses were conducted adopting the Boundary Conditions (BC) available in Table 8.3. The mouths of the emitter and receiver were modelled as circular surfaces with a diameter of 2 cm [31]. In Figure 8.3, the BC in terms of air velocity at the mouths of the emitter and receiver are also illustrated; in particular, a sinusoidal BC function was adopted on both the emitter and receiver mouths to simulate a real interaction between two subjects [31]. Volumetric flow rates equal to 1 L s^{-1} for speaking and 0.45 L s^{-1} for mouth breathing were imposed as BC [104]. A frequency of 0.2 s^{-1} and an amplitude of 1 ms^{-1} were selected for the sinusoidal velocity profile applied to the receiver mouth assuming a temporal range of 5 s for a full breath [31]. For the speaking emitter subject, velocity peaks of 5 m s^{-1} were mounted on the sinusoidal velocity profile [31], [104].

Table 8.3 - Boundary conditions (BC) adopted for the external surfaces of the computational domain and for the subjects.

Surface	BC for velocity	BC for pressure	BC for temperature
ABEF	$\boldsymbol{u} = 0$	$\partial p/\partial n = 0$	$\partial T/\partial n = 0$
CDGH	$\boldsymbol{u} = 0$	$\partial p/\partial n = 0$	$\partial T/\partial n = 0$
BDFH	$\boldsymbol{u} = 0$	$\partial p/\partial n = 0$	$\partial T/\partial n = 0$
ACEG	$\boldsymbol{u} = 0$	$\partial p/\partial n = 0$	$\partial T/\partial n = 0$
ABCD	$\partial \boldsymbol{u}/\partial n = 0$	$p = 101325$ Pa	$T = 293.15$ K
Emitter mouth	see Figure 8.2	$\partial p/\partial n = 0$	$T = 308.15$ K
Receiver mouth	$\boldsymbol{u} = A \cdot \sin(2\pi f t)$	$\partial p/\partial n = 0$	$T = 308.15$ K

The computational grids were generated using the open-source snappyHexMesh algorithm with hexahedral-based unstructured elements. Three different meshes were tested: Mesh 1 with 927,156 elements, Mesh 2 with 2,904,623 elements, and Mesh 3 with 4,415,668 elements. The grids were refined near the solid surfaces, with a boundary layer region added to capture viscous region gradients, resulting in a maximum non-orthogonality value of approximately 50. Spatial and temporal mesh sensitivity analyses were conducted to determine the optimal grid for reliable results in the studied close proximity scenario. The spatial sensitivity analysis focused on two vertical sections (located in the middle of the emitter's mouth in the x-direction at y=2.1 m and y=2.5 m, as shown in Figure 8.4) to capture the fluid dynamic phenomena affecting the outgoing air jets from the emitter mouth and the outlet surfaces of the personal cleaner.

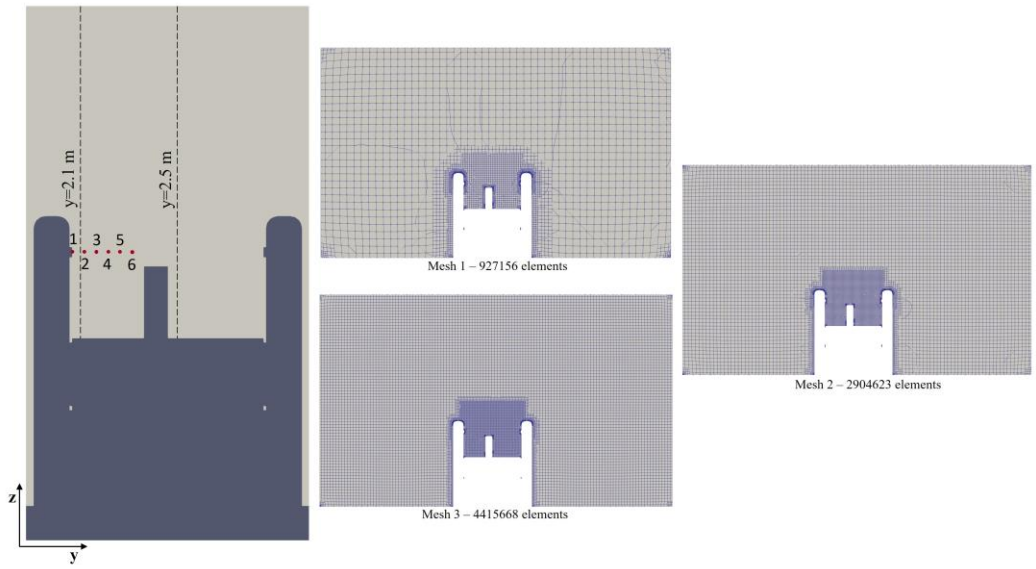

Figure 8.4 - Sections and probes selected for the mesh sensitivity analysis (left); computational grids employed to simulate IRP spread in close proximity (right).

In Figure 8.5, the y-velocity profiles of Mesh 1, 2, and 3 were analysed concerning the z-coordinate in two specific vertical sections at 2.1 m and 2.5 m. When comparing Mesh 1 and Mesh 2, the average percent deviation among the velocity fields was 6.5%, while it was 2.8% when comparing Mesh 2 and Mesh 3.

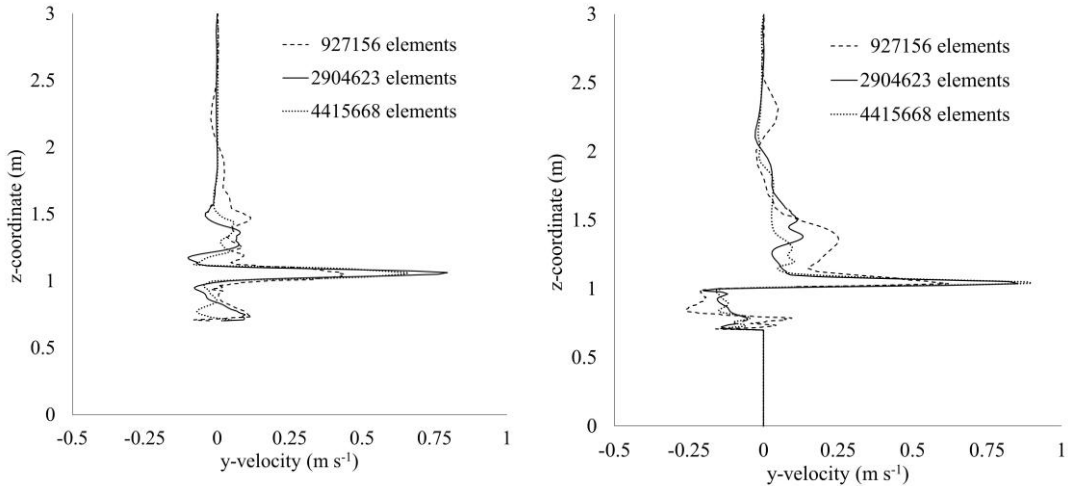

Figure 8.5 – Velocity profiles resulting from simulations at different distances from the emitter's mouth (a) y=2.1 m and (b) y= 2.5 m

Furthermore, a temporal sensitivity analysis was also conducted by collecting the y-velocity trend (every 0.1 seconds over a temporal interval of 100 s) in the six evenly spaced probes (indicated in Figure 8.4) at an interval of 5 cm in y direction starting

from the emitting subject mouth. In Table 8.4, the average percentage deviations in y-velocity obtained when comparing Mesh 1 and Mesh 3 with Mesh 2 are as follows: the total averaged deviations between Mesh 1 and Mesh 2, and between Mesh 2 and Mesh 3, were found to be 4.1% and 2.5%, respectively. Since the percentage deviations among the velocity fields obtained between Mesh 2 and Mesh 3 were both below 5% for the sensitivity analyses performed (spatial and temporal), the simulations were carried out using Mesh 2

Table 8.4 - Average y-velocity percent deviation between Mesh 1 and Mesh 3 concerning Mesh 2 calculated for six evenly spaced probes at intervals of 5 cm in y direction starting from the emitting subject mouth.

Probe number	Probe coordinates (x,y,z)	Average deviation between Mesh 1 and Mesh 2 (%)	Average deviation between Mesh 2 and Mesh 3 (%)
1	(2.50, 2.05, 1.06)	4.0	4.0
2	(2.50, 2.10, 1.06)	3.2	1.7
3	(2.50, 2.15, 1.06)	3.1	1.8
4	(2.50, 2.20, 1.06)	3.9	2.1
5	(2.50, 2.25, 1.06)	4.8	2.5
6	(2.50, 2.30, 1.06)	5.6	2.9
Total averaged values (%)		4.1	2.5

8.1.3 Personal air cleaner in shared environments

The effectiveness of personal air cleaners in shared indoor environments was assessed through numerical simulations. The goal was to study the impact of the personal air cleaner on reducing the concentration of infectious respiratory particles (IRPs) in the user's breathing zone when an infected individual (teacher) speaks during a 2-hour lesson. Given the significant influence of natural and mechanical ventilation on indoor IRP transport, careful consideration was given to selecting the simulated indoor environment. For this purpose, a university lecture room with known dimensions and mechanical ventilation characteristics, as described in Arpino et al. [103], was chosen. The evaluation of IRP spread and distribution within the lecture room during a two-hour lesson was conducted using the same approach.

The room's dimensions are 8.78×7.23×2.88 m in the x, y, and z directions. It consists of four rows for a maximum of 24 seated students and one main desk for the teacher. The HVAC system, situated at the top of the room, is equipped with eight helical swirl diffusers and three rectangular grilles, each measuring 0.182 m2, which

serve as exhaust sections located on the room's eastern wall at a height of 2.50 m. The HVAC system ensures an air exchange rate of 7.5 h-1 within the room. Figure 8.6, the inlet and outlet sections in the computational domain are indicated in green and red, respectively, while other boundary patches, shown in transparent grey, are modelled as walls. The teacher's mouth was represented as a cylinder with a radius of 0.021 m, positioned at a height of 1.60 m just behind the main desk in the room. The constant average velocity, which was set as a boundary condition for the injector, corresponds to the average of the sinusoidal values during exhalation and inhalation as documented by Abkarian et al. [105] and Cortellessa et al. for speaking activities. In terms of the respiratory particle injection direction, random velocity directions at intervals of 0.1 s were applied from the emitter's mouth, considering a conical jet flow with an angle of 22°. The simulation of the eight helical swirl diffusers involved a swirling behaviour with a rotational velocity of 128 rpm, determined through the validation process conducted by Arpino et al. through experimental and numerical comparisons. The flow rates of the eight diffusers, as measured in our previous work, can be found in [103].

Table 8.5 – Flow rates adopted for the eight diffusers placed on the top of the room.

Diffuser	Flow rate ($m^3 s^{-1}$)
1	0.0481
2	0.0388
3	0.0439
4	0.0448
5	0.0451
6	0.0436
7	0.0347
8	0.0444

A hexahedral-based unstructured grid was defined and used to simulate the lecture room, whose clipping is shown in Figure 8.7, by employing the OpenFOAM tool “snappyHexMesh”. The mesh was generated using the same structure and configuration adopted in our previous work [103], in particular, different refinement parameters in the portable personal protection device zone were used. The mesh used to process the shared environment is composed of 3 351 054 cells, with 3.42 max skewness and 58.3 non-orthogonality (Figure 8.7). The choice of this mesh is the result of a sensitivity analysis conducted by comparing three grids of increasing cell

numbers; the grid independence was obtained with the abovementioned grid (the intermediate one), whose errors were <5% from the reference.

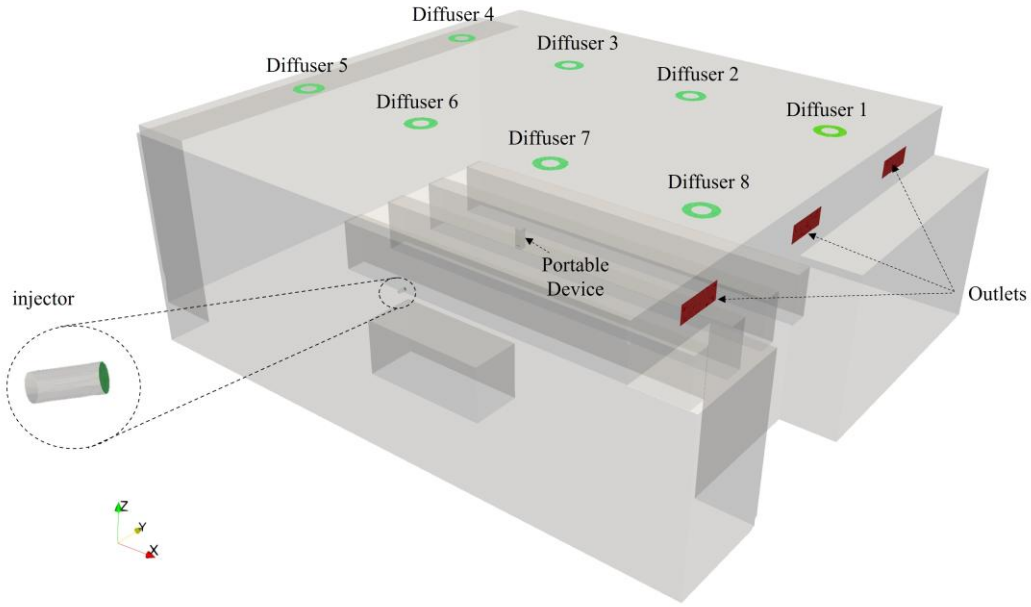

Figure 8.6 - 3D model of the lecture room and patch location of the numerical simulation.

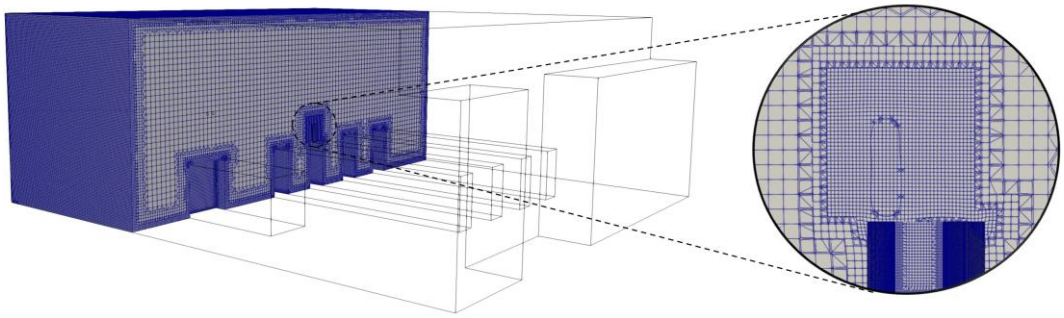

Figure 8.7 - Computational grid (composed by 3 351 054 elements) adopted in the numerical analysis of the university lecture room.

The numerical model is based on the Eulerian-Lagrangian approach described in Section 2. The numerical simulations were conducted in terms of a time-averaged velocity field: to define a proper averaging time interval, eight different numerical probes were placed in the lecture room (Figure 8.8) and a limit of 1% was considered to define the average fields. The first 180 temporal times were not considered in the averaging time, to avoid the fluctuation influence of the velocity field.

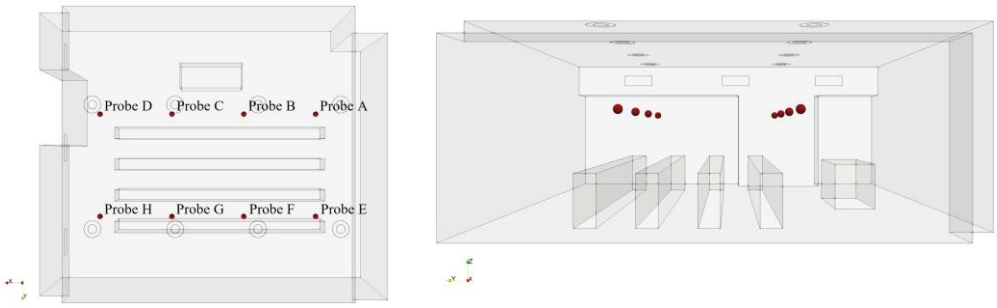

Figure 8.8 – Positioning of the numerical probes adopted to evaluate the time-averaged velocity field.

The adopted boundary conditions for the different surfaces of the domain are detailed in Table 8.6. The boundary conditions of the IRPs were necessary for solving the Lagrangian Particle Tracking model. An escape boundary condition was applied to all surfaces of the computational domain, except for the entry sections, where a rebound boundary condition was used. These conditions also accounted for the adhesion of particles to the walls, as particles in contact with the external surfaces of the domain were assumed to vanish and could not re-enter the computational domain.

Table 8.6 - Boundary conditions (BC) adopted for the different patches of the computational domain considered for the simulation of the lecture room.

surface	**BC for velocity**	**BC for pressure**	**BC for temperature**	**BC for *k***	**BC for ω**	**Lagrangian**
diffusers	see Table 8.5	$\partial p/\partial n = 0$	$T = 293.15$ K	$I = 10\%$	$\ell = 0.07$ L	*Rebound*
outlet sections	$\partial \boldsymbol{u}/\partial n = 0$	$p = 101325$ Pa	$\partial T/\partial n = 0$	$\partial k/\partial n = 0$	$\partial \omega/\partial n = 0$	*Escape*
walls	$\boldsymbol{u} = 0$	$\partial p/\partial n = 0$	$\partial T/\partial n = 0$	standard wall functions		*Escape*
injector	$\lvert u \rvert = 1.11$ m s^{-1}	$\partial p/\partial n = 0$	$T = 308.15$ K	$k = 0.1$ m^2 s^{-2}	$\partial \omega/\partial n = 0$	*Rebound*
air cleaner	see Table 8.3	$\partial p/\partial n = 0$	$T = 293.15$ K	$I = 10\%$	$\ell = 0.07$ L	*Escape*

The CFD model adopted for the numerical analysis in the shared indoor environment was validated by the authors in our previous work [103] by comparing numerical and measured velocities at the eight probes placed inside the domain (Figure 8.8): results of the comparison are illustrated in Figure 8.9 where a good agreement between experimental and numerical data is recognizable. For detailed information about the validation procedure and the experimental apparatus, the interested reader may refer to Arpino et al. [103] where the different numerical performances of two

RANS turbulence approaches were also tested (SST k–ω and RNG k–ε). In particular, the test revealed that the SST k–ω is the best one in predicting fluid flow for the scenario under investigation and this is the reason why we adopted it in the present paper too.

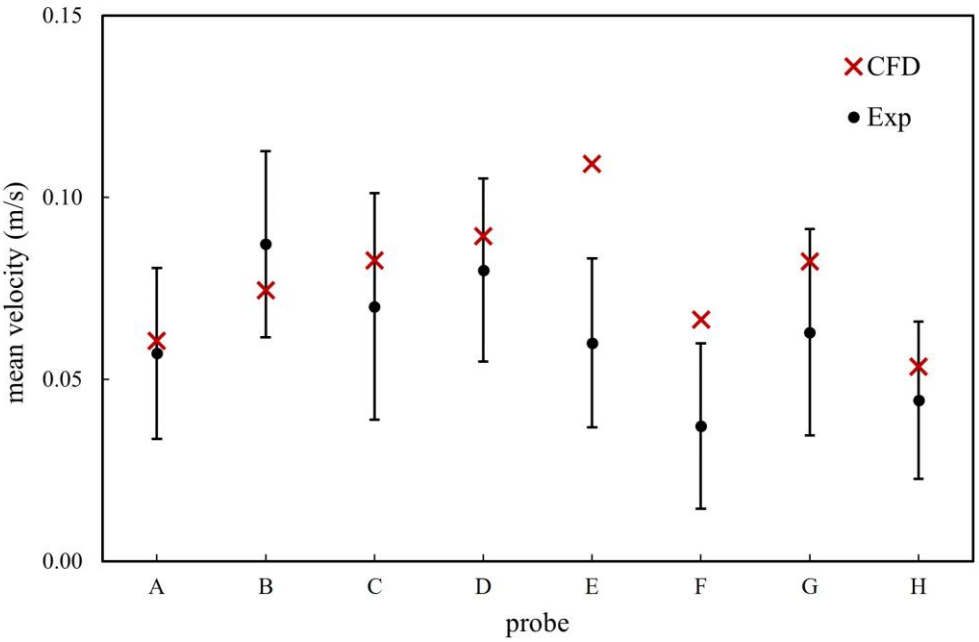

Figure 8.9 – Comparison between mean velocities obtained from numerical simulations and experimental analysis in the eight probes of the domain defined in Figure 8.8.

In order to investigate the effectiveness of the personal air cleaner in terms of relative reduction of the exposure to IRPs during a 2-h lesson, the IRP volume concentration in twenty-four 1.00×1.00×0.88 m (width, height, and depth, respectively) boxes, was provided (Figure 8.10). Each box was meant to represent the average IRP concentration experienced by each student as they were virtually placed on the students' desks and extend one meter from the desk height to analyse the students' breathing areas.

The effectiveness was estimated by comparing the average IRP volume concentration of the boxes with and without the air cleaner. In particular, simulations without air cleaner allowed identification of the box with the highest IRP volume concentration as reported in detail in the results section 8.2.1 (Figure 8.10). Then, a simulation with the air cleaner was performed positioning it in the proximity of the most exposed student/spot previously identified following the recommended (designed) positioning of about 40 cm from the student.

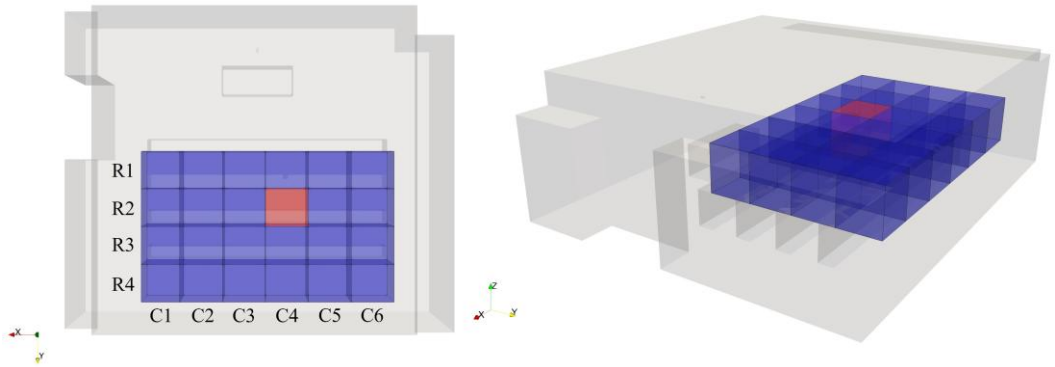

Figure 8.10 – twenty-four volumes used for defining the critical volume for IRP's concentration in the lecture room for a two-hours lesson

8.2 Results and discussion

In this section, the results obtained from the numerical analysis concerning the two case sceanarios of the personal air cleaner device are illustrated and commented. The same logic division is provided for both cases, the Section 8.1.2for the close-proximity scenario and the Section 8.1.3 for the shared environment.

8.2.1 Air cleaner device in the close proximity scenario

The study evaluated the effectiveness of an air cleaner in close proximity by comparing the results of simulations performed with and without the air cleaner. The exposure time was 900 seconds, and the distance between the individuals was 80 cm, with the air cleaner placed at a recommended distance of 40 cm from the receiver. Figure 8.11 illustrates the trajectories of inhaled respirable particles (IRPs) and flow fields obtained from the simulations. The velocity streamlines and IRPs distribution for a breathing period of 5 seconds clearly demonstrate how the high-velocity air flows from the personal air cleaner create a protection zone around the receiver's mouth, deflecting IRPs upwards and preventing their inhalation. Additionally, the low-velocity air jet from the device ensures clean air in the breathing zone, enhancing individual protection. Figure 8.12presents the volumes of IRPs inhaled by the receiver over time, with the air cleaner both turned off and on during the 900-second exposure. The effectiveness of the air cleaner is expressed as the relative reduction in the volume of IRPs inhaled by the receiver, which consistently exceeds 92%, with an average reduction of 96% during the exposure scenario. This demonstrates the high effectiveness of the air cleaner in reducing the inhalation of IRPs.

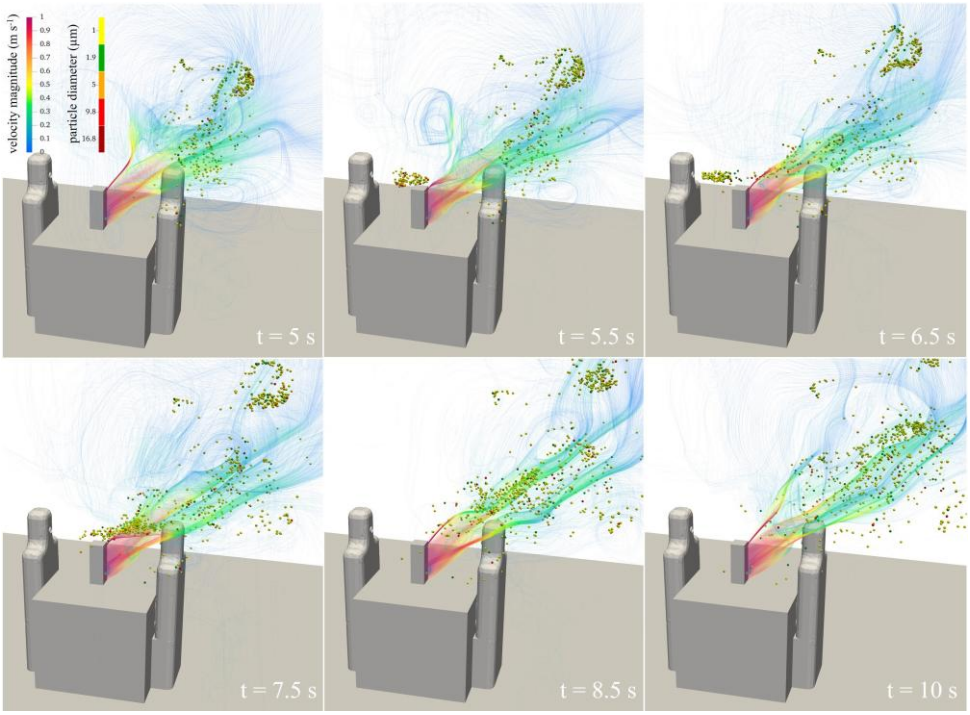

Figure 8.11. Numerical velocity streamlines and IRPs dispersion for six computational times (5, 5.5, 6.5, 7.5, 8.5, and 10 s)

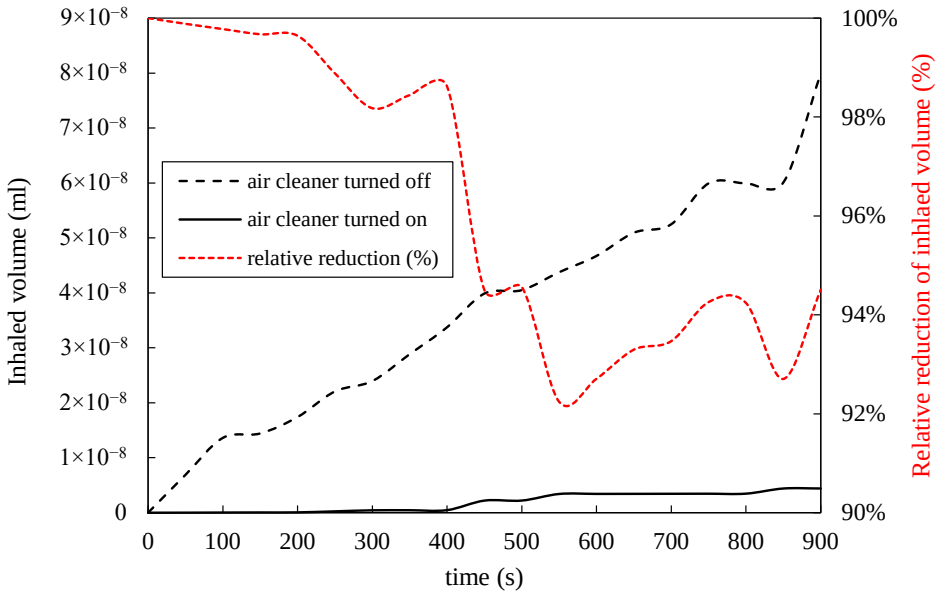

Figure 8.12. Volume of IRPs (ml) inhaled from the receiver subject in the case of personal air cleaner turned off and on and relative effectiveness of the air cleaner (red).

8.2.2 Air cleaner device in the shared environment scenario

The effectiveness of the air cleaner in a shared indoor environment was evaluated by comparing simulation results during a 2-hour lesson, while the air cleaner device was operating or passive. The analysis specifically focused on the volume concentration of infectious respiratory particles (IRPs) within virtual boxes representing student seating positions, while the teacher, impersonates the infected subject speaking the two. The air cleaner was positioned at the recommended 40 cm distance from the receiver, targeting the box with the highest concentration observed in simulations without the air cleaner.

Figure 8.13 illustrates the spatial distribution of IRPs in the classroom under both conditions. The box used for concentration comparison is highlighted in red, clearly demonstrating the reduction in IRP concentration when the air cleaner is activated. The presence of the portable personal protection device significantly alters the IRP flow patterns, especially within the working area and in front of the protection zone. The velocity field generated by the air cleaner reduces the IRP concentration in the breathing zone of the protected student, but simultaneously transports IRPs toward the forward adjacent boxes, leading to increased concentrations in those areas. This redistribution effect is evident in Figure 8.14 and in Table 8.7.

The box with the highest concentration in the absence of the air cleaner (R2C4, with 4.07×10^{-7} ml m^{-3}) exhibited a concentration reduction of approximately 50% (2.08×10^{-7} ml m^{-3}) when the air cleaner was used. Adjacent boxes (R2C3 and R2C5) also saw a decrease of around 30–35%. However, significant concentration increases (up to six times the original values) were observed in the boxes ahead (R1C3 and R1C4), driven by IRP transport induced by the air cleaner. This underscores that the use of a single air cleaner can inadvertently elevate IRP concentrations in the breathing zones of nearby students.

The proposed personal air cleaner offers a promising mitigation strategy for indoor environments where occupants remain stationary. To ensure comprehensive protection and prevent increases in IRP concentrations for adjacent students, air cleaners should be installed at each student's location. The use of multiple air cleaners is not expected to result in adverse interactions, as the terminal velocities of the flow from each device are negligible at the distances typically separating students, as demonstrated in Figure 8.11. The primary aim of this study—validating the protective efficacy of the personal air cleaner in shared spaces—has been successfully achieved. Further research is needed to explore real-world scenarios involving the simultaneous operation of multiple air cleaners to optimize their deployment in practical settings.

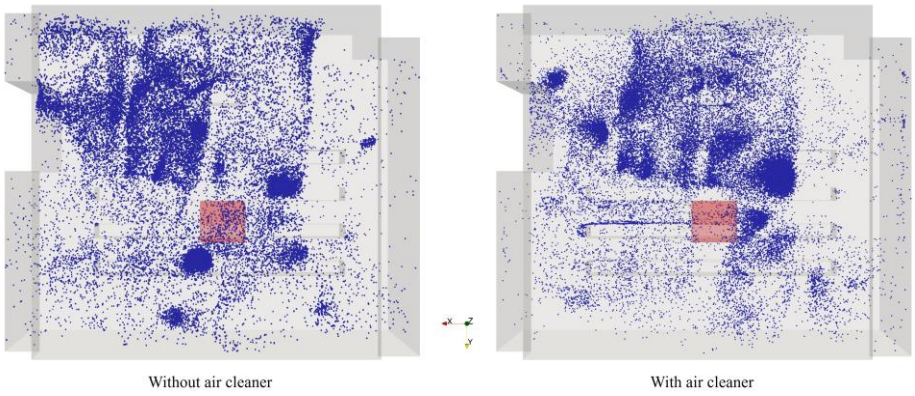

Figure 8.13. Top view of the spatial distribution of IRPs in the lecture room without (left) and with (right) personal air cleaner.

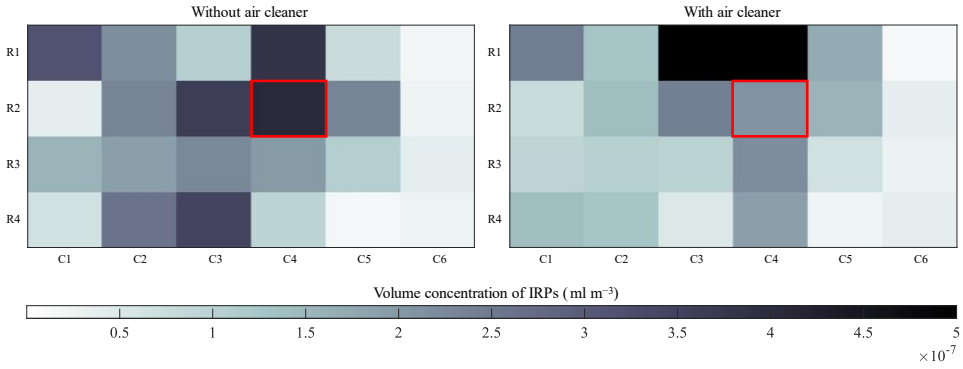

Figure 8.14. Colourmaps of the volume concentration of IRPs (ml m^{-3}) inside the 24 boxes, without (left) and with (right) air cleaner.

Table 8.7. Volume concentrations of IRPs in each of the 24 boxes (ml m^{-3}), with and without air cleaner

Box	Volume concentration of IRPs in each box (ml m^{-3})	
	Without air cleaner	With air cleaner
R1C1	3.16×10^{-7}	2.45×10^{-7}
R1C2	2.16×10^{-7}	1.29×10^{-7}
R1C3	1.07×10^{-7}	6.63×10^{-7}
R1C4	3.82×10^{-7}	6.26×10^{-7}
R1C5	0.76×10^{-7}	1.70×10^{-7}
R1C6	0.21×10^{-7}	0.13×10^{-7}
R2C1	0.39×10^{-7}	0.79×10^{-7}
R2C2	2.32×10^{-7}	1.42×10^{-7}
R2C3	3.63×10^{-7}	2.41×10^{-7}
R2C4	4.07×10^{-7}	2.08×10^{-7}
R2C5	2.32×10^{-7}	1.55×10^{-7}
R2C6	0.24×10^{-7}	0.36×10^{-7}

R3C1	1.54×10^{-7}	0.93×10^{-7}
R3C2	1.90×10^{-7}	1.03×10^{-7}
R3C3	2.25×10^{-7}	0.99×10^{-7}
R3C4	1.95×10^{-7}	2.20×10^{-7}
R3C5	1.07×10^{-7}	0.68×10^{-7}
R3C6	0.38×10^{-7}	0.28×10^{-7}
R4C1	0.67×10^{-7}	1.42×10^{-7}
R4C2	2.61×10^{-7}	1.28×10^{-7}
R4C3	3.47×10^{-7}	0.52×10^{-7}
R4C4	0.97×10^{-7}	1.91×10^{-7}
R4C5	0.19×10^{-7}	0.23×10^{-7}
R4C6	0.27×10^{-7}	0.38×10^{-7}

The use of twenty-four 1.00 m × 1.00 m × 0.88 m virtual boxes proved to be extremely useful in identifying the student/spot characterized by the highest exposure to IRPs volume concentration; nonetheless, the size of these boxes is significantly larger than the breathing zone of the students and, consequently, larger than the protected zone provided by the air cleaner. In other words, the effectiveness of the air cleaner evaluated with this box size could be extremely underestimated, as it should be determined just by considering the actual breathing zone of the student. To address this, a smaller 0.20 m × 0.20 m × 0.20 m box (referred to as the "reduced box") located within the device's airflow outlets was also considered to properly compare the volume concentrations with and without air cleaner. The initial and reduced box size and positioning are highlighted in Figure 8.15, whereas the volume concentrations of IRPs and the corresponding relative reductions obtained with the two boxes are reported in Table 8.8. When the proper (i.e., the reduced) box is considered, the relative reduction of the student's exposure results equal to 99.5%, indicating that the personal air cleaner can significantly protect the susceptible not only in close proximity scenarios but also in shared indoor environments. Thus, the adoption of a personalized air cleaner could be an interesting solution to support general ventilation in managing the airborne transmission of respiratory pathogens in shared indoor environments. It is important to emphasize that these findings apply beyond the specific indoor environment considered. They can be generalized to almost all indoor spaces where users have a nearly fixed position: indeed, the protection of the air cleaner can be undermined only if high-velocity currents of air are present (e.g., droughts). This is not the case for properly designed HVAC systems, whose terminal velocity at head height, for thermal comfort reasons, is expected to be <0.5 m s^{-1}.

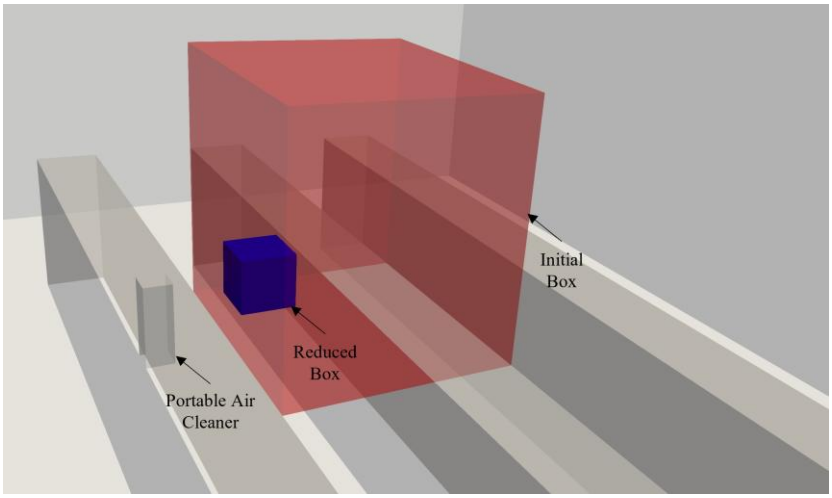

Figure 8.15. Standard and reduced volume were applied to investigate the performance of personal air cleaners.

Table 8.8. Volume concentrations of IRPs (and corresponding relative reductions) obtained from simulations.

Box	Volume concentration of IRPs (ml m^{-3})		Relative reduction of volume concentration
	Without device	With device	
initial box (1.00 m × 1.00 m × 0.88 m)	4.07×10^{-7}	2.08×10^{-7}	49.1%
reduced box (0.20 m × 0.20 m × 0.20 m)	1.25×10^{-6}	5.95×10^{-9}	99.5%

8.3 Conclusion

This chapter highlighted the analysis of the performance of a personal portable air cleaner, from the concept to the numerical testing. The device was tested in two typical exposure scenarios, in close proximity and a shared indoor environment, aiming to reduce the transmission of airborne respiratory particles. The effectiveness of the portable air cleaner was tested in the numerical environment, using the three-dimensional CFD models, which were validated against experimental data. Close-proximity simulations were conducted using a typical face-to-face configuration between the emitter and receiver, while indoor environment simulations were carried out in a university lecture room previously characterized both experimentally and numerically in terms of airflow patterns.

The CFD analysis results showed that in the close-proximity scenario, the air cleaner effectively reduced the volume of inhaled infectious respiratory particles (IRPs) by an average of 96% over a 900-second conversation, with instantaneous reductions consistently exceeding 92%. Similarly, simulations in the shared indoor environment demonstrated an average relative reduction of IRP volume concentration in the breathing zone of 49.1% evaluating the stock box during a 2-hour lesson, while the reduction is more effective (99.5%) while considering a reduced volume of interest, which is representative of the effective breathing area.

In summary, the proposed personal air cleaner provides substantial protection against airborne pathogens in both close-proximity and shared indoor settings, significantly reducing the risk of airborne transmission of respiratory infections. The CFD numerical models developed in the previous Chapters and applied to the evaluation of the effectiveness of the prototyping of the protection device is a very useful tool, to predict the behaviour and movement of the particles within the chosen computational domain.

CHAPTER 9. CONCLUSIONS

This dissertation can be categorized into three distinct parts, seemingly unrelated yet unified by a common objective: ensuring a sustainable future. The significance of this research lies in its pursuit of innovative solutions that address the immediate need for healthier indoor environments while also working towards the long-term goal of achieving a carbon-neutral energy landscape. Both of these aspects are crucial for fostering sustainability, as highlighted by the sustainable development goals established by the United Nations in 2015.

The conclusions and final recommendations for the various sections of this booklet are outlined in the subsections below.

9.1 Part I

The first part of the dissertation (Energy Conversion Systems and Decarbonization Strategies) explores various facets of energy conversion systems and the measurement chain that enables precise flow rate measurements in the transportation sector. This analysis provides insight into carbon dioxide emissions. Throughout both scenarios, the methodology applied is consistent across the chapters, grounded in an experimental-numerical (CFD) approach. The numerical investigation employs an Eulerian framework, addressing the conservation equations of mass, momentum, and energy within the flow field of the examined computational domain.

A Waste-to-Energy plant, located in the middle of Italy, was analyzed in Chapter 2 combining the CFD transient model with the chemical reactions resolution on the grid node through an integrated numerical model developed in the OpenFOAM environment. The boundary conditions of the numerical model were determined through an experimental campaign carried out on both the RDF entering the energy system, analyzing the chemical composition of the syngas at the primary inlet of the plant, and the gas temperature in the combustion chamber in two sections. The findings of the study demonstrated the necessity of using CFD approaches to properly assess the control of the thermodynamic variables within the combustion chamber without entering physically through experimental campaigns. The CFD results show good

reliability and consistency in the validation process and emphazise the importance of the numerical approach in predicting the temperature and partciles distribution in the combustion chamber.

In Chapter 3, the study offers strong evidence for the effectiveness of three-dimensional computational fluid dynamics (CFD) simulations in accurately modelling the performance of single-hole orifice plate flow meters across various operating conditions. These simulations have been rigorously validated against experimental data from the European SAFEST project, demonstrating that the CFD model reliably estimates critical parameters such as discharge coefficients and differential pressures throughout the orifice. However, the research acknowledges certain limitations within the model, particularly regarding the dynamic flow rate predictions at the inlet boundary. To improve the accuracy of these predictions, further investigation is required. This ongoing research aims to refine the model for a more precise representation of fluid behaviour under diverse operational scenarios. The findings highlight the significant value of CFD in optimizing flow metering systems for industrial applications. Accurate measurement is crucial in these settings, as it enhances operational efficiency, minimizes material waste, and reduces environmental impact. As industries increasingly transition toward sustainable practices, the insights gleaned from CFD simulations can greatly contribute to the development of advanced flow measurement tools capable of adapting to innovative fuel types. This adaptability is essential in fostering cleaner, more resource-efficient industrial processes. Consequently, this research not only propels the field of flow metering technology forward but also aligns with broader sustainability objectives. The role of CFD in facilitating more sustainable industrial operations underscores its importance as a tool for promoting environmentally responsible practices, ultimately contributing to a greener future.

9.2 Part II

II part (Indoor air quality: modelling and benchmarking) introduces a defined Lagrangian model for evaluating the behaviour of particles and droplets in a numerical environment. The motivation for this research stems from the studies on SARS-CoV-2 infection risks and particle distribution in indoor settings. The model outlines the structure of a droplet emission framework and analyzes droplets both before and after evaporation in various numerical and experimental scenarios.

Chapter 5 and **Error! Reference source not found.** provide a detailed examination o f both the experimental and numerical analyses of a side mirror model conducted within an open jet wind tunnel at the TU Delft laboratories, employing Particle Tracking Velocimetry (PTV) as the primary measurement technique. The main aim of this benchmarking exercise was to assess the performance of the Lagrangian model in a numerical context. The initial section of the report focuses on the experimental campaign, outlining the methodologies employed, the calibration processes undertaken to ensure accuracy and a comprehensive presentation of the results obtained. This includes an overview of the experimental setup, the wind tunnel conditions, and the data acquisition techniques utilized during the experiment. In the subsequent section, the Lagrangian numerical model is introduced, detailing its theoretical foundation and the specific algorithms used to simulate fluid dynamics around the side mirror model. A comparison between the experimental data and numerical predictions reveals noteworthy findings, demonstrating that the numerical model effectively predicts the flow distribution and mass concentration around the side mirror. These results underscore the model's reliability and highlight its potential applications in aerodynamic analysis and design optimization.

9.3 Part III

The third part (Indoor air quality: applications) of the dissertation shows the analysis of the spread and distribution of virus-laden droplets, emitted by an infected subject, in two distinct situations occurring in indoor environments: a close-distance conversation between two people and the evaluation of a patented personal protection device in close contact scenario and shared environment. These scenarios were chosen for their representation of commonplace situations in our daily lives. The methodology adopted is consistent across the chapters and is based on both experimental and CFD investigations. The numerical model is based on an Eulerian-Lagrangian approach, solving the mass, momentum and energy conservation equations for the air flow (continuous phase) and Newton's equation of motion for each droplet (discrete phase).

In Chapter 7, 3D CFD simulations were conducted to investigate the movement and distribution of droplets emitted by a particle source, mirroring the scenario of an infected individual speaking in front of a susceptible person at a distance of 0.7 meters. This study emphasizes the effectiveness of the numerical tool in predicting the distribution and movement of particles within the computational domain, thereby enabling a comprehensive risk assessment for virus transmission over a specified time

interval. A numerical campaign was carried out in the TU Delft laboratories to evaluate breathing behaviour and validate the velocity profile of the emission source. Overall, the study highlights the significance of this numerical tool in assessing droplet dynamics during common social interactions.

Chapter 8 discusses the development of a portable personal air cleaner designed to manage local airflow patterns in expansive indoor areas and minimize the airborne spread of respiratory pathogens. The device's efficiency is assessed using intricate 3D CFD simulations, which are corroborated by experimental data, across two typical exposure scenarios: close range and shared indoor settings. The air cleaner examined is envisioned as a portable, battery-powered device, engineered with appropriate airflow velocities and angles to generate a complex fluid-dynamic barrier that can safeguard a vulnerable individual from airborne and respiratory particles. Simulations for the close-range scenario considered a standard face-to-face setup between the emitter and receiver, detailed in Chapter 7, while simulations for the indoor environment were based on a university lecture room that had been characterized both experimentally and numerically in various studies by the research group. CFD analysis showed that in the close-range situation, the air cleaner effectively decreased, on average, the volume of inhaled infectious respiratory particles by 96% during a 900-second conversation, with instantaneous reductions exceeding 92%. Simulations conducted in the shared indoor setting indicated an average relative reduction of 99.5% in the volume concentration of infectious respiratory particles in the breathing zone of an exposed individual during a 2-hour lecture. To summarize, the proposed personal air cleaner offers considerable protection to individuals in both close proximity and shared indoor environments, resulting in a decreased airborne transmission of respiratory pathogens. Future investigations will aim to prototype the air cleaner and carry out field tests to evaluate its performance.

Appendix A

A.1 Governing equations of fluid dynamics

The equations governing the motion of a fluid represent mathematical statements of the conservation of mass, momentum, and energy [106], [107], [108].

For a viscous Newtonian, homogeneous and isotropic fluid the *conservative form* of the governing equations can be expressed as:

$$\frac{\partial \rho}{\partial t} + div(\rho \boldsymbol{u}) = 0 \tag{1.1}$$

$$\frac{\partial(\rho u)}{\partial t} + div(\rho u \boldsymbol{u}) = -\frac{\partial p}{\partial x} + \mu\left(\frac{\partial^2 u}{\partial x^2} + \frac{\partial^2 u}{\partial y^2} + \frac{\partial^2 u}{\partial z^2}\right) + \mu\frac{\partial}{\partial x}\left[\left(1 + \frac{\lambda}{\mu}\right) div(\boldsymbol{u})\right] + \sum b_x \tag{1.2}$$

$$\frac{\partial(\rho v)}{\partial t} + div(\rho v \boldsymbol{u}) = -\frac{\partial p}{\partial y} + \mu\left(\frac{\partial^2 v}{\partial x^2} + \frac{\partial^2 v}{\partial y^2} + \frac{\partial^2 v}{\partial z^2}\right) + \mu\frac{\partial}{\partial y}\left[\left(1 + \frac{\lambda}{\mu}\right) div(\boldsymbol{u})\right] + \sum b_y \tag{1.3}$$

$$\frac{\partial(\rho w)}{\partial t} + div(\rho w \boldsymbol{u}) = -\frac{\partial p}{\partial z} + \mu\left(\frac{\partial^2 w}{\partial x^2} + \frac{\partial^2 w}{\partial y^2} + \frac{\partial^2 w}{\partial z^2}\right) + \mu\frac{\partial}{\partial z}\left[\left(1 + \frac{\lambda}{\mu}\right) div(\boldsymbol{u})\right] + \sum b_z \tag{1.4}$$

$$\frac{\partial \rho e_i}{\partial t} + div(\rho e_i \boldsymbol{u}) = -p\,div(\boldsymbol{u}) + \kappa\left(\frac{\partial^2 T}{\partial x^2} + \frac{\partial^2 T}{\partial y^2} + \frac{\partial^2 T}{\partial z^2}\right) + \Phi + S_{e_i} \tag{1.5}$$

Φ is the dissipation function, accounting for the effects due to viscous stresses, whereas the term S_{e_i} represents a source of energy per unit volume per unit time.

Equations (1.1)–(1.5) constitute a set of five partial differential equations involving seven unknown field variables: u, v, w, p, ρ, e_i, T. The two missing equations, required to close the system, can be obtained by determining the relationships existing between the thermodynamic variables (p, ρ, e_i, T) based on the assumption of thermodynamic equilibrium [109]. These relationships are referred to as *equations of state*, and provide a mathematical connection between two or more *point functions* (i.e., thermodynamic

variables) [110]. In most of engineering problems, it is reasonable to assume that the investigated gas behaves as a perfect gas with constant specific heats, for which the following relations hold: $p = \rho \cdot R_{specific} \cdot T$ and $de_i = C_v dT$.

A.1.1 Simplified mathematical models

The conservation equations for mass and momentum are non-linear and strongly coupled, making them challenging to solve. Analytical solutions of the Navier-Stokes equations can be obtained only in a limited number of cases and for very simple geometries with limited practical relevance [107]. In most situations numerical methods must be employed, demanding significant computational resources. To address this issue, simplifications can be made to reduce the computing efforts. Two commonly adopted simplifications are the incompressible flow assumption and the Boussinesq approximation, described below.

INCOMPRESSIBLE FLOW

In many applications the fluid density may be assumed as constant, leading to the assumption of *incompressible flow*. Such approximation is acceptable if the Mach number is below 0.3. In that case, governing equations reduce to:

$$div(\boldsymbol{u}) = 0 \tag{1.6}$$

$$\rho\left[\frac{\partial u}{\partial t} + div(u\boldsymbol{u})\right] = -\frac{\partial p}{\partial x} + \mu\left(\frac{\partial^2 u}{\partial x^2} + \frac{\partial^2 u}{\partial y^2} + \frac{\partial^2 u}{\partial z^2}\right) + \sum b_x \tag{1.7}$$

$$\rho\left[\frac{\partial v}{\partial t} + div(v\boldsymbol{u})\right] = -\frac{\partial p}{\partial y} + \mu\left(\frac{\partial^2 v}{\partial x^2} + \frac{\partial^2 v}{\partial y^2} + \frac{\partial^2 v}{\partial z^2}\right) + \sum b_y \tag{1.8}$$

$$\rho\left[\frac{\partial w}{\partial t} + div(w\boldsymbol{u})\right] = -\frac{\partial p}{\partial z} + \mu\left(\frac{\partial^2 w}{\partial x^2} + \frac{\partial^2 w}{\partial y^2} + \frac{\partial^2 w}{\partial z^2}\right) + \sum b_z \tag{1.9}$$

$$\rho\left[\frac{\partial e_i}{\partial t} + div(e_i\boldsymbol{u})\right] = \kappa\left(\frac{\partial^2 T}{\partial x^2} + \frac{\partial^2 T}{\partial y^2} + \frac{\partial^2 T}{\partial z^2}\right) + \Phi + S_{e_i} \tag{1.10}$$

The energy equation is no longer coupled with other equations (assuming that fluid properties do not change with temperature, otherwise all equations are coupled as for compressible flows). Therefore, we can first solve the continuity and momentum conservation equations to find velocity and pressure fields and then solve the energy equation to yield the temperature distribution. For buoyancy-driven flows, where variations in density due to temperature changes are accounted for in the body force

term of the momentum equation (Boussinesq approximation, see below) all conservation equations again become coupled.

A.1.2 Boussinesq approximation

In flows involving heat transfer, fluid properties typically depend on temperature. Even minor variations in temperature can cause the fluid motion. If the change in density is small, it is possible to treat the density as constant in the unsteady and convection terms and treat it as variable only in the gravitational term. This simplification is referred to as the *Boussinesq approximation*, and assumes that density varies linearly with temperature:

$$\rho = \rho_0[1 - \beta(T - T_0)] \qquad (1.11)$$

where ρ_0 is a reference density, T_0 a reference temperature and β is the coefficient of volumetric expansion. This approximation introduces errors of the order of 1% if the temperature differences are below 15 °C for air [103].

A.2 Physics of turbulent flows

Most flows of engineering interest are turbulent in nature [107], [108], [111]. Turbulence is characterized by unsteadiness and three-dimensionality and causes the appearance in the flow of rotational structures, so-called *turbulent eddies*, with a broad range of length and time scales. In the study of turbulent flows, it is common to refer to an energy cascade, a process where the kinetic energy of larger eddies is transferred to smaller eddies. The cascade starts with the largest eddies (of size *l*), extracting energy from the mean flow and having the highest level of turbulent kinetic energy per unit mass, as illustrated in the energy spectrum graph below (Figure 2.1). These large eddies are identified by the *turbulence Reynolds number* $Re_l = \sqrt{k}l/\nu$. In Figure 2.1, the horizontal axis is the wave number, representing the number of eddies per unit length (i.e., $\propto r^{-1}$, where *r* is the eddy size). The kinetic energy of eddies between the wave numbers κ and $\kappa+d\kappa$ is $E(\kappa)d\kappa$ [112].

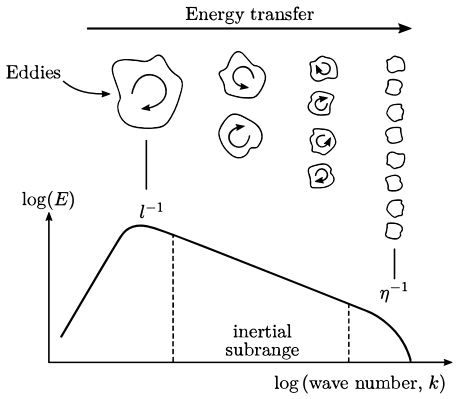

Figure 2.1. Energy spectrum for a turbulent flow [112].

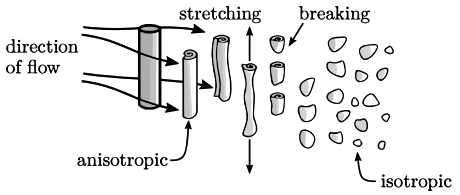

Figure 2.2. Process of large eddies becoming smaller [112].

Large eddies are usually anisotropic due to the way turbulence is generated; their behaviour is dictated by the geometry of the problem domain, the boundary conditions and body forces [106]. For instance, when a fluid flows past a cylinder, it causes the shedding of vortices having a shape similar to the cylinder, i.e., they are elongated in the direction of the cylinder axis (see Figure 2.2).

When moving downstream, through open space, eddies quickly stretch, bend, rotate and break, eventually becoming "blobs" of vorticity. The *turn-over* time of the eddies (i.e., the time for one revolution) decreases with their size. The smaller eddies are nearly isotropic, and have a universal behaviour, dominated by the viscosity ν and by the rate of energy transferred from the large scales ε. The smallest relevant length scales are known as the *Kolmogorov length scale* (η) and are responsible for dissipation. If the Reynolds number is sufficiently high, an intermediate range of scale exists ($\eta \ll r \ll l$, known as the *inertial subrange*) which transfers the energy from the large scales down the cascade (however, negligible dissipation occurs in this range).

There are several numerical methods to model the behaviour of turbulence flows.

These methods can be grouped into three main categories: (i) turbulence models for Reynolds-averaged Navier-Stokes (RANS) equations; (ii) large eddy simulation (LES); (iii) direct numerical simulation (DNS) [106].

The latter consists in directly numerically solving the governing equations over the whole range of turbulent scales (both temporal and spatial). This results in prohibitive computational costs owing to the mesh and time step requirements: the total number of grid points required is of the order of $Re_l^{9/4}$, whereas the time step should be of the

order of η/u_l (where u_l is the large-scale velocity) [113]. For this reason, this approach is mainly used for benchmarking and academic purposes.

With LES, the largest scales of turbulent motion are directly simulated whereas the smaller scales are filtered out and modelled by the so-called subgrid scale models. The underlying principle of this approach is that, while largest scales are affected by the flow conditions and domain boundaries, the smaller scales tend only to be aware of their immediate surroundings and have common characteristic, being thus easier to model. LES reduces the computational cost compared to DNS, and its use is gradually expanding thanks to the advances in computing hardware and parallel algorithms [86].

The method that demands the least computational resources, and for this reason widely applied in both industry and research, is RANS. Here, the governing equations are time-averaged, giving rise to new terms that must be correlated with the mean flow variables through turbulence models. These models are semi-empirical, based on experimental data acquired for simple and controlled flow configurations; as a result, a general-purpose model does not exist and several models have been developed over the years, each suitable for investigating specific categories of fluid flow problems.

A schematic representation of the length scales solved with the different approaches described above is provided in Figure 2.3.

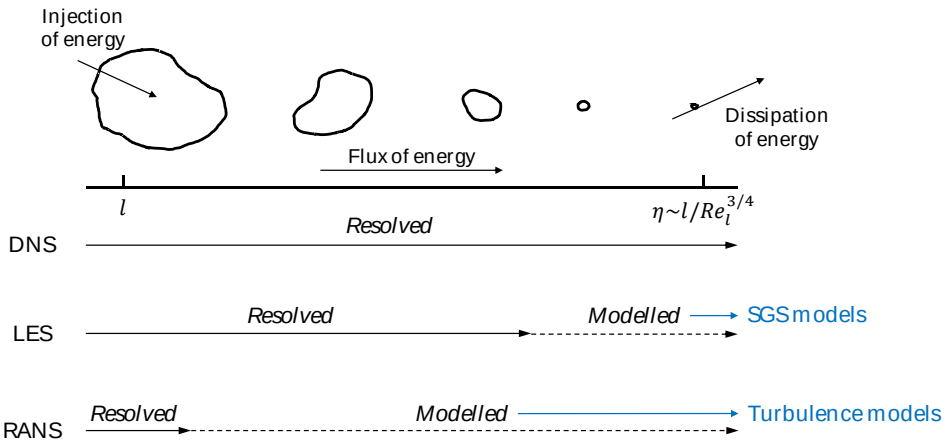

Figure 2.3. Schematic representation of the scales of turbulent motion solved with DNS, LES and RANS approaches (adapted from Bakker [114]).

REYNOLDS-AVERAGED NAVIER-STOKES (RANS) SIMULATIONS

According to the Reynolds decomposition, every flow variable can be written as the sum of a mean (i.e., time-averaged) part $\bar{\varphi}$ and a time-dependent fluctuating part φ' [111]:

$$\varphi(\boldsymbol{x},t) = \bar{\varphi}(\boldsymbol{x}) + \varphi'(\boldsymbol{x},t) \tag{2.1}$$

The time-average of the fluctuating value is zero $\overline{\varphi'} = 0$, and the mean value defined as:

$$\bar{\varphi}(\boldsymbol{x}) = \lim_{T\to\infty} \frac{1}{T} \int_{t}^{t+T} \varphi(\boldsymbol{x},t)\, dt \tag{2.2}$$

Here, T represents the averaging interval. This interval must be large compared to the typical time scales of the fluctuations; thus, we are interested in the limit $T \to \infty$ [107] (see Figure 2.4, left picture).

If the mean flow $\bar{\varphi}$ varies slowly over time, an unsteady approach (URANS) must be employed. Equations (2.1) and (2.2) modify as follows:

$$\varphi(\boldsymbol{x},t) = \bar{\varphi}(\boldsymbol{x},t) + \varphi'(\boldsymbol{x},t) \tag{2.3}$$

$$\bar{\varphi}(\boldsymbol{x},t) = \frac{1}{T} \int_{t}^{t+T} \varphi(\boldsymbol{x},t)\, dt \qquad , \qquad T_1 \ll T \ll T_2 \tag{2.4}$$

where T_1 is the time scale of the rapid fluctuations and T_2 the time scale of the slow variations in the flow, respectively (Figure 2.4, right picture).

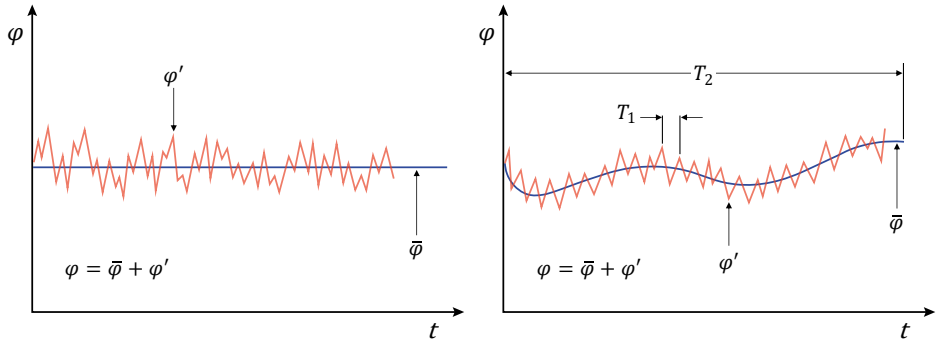

Figure 2.4. Time averaging for a statistically steady turbulent flow (left) and time averaging for an unsteady turbulent flow (right), adapted from Guerrero [109].

Let us now consider the continuity and momentum equations for incompressible flows without body forces:

$$div(\boldsymbol{u}) = 0 \tag{2.5}$$

$$\frac{\partial \rho u}{\partial t} + div(\rho u \boldsymbol{u}) = -\frac{\partial p}{\partial x} + \mu\left(\frac{\partial^2 u}{\partial x^2} + \frac{\partial^2 u}{\partial y^2} + \frac{\partial^2 u}{\partial z^2}\right) \quad (2.6)$$

$$\frac{\partial \rho v}{\partial t} + div(\rho v \boldsymbol{u}) = -\frac{\partial p}{\partial y} + \mu\left(\frac{\partial^2 v}{\partial x^2} + \frac{\partial^2 v}{\partial y^2} + \frac{\partial^2 v}{\partial z^2}\right) \quad (2.7)$$

$$\frac{\partial \rho w}{\partial t} + div(\rho w \boldsymbol{u}) = -\frac{\partial p}{\partial z} + \mu\left(\frac{\partial^2 w}{\partial x^2} + \frac{\partial^2 w}{\partial y^2} + \frac{\partial^2 w}{\partial z^2}\right) \quad (2.8)$$

Reynolds decomposition of the flow variables returns:

$$\boldsymbol{u}(\boldsymbol{x}, t) = \bar{\boldsymbol{u}}(\boldsymbol{x}) + \boldsymbol{u}'(\boldsymbol{x}, t) \quad (2.9)$$

$$p(\boldsymbol{x}, t) = \bar{p}(\boldsymbol{x}) + p'(\boldsymbol{x}, t) \quad (2.10)$$

Substituting expressions (2.9) and (2.10) in equations (2.5)– (2.8, time averaging and rearranging, the incompressible RANS equations are obtained:

$$div(\bar{\boldsymbol{u}}) = 0 \quad (2.11)$$

$$div(\rho \bar{u} \bar{\boldsymbol{u}}) + div\left(\rho \overline{u' \boldsymbol{u}'}\right) = -\frac{\partial \bar{p}}{\partial x} + \mu\left(\frac{\partial^2 \bar{u}}{\partial x^2} + \frac{\partial^2 \bar{u}}{\partial y^2} + \frac{\partial^2 \bar{u}}{\partial z^2}\right) \quad (2.12)$$

$$div(\rho \bar{v} \bar{\boldsymbol{u}}) + div\left(\rho \overline{v' \boldsymbol{u}'}\right) = -\frac{\partial \bar{p}}{\partial y} + \mu\left(\frac{\partial^2 \bar{v}}{\partial x^2} + \frac{\partial^2 \bar{v}}{\partial y^2} + \frac{\partial^2 \bar{v}}{\partial z^2}\right) \quad (2.13)$$

$$div(\rho \bar{w} \bar{\boldsymbol{u}}) + div\left(\rho \overline{w' \boldsymbol{u}'}\right) = -\frac{\partial \bar{p}}{\partial z} + \mu\left(\frac{\partial^2 \bar{w}}{\partial x^2} + \frac{\partial^2 \bar{w}}{\partial y^2} + \frac{\partial^2 \bar{w}}{\partial z^2}\right) \quad (2.14)$$

The term $\overline{u_i' u_j'}$ (in suffix notation), arising from the time-averaging operation, is the so-called *Reynolds stress tensor* $\mathcal{R}_{ij}$[1]. It is clearly symmetric and represents the momentum transfer by the fluctuating velocity field. From Equations (2.11)–(2.14) it is observed that the number of unknown quantities (pressure, three velocity components and six stresses) is larger than the number of equations. As a result, the system of equations is not closed, and the Reynolds stresses need to be appropriately modelled. A common approach used to resolve the problem of closure is the Boussinesq hypothesis, which relates the Reynolds stresses to the mean velocity gradients through an eddy (or turbulent) viscosity μ_T:

[1] A check of the dimensions will show that $\mathcal{R}_{ij}$ is not actually a stress. It must be multiplied by the density ρ to have dimensions corresponding to the stresses.

$$-\rho\left(\overline{u_i' u_j'}\right) = \mu_T\left(\frac{\partial \bar{u}_i}{\partial x_j} + \frac{\partial \bar{u}_j}{\partial x_i}\right) - \frac{2}{3}\rho\delta_{ij}k \qquad (2.15)$$

where δ_{ij} is the Kronecker delta and $k = \frac{1}{2}\overline{u_\iota' u_\iota'}$ is the turbulent kinetic energy per unit mass. The isotropic part of the Reynolds stress tensor is absorbed normally into the pressure term as $\bar{p} = \bar{p} + 2k/3$ [115]. The turbulent viscosity is a property of the flow field and not a physical property of the fluid. The missing equations, required to balance the number of unknowns and yield the solution, are provided by the so-called *turbulence models*.

LARGE EDDY SIMULATIONS (LES)

Instead of time-averaging, large eddy simulation involves the use of a spatial filter to separate the larger eddies (to be resolved) from the smaller ones (to be modelled).

For a general property φ, the filtering operation is usually defined as:

$$\tilde{\varphi}(\boldsymbol{x}, t) = \int_{\mathcal{D}} \mathcal{G}(\boldsymbol{x}, \boldsymbol{x}', \Delta)\varphi(\boldsymbol{x}', t)dx'dy'dz' \qquad (2.16)$$

where $\tilde{\varphi}(\boldsymbol{x}, t)$ is the filtered function; $\mathcal{D}$ is the flow domain; $\mathcal{G}$ is the filter function (usually a Gaussian filter); **x'** is the variable moving in the points surrounding **x**, that is instead the vector coordinate of the position.

Δ is the cutoff width (only eddies with a length scale greater than the cutoff width are resolved), and is often taken as the cube root of the grid cell volume:

$$\Delta = \sqrt[3]{\Delta x \Delta y \Delta z} \qquad (2.17)$$

Δx, Δy, Δz are the grid lengths in the x, y and z directions respectively.

Let us now focus our attention on incompressible flows, for the sake of simplicity. The filtered continuity and momentum conservation equations for a Newtonian fluid are the following (body forces are also neglected):

$$div(\rho\widetilde{\boldsymbol{u}}) = 0 \qquad (2.18)$$

$$\frac{\partial(\rho\tilde{u})}{\partial t} + div(\rho\tilde{u}\widetilde{\boldsymbol{u}}) = -\frac{\partial \tilde{p}}{\partial x} + \mu\left(\frac{\partial^2 \tilde{u}}{\partial x^2} + \frac{\partial^2 \tilde{u}}{\partial y^2} + \frac{\partial^2 \tilde{u}}{\partial z^2}\right) \qquad (2.19)$$

$$\frac{\partial(\rho\tilde{v})}{\partial t} + div(\rho\tilde{v}\widetilde{\boldsymbol{u}}) = -\frac{\partial \tilde{p}}{\partial y} + \mu\left(\frac{\partial^2 \tilde{v}}{\partial x^2} + \frac{\partial^2 \tilde{v}}{\partial y^2} + \frac{\partial^2 \tilde{v}}{\partial z^2}\right) \qquad (2.20)$$

$$\frac{\partial(\rho\tilde{w})}{\partial t} + div(\rho\widetilde{w\boldsymbol{u}}) = -\frac{\partial\tilde{p}}{\partial z} + \mu\left(\frac{\partial^2\tilde{w}}{\partial x^2} + \frac{\partial^2\tilde{w}}{\partial y^2} + \frac{\partial^2\tilde{w}}{\partial z^2}\right) \quad (2.21)$$

Equations (2.18)–(2.21) must be solved to yield the filtered velocity ($\tilde{u}$, $\tilde{v}$, $\tilde{w}$) and pressure ($\tilde{p}$) fields. However, the convective terms $div(\rho\widetilde{u\boldsymbol{u}})$, $div(\rho\widetilde{v\boldsymbol{u}})$ and $div(\rho\widetilde{u\boldsymbol{u}})$ requires further manipulation to get the solution. One can write:

$$div(\rho\widetilde{u_i\boldsymbol{u}}) = div(\rho\tilde{u}_i\tilde{\boldsymbol{u}}) + \left(div(\rho\widetilde{u_i\boldsymbol{u}}) - div(\rho\tilde{u}_i\tilde{\boldsymbol{u}})\right) \quad (2.22)$$

The difference $\widetilde{u_i\boldsymbol{u}} - \tilde{u}_i\tilde{\boldsymbol{u}}$ is modelled as:

$$\tau_{SGS} = -\rho(\widetilde{u_i\boldsymbol{u}} - \tilde{u}_i\tilde{\boldsymbol{u}}) \quad (2.23)$$

providing the momentum equations solved in LES:

$$\frac{\partial(\rho\tilde{u})}{\partial t} + div(\rho\tilde{u}\tilde{\boldsymbol{u}}) = -\frac{\partial\tilde{p}}{\partial x} + \mu\left(\frac{\partial^2\tilde{u}}{\partial x^2} + \frac{\partial^2\tilde{u}}{\partial y^2} + \frac{\partial^2\tilde{u}}{\partial z^2}\right) + div(\tau_{SGS}) \quad (2.24)$$

$$\frac{\partial(\rho\tilde{v})}{\partial t} + div(\rho\tilde{v}\tilde{\boldsymbol{u}}) = -\frac{\partial\tilde{p}}{\partial y} + \mu\left(\frac{\partial^2\tilde{v}}{\partial x^2} + \frac{\partial^2\tilde{v}}{\partial y^2} + \frac{\partial^2\tilde{v}}{\partial z^2}\right) + div(\tau_{SGS}) \quad (2.25)$$

$$\frac{\partial(\rho\tilde{w})}{\partial t} + div(\rho\tilde{w}\tilde{\boldsymbol{u}}) = -\frac{\partial\tilde{p}}{\partial z} + \mu\left(\frac{\partial^2\tilde{w}}{\partial x^2} + \frac{\partial^2\tilde{w}}{\partial y^2} + \frac{\partial^2\tilde{w}}{\partial z^2}\right) + div(\tau_{SGS}) \quad (2.26)$$

τ_{SGS} stresses are called the *subgrid-scale Reynolds stresses* and represent the momentum flux caused by the action of the unresolved scales [107]; they are approximated by the so-called *subgrid-scale models.*

THE FINITE VOLUME METHOD (FVM)

The governing equations described in the preceding sections are converted into linear algebraic equations and solved using the open-source code OpenFOAM, which is based on the finite volume formulation.

The Finite Volume Method is a widely employed technique in computational fluid dynamics, known for its inherent conservation properties and its ability to be used on arbitrary computational grids [116]. Like other numerical methods, the FVM transforms the set of partial differential equations into a system of algebraic equations; however, the discretisation process is different and is based on integrating the governing equations over control volumes that discretise the computational domain [106].

The starting point for applying the FVM is the convection-diffusion equation, which for a general property per unit mass φ appears as follows [106]:

$$\underbrace{\frac{\partial(\rho\varphi)}{\partial t}}_{transient\ term} + \underbrace{div(\rho\varphi\boldsymbol{u})}_{convective\ term} = \underbrace{div(\Gamma\ grad\varphi)}_{diffusive\ term} + \underbrace{S_{\varphi}}_{source\ term} \quad (2.27)$$

This equation can take the form of the equation of conservation of mass, momentum or energy by appropriately choosing φ, the diffusion coefficient Γ and the source term S_{φ}.

Integration of Equation (2.27) over a three-dimensional control volume (CV) returns:

$$\int_{CV} \frac{\partial(\rho\varphi)}{\partial t}\, dV + \int_{CV} div(\rho\varphi\boldsymbol{u})\, dV = \int_{CV} div(\Gamma\ grad\varphi)\, dV + \int_{CV} S_{\varphi}\, dV \quad (2.28)$$

The convective and diffusive terms are rewritten as integrals over the entire bounding surface of the CV *(A)*, by using the Gauss's divergence theorem, which for a generic vector **a** states:

$$\int_{CV} div(\boldsymbol{a})\, dV = \int_{A} \boldsymbol{n} \cdot \boldsymbol{a}\, dA \quad (2.29)$$

where $\boldsymbol{n} \cdot \boldsymbol{a}$ is the component of vector $\boldsymbol{a}$ in the direction of the vector $\boldsymbol{n}$ normal to the surface element dA.

Applying Gauss's divergence theorem, Equation (2.28) can be thus written as:

$$\frac{\partial}{\partial t}\int_{CV} \rho\varphi\, dV + \int_{A} \boldsymbol{n} \cdot (\rho\varphi\boldsymbol{u})\, dA = \int_{A} \boldsymbol{n} \cdot (\Gamma\ grad\varphi)\, dA + \int_{CV} S_{\varphi}\, dV \quad (2.30)$$

In words:

Rate of increase of φ inside the CV + **Net rate of decrease of φ due to convection across the CV boundaries** = **Net rate of increase of φ due to diffusion across the CV boundaries** + **Net rate of creation of φ inside the CV**

Equation (2.30) is thus a statement of the conservation of property φ for a finite size CV.

FVM FOR DIFFUSION PROBLEMS

The governing equation for diffusion problems can be derived from the general transport equation (2.27) for a property φ by deleting the convective term. This gives:

$$div(\Gamma\ grad\varphi) + S_{\varphi} = \frac{\partial(\rho\varphi)}{\partial t} \quad (2.31)$$

In the present discussion, the numerical techniques to discretise the governing equations are introduced for the sake of simplicity with reference to a steady state 1D case; however, the methodology adopted here has general validity and can be easily extended to 2D and 3D problems. Figure 2.5 displays a generic 1D domain with the terminology commonly adopted in the finite volume formulation.

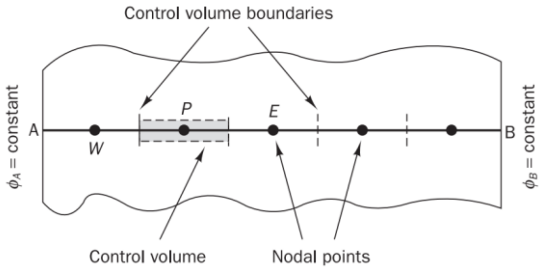

Figure 2.5. Generic 1D computational domain [106].

For steady state, one-dimensional problems, Equation (2.31) modifies as follows:

$$\frac{d}{dx}\left(\Gamma\frac{d\varphi}{dx}\right)+S=0 \tag{2.32}$$

The first step for the discretisation of the governing equation is the definition of the computational grid, obtained by dividing the domain into discrete control volumes. For a general nodal point *P*, the control volume is depicted in Figure 2.6. The left and right nodes are identified by the letters *W* and *E*, respectively; faces of the control volume are referred to by the letters *w* and *e*. Distances of interest for the analysis, and the width of the CV, are indicated in Figure 2.6 as well.

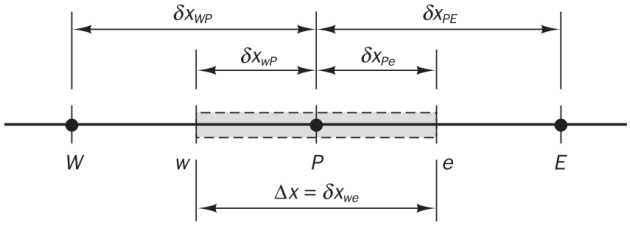

Figure 2.6. Usual convention of CFD methods [106].

The next step is the integration over the CV of the terms from Equation (2.32) and the application of Gauss's theorem:

$$\int_{\Delta V}\frac{d}{dx}\left(\Gamma\frac{d\varphi}{dx}\right)dV+\int_{\Delta V}S\,dV=\left(\Gamma A\frac{d\varphi}{dx}\right)_e-\left(\Gamma A\frac{d\varphi}{dx}\right)_w+\bar{S}\Delta V=0 \tag{2.33}$$

Here A is the cross-sectional area of the CV face, ΔV is the volume and $\bar{S}$ is the average value of source S over the CV.

Assuming that the generic property φ is continuous, differentiable, with bounded and continuous derivatives, it is possible to expand the function $\varphi(x)$ into a Taylor series and express φ_E and φ_P in terms of φ_e:

$$\varphi_E = \varphi_e + \left.\frac{d\varphi}{dx}\right|_e \delta x_{eE} + \left.\frac{d^2\varphi}{dx^2}\right|_e \frac{\delta x_{eE}^2}{2} + o(\delta x^3) \qquad (2.34)$$

$$\varphi_P = \varphi_e - \left.\frac{d\varphi}{dx}\right|_e \delta x_{Pe} + \left.\frac{d^2\varphi}{dx^2}\right|_e \frac{\delta x_{Pe}^2}{2} + o(\delta x^3) \qquad (2.35)$$

where the symbol $o(\delta x^3)$ indicates that the order of magnitude of the remaining terms is δx^3. Subtracting expressions (2.34) and (2.35) term by term yields:

$$\varphi_E - \varphi_P = \left.\frac{d\varphi}{dx}\right|_e (\delta x_{eE} + \delta x_{Pe}) + o(\delta x^2) \qquad (2.36)$$

from which, considering that $\delta x_{eE} + \delta x_{Pe} = \delta x_{PE}$ and neglecting the term $o(\delta x^2)$, the approximation of the differential operator using the central differencing scheme, second–order accurate[2], is obtained:

$$\left.\frac{d\varphi}{dx}\right|_e = \frac{\varphi_E - \varphi_P}{\delta x_{PE}} \qquad (2.37)$$

A similar expression is obtained for the derivative at the interface *w*:

$$\left.\frac{d\varphi}{dx}\right|_w = \frac{\varphi_P - \varphi_W}{\delta x_{WP}} \qquad (2.38)$$

By substituting equations (2.37) and (2.38) into equation (2.33), the discretised form of equation (2.32) is obtained, which is valid for the general internal node *P:*

$$\Gamma_e A_e \frac{\varphi_E - \varphi_P}{\delta x_{PE}} - \Gamma_w A_w \frac{\varphi_P - \varphi_W}{\delta x_{WP}} + \bar{S}\Delta V = 0 \qquad (2.39)$$

[2] It is second–order accurate because the neglected term in equation (2.36), i.e., the truncation error, is proportional to δx^2. This enables greater accuracy in the solution with coarser grids.

Discretised expressions of the form of equation (2.39) must be derived for each node of the computational grid in order to solve the problem. For control volumes adjacent to the domain boundaries, equation (2.39) is modified to embed boundary conditions. This results in a system of linear algebraic equations that is solved to obtain the values of the property φ at the nodes of the computational grid.

FVM FOR CONVECTION-DIFFUSION PROBLEMS

To solve problems involving the presence of a moving fluid, it is necessary to consider both the effects of transport and diffusion. Let us consider the steady-state convection-diffusion equation for the general quantity φ, derived from equation (2.27) by deleting the transient term:

$$div(\rho\varphi\boldsymbol{u}) = div(\Gamma\, grad\varphi) + S_{\varphi} \tag{2.40}$$

Simultaneously, due to the presence of a velocity field, the continuity equation must also be upheld:

$$div(\rho\boldsymbol{u}) = 0 \tag{2.41}$$

To simplify the analysis, the 1D scenario in a steady-state condition without generation is here considered. It is assumed that the velocity field is known (some methods for solving the velocity field are described in Section A.3).

Equations (2.40) and (2.41) are modified as follows:

$$\frac{d}{dx}(\rho\varphi\boldsymbol{u}) = \frac{d}{dx}\left(\Gamma\frac{d\varphi}{dx}\right) \tag{2.42}$$

$$\frac{d(\rho\boldsymbol{u})}{dx} = 0 \tag{2.43}$$

Let us now focus on the control volume in Figure 2.7, with particular attention to the general internal node *P*.

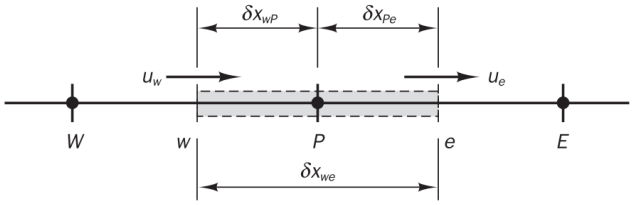

Figure 2.7. A control volume around node P [106].

The integration of equation (2.42) over the control volume yields the following expression:

$$(\rho u A\varphi)_e - (\rho u A\varphi)_w = \left(\Gamma A \frac{d\varphi}{dx}\right)_e - \left(\Gamma A \frac{d\varphi}{dx}\right)_w \tag{2.44}$$

Integration of the mass conservation equation (2.43) yields the following:

$$(\rho u A)_e - (\rho u A)_w = 0 \tag{2.45}$$

To derive the discretised equations, it is necessary to approximate the terms within equation (2.44). In this instance, not only the gradient but also the value of φ itself needs to be evaluated at the interface. The derivatives at the interfaces *(e, w)* can still be approximated according to equations (2.37) and (2.38), respectively.

Let us introduce the two terms:

$$F = \rho u A; \quad D = \frac{\Gamma A}{\delta x} \tag{2.46}$$

and thus

$$F_e = (\rho u A)_e \quad F_w = (\rho u A)_w \tag{2.47}$$

$$D_e = \frac{\Gamma_e A_e}{\delta x_{PE}} \quad D_w = \frac{\Gamma_w A_w}{\delta x_{WP}} \tag{2.48}$$

Hence, equations (2.44) and (2.45) can be rewritten as:

$$F_e\varphi_e - F_w\varphi_w = D_e(\varphi_E - \varphi_P) - D_w(\varphi_P - \varphi_W) \tag{2.49}$$

$$F_e - F_w = 0 \tag{2.50}$$

The values of φ_e and φ_w still need to be evaluated, and there are several possibilities to consider: (i) central differencing scheme, (ii) constant upwinding, and (iii) linear upwinding.

THE CENTRAL DIFFERENCING SCHEME

In the central differencing scheme, φ values at the control volume faces are computed using linear interpolation of nodal values:

$$\varphi_e = (\varphi_E + \varphi_P)/2 \tag{2.51}$$

$$\varphi_w = (\varphi_W + \varphi_P)/2 \tag{2.52}$$

The substitution of the above relationships into equation (2.49) leads to the following expression:

$$F_e\left(\frac{\varphi_E+\varphi_P}{2}\right)-F_w\left(\frac{\varphi_W+\varphi_P}{2}\right)=D_e(\varphi_E-\varphi_P)-D_w(\varphi_P-\varphi_W) \qquad (2.53)$$

Rearranging equation (2.53) and also considering the continuity equation (2.50), we obtain the discretised expression (according to the central differencing scheme) of the convection-diffusion equation for the general internal node P:

$$a_P\varphi_P=a_E\varphi_E+a_W\varphi_W \qquad (2.54)$$

where $a_P=a_E+a_W$, $a_E=D_e-\frac{F_e}{2}$, $a_W=D_w+\frac{F_w}{2}$.

By deriving expressions similar to (2.54) for all nodes, a system of linear algebraic equations is obtained, which, when solved, yields the distribution of the property φ inside the computational domain.

PROPERTIES OF DISCRETISATION SCHEMES

The central differencing scheme, which was used in the previous section for the discretisation of convective terms, exhibits stability issues when the convective term becomes more significant compared to the diffusive term. To understand the reasons behind this, it is necessary to introduce the properties that discretisation schemes must possess for the numerically results obtained from solving the approximate equations to accurately describe physical reality. The most important properties are: (i) conservativeness; (ii) boundedness; (iii) transportiveness.

i. Conservativeness

A numerical scheme must be *conservative*. The integration of the convection-diffusion equation over a finite number of control volumes leads to a set of discretised equations where the fluxes of the property φ through the control volume faces appear. To ensure the conservation of φ throughout the solution domain, the flux of φ leaving the control volume through a face must be equal to the flux entering the adjacent volume through the same face. Therefore, the flux through a common face must be consistently expressed in the same manner across adjacent elements.

ii. Boundedness

A numerical scheme must be *bounded*. To ensure *boundedness,* it is desirable for the discretisation scheme to produce coefficients in compliance with the Scarborough criterion[106], [117]:

$$\frac{|a_P|}{\sum|a_{nb}|}\begin{cases}\geq 1 & at\ all\ nodes\\ > 1 & at\ one\ node\ at\ least\end{cases} \qquad (2.55)$$

This criterion represents a sufficient condition for a convergent iterative metho.d, not a necessary one. There are instances where convergence can still be achieved despite violating the criterion [117]

Here a_P is the coefficient of the central node P and the summation in the denominator is taken over all the neighbouring nodes *(nb)*. If the condition expressed by equation (2.55) is verified, then the resulting matrix of coefficients is said to be *diagonally dominant*. From a physical perspective, this implies that, for example, in a steady-state conduction problem with no sources and boundary temperatures of 500°C and 200°C, all internal temperature values must be less than 500°C and greater than 200°C. In this sense, the problem is bounded: it has an upper and lower limit.

Another fundamental requirement for *boundedness* is that the coefficients of the discretised equations must all have the same sign (usually all positive). Physically, this means that an increase in the variable φ at one node results in an increase in nearby nodes. If the discretisation scheme does not satisfy the boundedness condition, it is possible that the solution may contain small oscillations or may not converge at all.

iii. Transportiveness

A numerical scheme should be capable of properly handling transport and taking into account the actual direction from which the flow originates. This property can be illustrated by considering the effect of two nearby sources, located at nodes *W* and *E*, on a generic node *P* (Figure 2.8).

To accomplish this, we introduce the *Peclet number*, which represents a measure of the relative strength of convection and diffusion:

$$Pe = \frac{F}{D} = \frac{\rho u \delta x}{\Gamma} \qquad (2.56)$$

where δx is the characteristic length (cell width).

The contour lines in Figure 2.8 represent the contours of constant φ in the cases of pure diffusion (Figure 2.8a) and increasing convection (Figure 2.8b). In the first case ($Pe \to 0$, pure diffusion), points *W* and *E* influence point *P* in the same way; conversely, in the case of a non-negligible convective contribution (increasing Pe), the influence of the upstream point becomes more pronounced. In this case, it is therefore crucial for the numerical scheme to consider the direction of the flow.

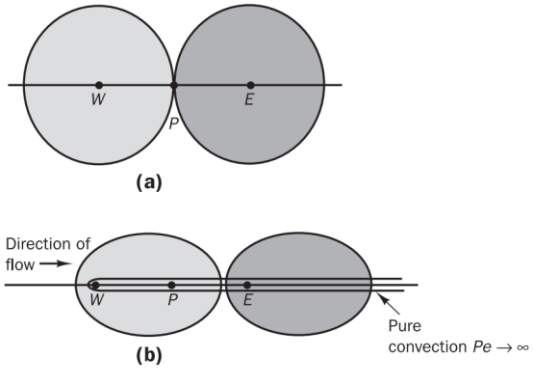

Figure 2.8. Distribution of φ in the vicinity of two sources at different Peclet numbers: (a) pure diffusion, $Pe \to 0$; (b) diffusion and convection [106].

In light of the considerations just made, it is possible to assess the applicability of the central differencing scheme to convection-diffusion problems.

- *Conservativeness:* the scheme is conservative because it employs consistent expressions to evaluate convective and diffusive fluxes at the control volume faces.
- *Boundedness:* taking into consideration the discretised equation (2.54), the scheme is bounded if a_E is positive and hence:

$$\frac{F_e}{D_e} = Pe_e < 2 \qquad (2.57)$$

  This is why the method encounters stability issues when convection dominates over diffusion: *Pe* increases and exceeds the limit just identified. To accommodate higher inlet velocities, it is necessary to refine the computational grid so as to satisfy the condition expressed by equation (2.57).
- *Trasportiveness:* the scheme does not possess the transportiveness property because it does not account for the flow direction. The fluxes through the faces are computed as the average of values upstream and downstream of the face itself.

CONSTANT UPWINDING

One of the main limitations of the central differencing scheme is its inability to identify the flow direction: the value of the property φ is always influenced by the nodes upstream and downstream. The *upwinding* method overcomes this limitation and considers the convective effects, by approximating the values of the unknown variable φ on the faces with the upstream value of φ:

$$\varphi_e = \varphi_P \qquad (2.58)$$

$$\varphi_w = \varphi_W \tag{2.59}$$

The convection-diffusion equation for the generic internal node *P*, discretised using the *upwinding* scheme, is presented below:

$$a_P\varphi_P = a_E\varphi_E + a_W\varphi_W \tag{2.60}$$

where $a_p = a_W + a_E$, $a_E = D_e$, $a_W = D_w + F_w$.

The *upwinding* method is *conservative*, possesses the *transportiveness* property (as it accounts for the flow direction) and *bounded* (the coefficients of the discretised equation are always positive, thus satisfying the condition expressed by equation (2.57)). However, it is first-order accurate and has the drawback of introducing artificial diffusion (*false diffusion*) that tends to dampen the gradients in the solution.

LINEAR UPWINDING

Linear upwinding is a second-order accurate discretisation scheme that addresses the issues of artificial diffusion introduced by constant upwinding. It takes into account the Peclet number for evaluating the property φ on the control volume faces.

A.3 Pressure-velocity coupling: SIMPLE, PISO and PIMPLE algorithms

In the preceding section, the process of discretising and solving the convection-diffusion equation for a general property φ, given the velocity field, was demonstrated. However, in general, this velocity field is not initially known but emerges as part of the overall solution along with other variables. To obtain the velocity field of a fluid system, the continuity and momentum conservation equations must be solved. However, solving these equations is challenging due to: (i) their strong coupling (each velocity component appears in each equation); (ii) the absence of an explicit equation to determine the pressure; (iii) the presence of nonlinear terms in the momentum conservation equation. For incompressible flows, the calculation is further complicated by the strong coupling between pressure and velocity (if the correct pressure field is applied in the conservation of momentum, the resulting velocity field must satisfy mass conservation) and the fact that pressure does not appear as a primary variable in the equations of momentum conservation nor continuity. The issues associated with nonlinearity in the system of equations and the pressure-velocity coupling can be addressed by adopting iterative solution strategies. Among the most used solvers are the so-called *pressure-based* algorithms, which involve determining

the velocity field by solving the momentum conservation equation and calculating the pressure field by solving a pressure-correction equation (obtained by manipulating the equations of mass and momentum conservation and taking the form of a Poisson equation). *Pressure-based* algorithms can be categorised as *segregated* and *coupled;* with the former, the governing equations are solved separately and sequentially, while with the latter, they are solved simultaneously. In OpenFOAM, the segregated solvers SIMPLE, PISO, and PIMPLE are implemented, and these are described in more detail in the following sections.

SIMPLE ALGORITHM

The SIMPLE algorithm (Semi-Implicit Method for Pressure-Linked Equations), developed by Patankar and Spalding in 1972 [118], is a steady-state solver for both compressible and incompressible flows. Over the years, many variations of this algorithm have been proposed, making it one of the most extensively studied algorithms in computational fluid dynamics.

The algorithm, whose flowchart is depicted in Figure 3.1, involves an iterative sequence of steps ($i = 1, 2, \dots, i_{end}$) until convergence is reached. It starts by constructing a matrix equation for energy, which is under-relaxed (a method used to improve the convergence of the solution, by limiting the amount of variation of a variable during a solution step) by a factor α_T. This equation is solved for temperature T, which is then used to update the density $\rho(T, p)$ according to an equation of state. A matrix equation denoted as $\mathbf{A} \cdot \mathbf{u} - \mathbf{b}$ (momentum matrix) is then built using all terms from the momentum conservation equation except ∇p; this matrix equation is under-relaxed by a factor α_u before being equated to $-\nabla p$ and solved for the velocity vector $\mathbf{u}$ (momentum predictor). Starting from the matrix equation $\mathbf{A} \cdot \mathbf{u} - \mathbf{b}$, the terms $\boldsymbol{A}\mathbf{u}$ and $\mathbf{H}(\mathbf{u})$ are determined, where $\boldsymbol{A}$ is a diagonal matrix (see Figure 3.2).

These derived terms are employed to formulate the pressure equation and calculate p. The new pressure is then used to correct the mass flux ϕ_{f} to ensure with greater accuracy the adherence to the mass conservation equation (flux corrector). Finally, it is under-relaxed by a factor α_p before correcting the velocity value (momentum corrector).

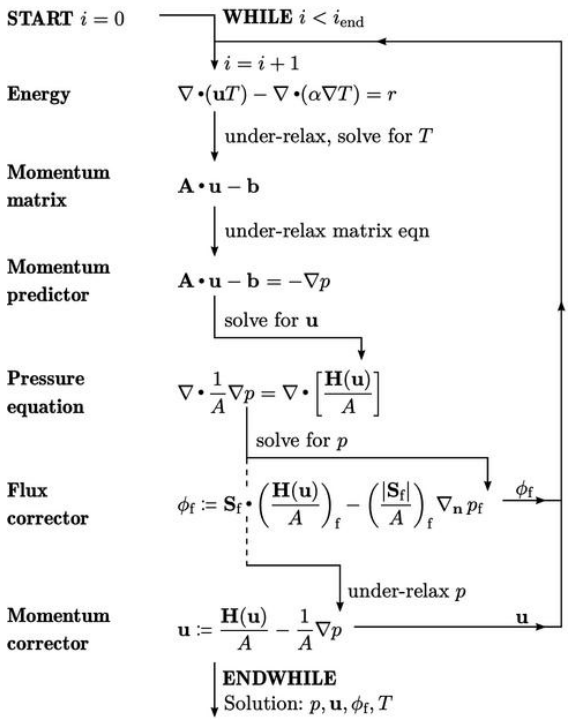

Figure 3.1. Implementation of the SIMPLE algorithm in OpenFOAM [112].

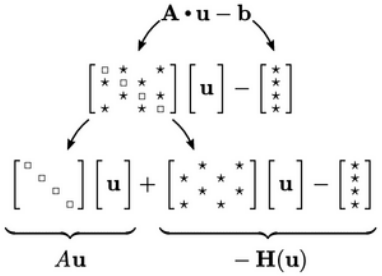

Figure 3.2. Splitting of the starting matrix equation $\mathbf{A} \cdot \mathbf{u} - \mathbf{b}$ [112].

PISO ALGORITHM

The PISO algorithm (Pressure Implicit with Splitting of Operators), introduced by Issa in 1986 [119], is a non-iterative method for solving the coupled equations arising from the implicit discretisation of the time-varying fluid motion equations. It can be seen as a transient version of SIMPLE, with the significant modification that the momentum corrector is executed more than once for each time step (PISO loop).

The equations are solved over successive time intervals Δt between an initial time instant t_{start} and a final time instant t_{end} (Figure 3.3). The time step must be relatively small to maintain sufficient accuracy in describing transient phenomena, a condition that is expressed in terms of the maximum allowable Courant number ($Co < 1$).

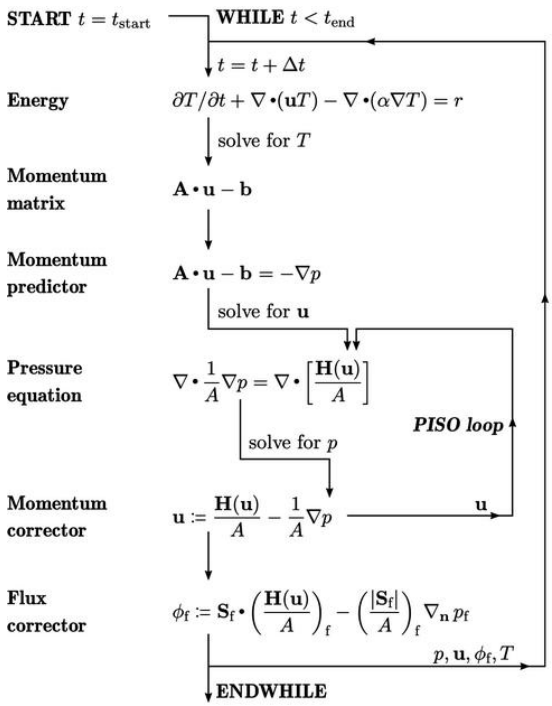

Figure 3.3. Implementation of the PISO algorithm in OpenFOAM [112].

PIMPLE ALGORITHM

The algorithms for pressure-velocity coupling previously presented can be combined into an algorithm known as PIMPLE. It blends the controls of both PISO and SIMPLE (hence the merged acronym), particularly the iterative cycles and under-relaxation. It can be viewed as the application of SIMPLE at each time step, iterating until convergence or a maximum number of iterations is reached. The advantage of PIMPLE over PISO is its increased stability, even with $Co > 1$. Figure 3.4 illustrates the flowchart of the PIMPLE solver, as implemented in OpenFOAM [112].

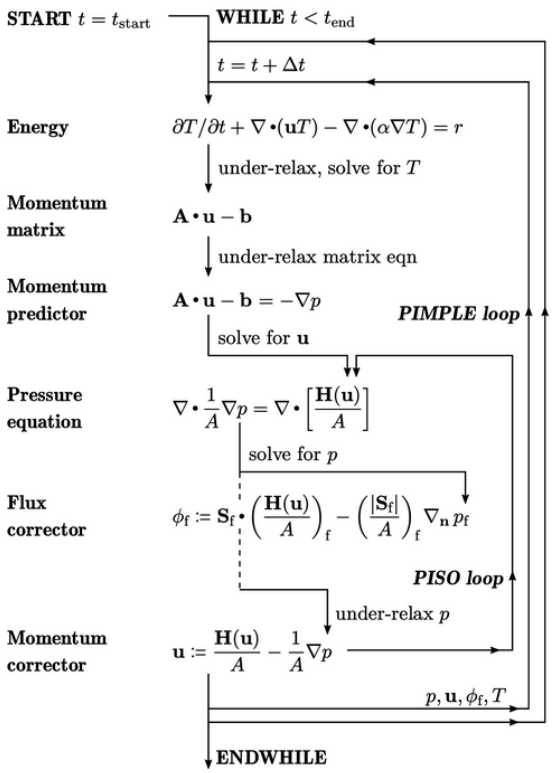

Figure 3.4. Implementation of the PIMPLE algorithm in OpenFOAM [112].

References

[1] M. Costa, M. Dell'Isola, e N. Massarotti, «Temperature and residence time of the combustion products in a waste-to-energy plant», *Fuel*, vol. 102, pp. 92–105, dic. 2012, doi: 10.1016/j.fuel.2012.06.043.

[2] European Commission, «REPORT FROM THE COMMISSION TO THE EUROPEAN PARLIAMENT, THE COUNCIL, THE EUROPEAN ECONOMIC AND SOCIAL COMMITTEE AND THE COMMITTEE OF THE REGIONS on the Thematic Strategy on the Prevention and Recycling of Waste SEC(2011)», 2011. [Online]. Disponibile su: https://eur-lex.europa.eu/legal-content/EN/TXT/HTML/?uri=CELEX:52011DC0013

[3] EUROPEAN COMMISSION, «The Role of Waste-to-Energy in the Circular Economy», presentato al COM(2017) final, Brussels, gen. 2017. [Online]. Disponibile su: https://eur-lex.europa.eu/LexUriServ/LexUriServ.do?uri=COM:2017:0034:FIN:EN:PDF

[4] J. Vehlow, «Reduction of dioxin emissions from thermal waste treatment plants: a brief survey», *Rev Environ Sci Biotechnol*, vol. 11, fasc. 4, pp. 393–405, dic. 2012, doi: 10.1007/s11157-012-9296-5.

[5] M. J. Murer *et al.*, «High efficient waste-to-energy in Amsterdam: getting ready for the next steps», *Waste Manag Res*, vol. 29, fasc. 10_suppl, pp. S20–S29, ott. 2011, doi: 10.1177/0734242X11413334.

[6] United Nations, «Paris Agreement», Paris, dic. 2015. [Online]. Disponibile su: https://unfccc.int/sites/default/files/english_paris_agreement.pdf.

[7] M. Kabir, A. Chowdhury, e M. Rasul, «Pyrolysis of Municipal Green Waste: A Modelling, Simulation and Experimental Analysis», *Energies*, vol. 8, fasc. 8, pp. 7522–7541, lug. 2015, doi: 10.3390/en8087522.

[8] A. Zhou, H. Xu, Y. Tu, F. Zhao, Z. Zheng, e W. Yang, «Numerical investigation of the effect of air supply and oxygen enrichment on the biomass combustion in the grate boiler», *Applied Thermal Engineering*, vol. 156, pp. 550–561, giu. 2019, doi: 10.1016/j.applthermaleng.2019.04.053.

[9] M. Costa, N. Massarotti, A. Mauro, F. Arpino, e V. Rocco, «CFD modelling of a RDF incineration plant», *Applied Thermal Engineering*, vol. 101, pp. 710–719, mag. 2016, doi: 10.1016/j.applthermaleng.2016.01.073.

[10] C. Montejo, C. Costa, P. Ramos, e M. D. C. Márquez, «Analysis and comparison of municipal solid waste and reject fraction as fuels for incineration plants», *Applied Thermal Engineering*, vol. 31, fasc. 13, pp. 2135–2140, set. 2011, doi: 10.1016/j.applthermaleng.2011.03.041.

[11] F. Arpino *et al.*, «A novel approach for the numerical analysis of waste-to-energy plants», *J. Phys.: Conf. Ser.*, vol. 1599, fasc. 1, p. 012025, ago. 2020, doi: 10.1088/1742-6596/1599/1/012025.

[12] N. Couto *et al.*, «Numerical and experimental analysis of municipal solid wastes gasification process», *Applied Thermal Engineering*, vol. 78, pp. 185–195, mar. 2015, doi: 10.1016/j.applthermaleng.2014.12.036.
[13] S. Jarungthammachote e A. Dutta, «Thermodynamic equilibrium model and second law analysis of a downdraft waste gasifier», *Energy*, vol. 32, fasc. 9, pp. 1660–1669, set. 2007, doi: 10.1016/j.energy.2007.01.010.
[14] S. Kumar, S. Kumar, e J. K. Prajapati, «Hydrogen production by partial oxidation of methane: Modeling and simulation», *International Journal of Hydrogen Energy*, vol. 34, fasc. 16, pp. 6655–6668, ago. 2009, doi: 10.1016/j.ijhydene.2009.06.043.
[15] N. F. Dummer *et al.*, «Methane Oxidation to Methanol», *Chem. Rev.*, vol. 123, fasc. 9, pp. 6359–6411, mag. 2023, doi: 10.1021/acs.chemrev.2c00439.
[16] H. K. Versteeg e W. Malalasekera, *An introduction to computational fluid dynamics: the finite volume method*, 2nd ed. Harlow, England ; New York: Pearson Education Ltd, 2007.
[17] P. Bradshaw, *An introduction to turbulence and its measurement*, Facsim. ed. in Pergamon international library of science, technology, engineering and social studies. Elkins Park (Pa.): Franklin book, 1993.
[18] D. C. Wilcox, *Turbulence modeling for CFD*. La Cãnada, CA: DCW Industries, Inc, 1993.
[19] *Fondamenti di trasmissione del calore. 1*, 2. ed. Napoli: Liguori, 1991.
[20] A. Bejan e A. D. Kraus, *Heat transfer handbook*. New York: J. Wiley, 2003.
[21] F. Moukalled, L. Mangani, e M. Darwish, *The Finite Volume Method in Computational Fluid Dynamics: An Advanced Introduction with OpenFOAM® and Matlab*, vol. 113. in Fluid Mechanics and Its Applications, vol. 113. Cham: Springer International Publishing, 2016. doi: 10.1007/978-3-319-16874-6.
[22] H. G. Weller, G. Tabor, H. Jasak, e C. Fureby, «A tensorial approach to computational continuum mechanics using object-oriented techniques», *Computers in Physics*, vol. 12, fasc. 6, pp. 620–631, nov. 1998, doi: 10.1063/1.168744.
[23] M. L. de Souza-Santos, *Solid fuels combustion and gasification: modeling, simulation, and equipment operations*, 2nd ed. in Mechanical engineering. Boca Raton, FL: CRC Press, Taylor & Francis, 2010.
[24] D. C. Toncu, G. Toncu, e S. Soleimani, «On methane pyrolysis special applications», *IOP Conf. Ser.: Mater. Sci. Eng.*, vol. 95, p. 012026, nov. 2015, doi: 10.1088/1757-899X/95/1/012026.
[25] Luigi Acampora e Francesco Saverio Marra, «Investigation by thermodynamic properties of methane combustion mechanisms under harmonic oscillations in perfectly stirred reactor», *Chemical Engineering Transactions*, vol. 57, pp. 1459–1464, mag. 2017, doi: 10.3303/CET1757244.
[26] *Combustion of Liquid Fuel Sprays*. Elsevier, 1990. doi: 10.1016/C2013-0-00958-9.
[27] Z. Lian, J. Zhang, F. Zhao, e W. Yu, «Optimization of methane simplified chemical kinetic mechanism based on uncertainty quantitation analysis by sparse polynomial chaos expansions», *Fuel*, vol. 339, p. 127393, mag. 2023, doi: 10.1016/j.fuel.2023.127393.

[28] N. A. Slavinskaya e O. Haidn, «Reduced Chemical Mechanism for Methane Combustion», presentato al 2nd European Conference for Aerospace Sciences (eucass), 2007.
[29] B. A. Putra e I. S. Ertesvåg, «Investigations of the extended Eddy Dissipation Concept formulation for weakly turbulent and slow chemistry flames», *Fuel*, vol. 352, p. 129013, nov. 2023, doi: 10.1016/j.fuel.2023.129013.
[30] F. Arpino, G. Cortellessa, G. Grossi, e H. Nagano, «A Eulerian-Lagrangian approach for the non-isothermal and transient CFD analysis of the aerosol airborne dispersion in a car cabin», *Building and Environment*, vol. 209, p. 108648, feb. 2022, doi: 10.1016/j.buildenv.2021.108648.
[31] G. Cortellessa *et al.*, «Close proximity risk assessment for SARS-CoV-2 infection», *Science of The Total Environment*, vol. 794, p. 148749, nov. 2021, doi: 10.1016/j.scitotenv.2021.148749.
[32] B. Gulsacan, N. Tokgoz, E. S. Karakas, M. Aureli, e C. A. Evrensel, «Effect of orifice thickness-to-diameter ratio on turbulent orifice flow: An experimental and numerical investigation», *International Communications in Heat and Mass Transfer*, vol. 151, p. 107213, feb. 2024, doi: 10.1016/j.icheatmasstransfer.2023.107213.
[33] A. Golijanek-Jędrzejczyk, A. Mrowiec, S. Kleszcz, R. Hanus, M. Zych, e M. Jaszczur, «A numerical and experimental analysis of multi-hole orifice in turbulent flow», *Measurement*, vol. 193, p. 110910, apr. 2022, doi: 10.1016/j.measurement.2022.110910.
[34] IEA (2023), «CO2 Emissions in 2022». IEA. [Online]. Disponibile su: https://www.iea.org/reports/co2-emissions-in-2022
[35] M. J. Reader-Harris e J. A. Sattary, «The orifice plate discharge coefficient equation», *Flow Measurement and Instrumentation*, vol. 1, fasc. 2, pp. 67–76, gen. 1990, doi: 10.1016/0955-5986(90)90031-2.
[36] M. Reader-Harris, «Orifice Expansibility Factor», in *Orifice Plates and Venturi Tubes*, in Experimental Fluid Mechanics. , Cham: Springer International Publishing, 2015, pp. 187–201. doi: 10.1007/978-3-319-16880-7_6.
[37] T. T. YEH, *LASER DOPPLER VELOCIMETER STUDIES OF THE PIPEFLOW PRODUCED BY A GENERIC HEADER (CLASSIC REPRINT)*. S.l.: FORGOTTEN BOOKS, 2018.
[38] K. Gersten, «Fully Developed Turbulent Pipe Flow», in *Fluid Mechanics of Flow Metering*, W. Merzkirch, A c. di, Berlin, Heidelberg: Springer Berlin Heidelberg, 2005, pp. 1–22. doi: 10.1007/3-540-26725-5_1.
[39] F. R. Menter, M. Kuntz, e R. Langtry, «Ten Years of Industrial Experience with the SST Turbulence Model», 2003.
[40] F. R. Menter, «Two-equation eddy-viscosity turbulence models for engineering applications», *AIAA Journal*, vol. 32, fasc. 8, pp. 1598–1605, ago. 1994, doi: 10.2514/3.12149.
[41] International Standard published, *ISO Standard 5167*. 2022, p. 42.
[42] O. Büker, P. Lau, e K. Tawackolian, «Reynolds number dependence of an orifice plate», *Flow Measurement and Instrumentation*, vol. 30, pp. 123–132, apr. 2013, doi: 10.1016/j.flowmeasinst.2013.01.009.

[43] Y. Li, «Basic routes of transmission of respiratory pathogens—A new proposal for transmission categorization based on respiratory spray, inhalation, and touch», *Indoor Air*, vol. 31, fasc. 1, pp. 3–6, gen. 2021, doi: 10.1111/ina.12786.
[44] G. Buonanno *et al.*, «Link between SARS-CoV-2 emissions and airborne concentrations: Closing the gap in understanding», *Journal of Hazardous Materials*, vol. 428, p. 128279, apr. 2022, doi: 10.1016/j.jhazmat.2022.128279.
[45] T. Greenhalgh, J. L. Jimenez, K. A. Prather, Z. Tufekci, D. Fisman, e R. Schooley, «Ten scientific reasons in support of airborne transmission of SARS-CoV-2.», *Lancet*, vol. 397, fasc. 10285, pp. 1603–1605, mag. 2021, doi: 10.1016/S0140-6736(21)00869-2.
[46] W. W. Nazaroff, «Indoor aerosol science aspects of SARS-CoV-2 transmission», *Indoor Air*, vol. 32, fasc. 1, gen. 2022, doi: 10.1111/ina.12970.
[47] A. C. D'Alicandro, N. Massarotti, e A. Mauro, «Aerosol hazards in operating rooms: A review of numerical and experimental studies», *Journal of Aerosol Science*, vol. 158, p. 105823, nov. 2021, doi: 10.1016/j.jaerosci.2021.105823.
[48] M. Abuhegazy, K. Talaat, O. Anderoglu, e S. V. Poroseva, «Numerical investigation of aerosol transport in a classroom with relevance to COVID-19», *Physics of Fluids*, vol. 32, fasc. 10, p. 103311, ott. 2020, doi: 10.1063/5.0029118.
[49] G. K. Rencken, E. K. Rutherford, N. Ghanta, J. Kongoletos, e L. Glicksman, «Patterns of SARS-CoV-2 aerosol spread in typical classrooms», *Building and Environment*, vol. 204, p. 108167, ott. 2021, doi: 10.1016/j.buildenv.2021.108167.
[50] W. Li *et al.*, «Effects of ceiling fans on airborne transmission in an air-conditioned space», *Building and Environment*, vol. 198, p. 107887, lug. 2021, doi: 10.1016/j.buildenv.2021.107887.
[51] Y. Wang, F.-Y. Zhao, J. Kuckelkorn, D. Liu, J. Liu, e J.-L. Zhang, «Classroom energy efficiency and air environment with displacement natural ventilation in a passive public school building», *Energy and Buildings*, vol. 70, pp. 258–270, feb. 2014, doi: 10.1016/j.enbuild.2013.11.071.
[52] N. Massarotti, A. Mauro, S. Mohamed, A. J. Nowak, e D. Sainas, «Fluid dynamic and thermal comfort analysis in an actual operating room with unidirectional airflow system», *Build. Simul.*, vol. 14, fasc. 4, pp. 1127–1146, ago. 2021, doi: 10.1007/s12273-020-0713-3.
[53] ISO, «ISO 7730 - Ergonomics of the thermal environment — Analytical determination and interpretation of thermal comfort using calculation of the PMV and PPD indices and local thermal comfort criteria». 2005.
[54] C. T. Crowe, J. D. Schwarzkopf, M. Sommerfeld, e Y. Tsuji, *Multiphase Flows with Droplets and Particles*, 0 ed. CRC Press, 2011. doi: 10.1201/b11103.
[55] M. R. R. S. van Beest *et al.*, «Influence of indoor airflow on particle spread of a single breath and cough in enclosures: Does opening a window really 'help'?», *Atmospheric Pollution Research*, vol. 13, fasc. 7, p. 101473, lug. 2022, doi: 10.1016/j.apr.2022.101473.
[56] C. Kleinstreuer, *Two-phase flow: theory and applications*. New York: Taylor & Francis, 2003.
[57] C. Kleinstreuer e Y. Feng, «Computational Analysis of Non-Spherical Particle Transport and Deposition in Shear Flow With Application to Lung Aerosol

Dynamics—A Review», *Journal of Biomechanical Engineering*, vol. 135, fasc. 2, p. 021008, feb. 2013, doi: 10.1115/1.4023236.

[58] R. M. McCombs e W. E. Rawls, «Density Gradient Centrifugation of Rubella Virus», *J Virol*, vol. 2, fasc. 5, pp. 409–414, mag. 1968, doi: 10.1128/jvi.2.5.409-414.1968.

[59] M. Pattison, D. J. Alexander, e J. W. Harkness, «Purification and preliminary characterisation of a pathogenic strain of infectious bursal disease virus», *Avian Pathology*, vol. 4, fasc. 3, pp. 175–187, lug. 1975, doi: 10.1080/03079457509353864.

[60] A. E. Ritchie, D. R. Deshmukh, C. T. Larsen, e B. S. Pomeroy, «Electron Microscopy of Coronavirus-Like Particles Characteristic of Turkey Bluecomb Disease», *Avian Diseases*, vol. 17, fasc. 3, p. 546, lug. 1973, doi: 10.2307/1589153.

[61] G. R. Johnson *et al.*, «Modality of human expired aerosol size distributions», *Journal of Aerosol Science*, vol. 42, fasc. 12, pp. 839–851, dic. 2011, doi: 10.1016/j.jaerosci.2011.07.009.

[62] L. Morawska *et al.*, «Size distribution and sites of origin of droplets expelled from the human respiratory tract during expiratory activities», *Journal of Aerosol Science*, vol. 40, fasc. 3, pp. 256–269, mar. 2009, doi: 10.1016/j.jaerosci.2008.11.002.

[63] K. P. Fennelly, «Particle sizes of infectious aerosols: implications for infection control», *The Lancet Respiratory Medicine*, vol. 8, fasc. 9, pp. 914–924, set. 2020, doi: 10.1016/S2213-2600(20)30323-4.

[64] S. L. Bixler *et al.*, «Aerosol Exposure of Cynomolgus Macaques to SARS-CoV-2 Results in More Severe Pathology than Existing Models», *bioRxiv*, p. 2021.04.27.441510, gen. 2021, doi: 10.1101/2021.04.27.441510.

[65] S. Balachandar, S. Zaleski, A. Soldati, G. Ahmadi, e L. Bourouiba, «Host-to-host airborne transmission as a multiphase flow problem for science-based social distance guidelines», *International Journal of Multiphase Flow*, vol. 132, p. 103439, nov. 2020, doi: 10.1016/j.ijmultiphaseflow.2020.103439.

[66] X. Xie, Y. Li, A. T. Y. Chwang, P. L. Ho, e W. H. Seto, «How far droplets can move in indoor environments ? revisiting the Wells evaporation?falling curve», *Indoor Air*, vol. 17, fasc. 3, pp. 211–225, giu. 2007, doi: 10.1111/j.1600-0668.2007.00469.x.

[67] K. Ohmi e H.-Y. Li, «Particle-tracking velocimetry with new algorithms», *Meas. Sci. Technol.*, vol. 11, fasc. 6, pp. 603–616, giu. 2000, doi: 10.1088/0957-0233/11/6/303.

[68] A. Saber, T. S. Lundström, e J. G. I. Hellström, «Turbulent Modulation in Particulate Flow: A Review of Critical Variables», *ENG*, vol. 07, fasc. 10, pp. 597–609, 2015, doi: 10.4236/eng.2015.710054.

[69] J. C. Weil, R. I. Sykes, e A. Venkatram, «Evaluating Air-Quality Models: Review and Outlook», *Journal of Applied Meteorology (1988-2005)*, vol. 31, fasc. 10, pp. 1121–1145, 1992.

[70] C. Poelma, J. Westerweel, e G. Ooms, «Particle–fluid interactions in grid-generated turbulence», *J. Fluid Mech.*, vol. 589, pp. 315–351, ott. 2007, doi: 10.1017/S0022112007007793.

[71] D. Kim, M. Kim, E. Saredi, F. Scarano, e K. C. Kim, «Robotic PTV study of the flow around automotive side-view mirror models», *Experimental Thermal and Fluid Science*, vol. 119, p. 110202, nov. 2020, doi: 10.1016/j.expthermflusci.2020.110202.

[72] M. Elhimer, O. Praud, M. Marchal, S. Cazin, e R. Bazile, «Simultaneous PIV/PTV velocimetry technique in a turbulent particle-laden flow», *J Vis*, vol. 20, fasc. 2, pp. 289–304, mag. 2017, doi: 10.1007/s12650-016-0397-z.

[73] Q. Chen, «Ventilation performance prediction for buildings: A method overview and recent applications», *Building and Environment*, vol. 44, fasc. 4, pp. 848–858, apr. 2009, doi: 10.1016/j.buildenv.2008.05.025.

[74] D. E. Faleiros, M. Tuinstra, A. Sciacchitano, e F. Scarano, «Generation and control of helium-filled soap bubbles for PIV», *Exp Fluids*, vol. 60, fasc. 3, p. 40, mar. 2019, doi: 10.1007/s00348-019-2687-4.

[75] B. Wieneke, «Volume self-calibration for 3D particle image velocimetry», *Exp Fluids*, vol. 45, fasc. 4, pp. 549–556, ott. 2008, doi: 10.1007/s00348-008-0521-5.

[76] D. Schanz, S. Gesemann, e A. Schröder, «Shake-The-Box: Lagrangian particle tracking at high particle image densities», *Exp Fluids*, vol. 57, fasc. 5, p. 70, mag. 2016, doi: 10.1007/s00348-016-2157-1.

[77] N. Agüera, G. Cafiero, T. Astarita, e S. Discetti, «Ensemble 3D PTV for high resolution turbulent statistics», *Meas. Sci. Technol.*, vol. 27, fasc. 12, p. 124011, dic. 2016, doi: 10.1088/0957-0233/27/12/124011.

[78] F. R. Menter, «Two-equation eddy-viscosity turbulence models for engineering applications», *AIAA Journal*, vol. 32, fasc. 8, pp. 1598–1605, ago. 1994, doi: 10.2514/3.12149.

[79] K. Hanjalić, Y. Nagano, e M. J. Tummers, A c. di, *Turbulence, heat and mass transfer 4: proceedings of the Fourth International Symposium on Turbulence, Heat and Mass Transfer, Antalya, Turkey, 12 - 17 October, 2003*. New York, NY: Begell House, 2003.

[80] R. Kotapati-Apparao, J. Forsythe, e K. Squires, «Computation of the Flow Over a Maneuvering Spheroid», in *41st Aerospace Sciences Meeting and Exhibit*, Reno, Nevada: American Institute of Aeronautics and Astronautics, gen. 2003. doi: 10.2514/6.2003-269.

[81] K. Squires, J. Forsythe, e R. Kotapati-Apparao, «Prediction of the Flow over an Airfoil at Maximum Lift», in *42nd AIAA Aerospace Sciences Meeting and Exhibit*, Reno, Nevada: American Institute of Aeronautics and Astronautics, gen. 2004. doi: 10.2514/6.2004-259.

[82] C. J. Keylock, R. J. Hardy, D. R. Parsons, R. I. Ferguson, S. N. Lane, e K. S. Richards, «The theoretical foundations and potential for large-eddy simulation (LES) in fluvial geomorphic and sedimentological research», *Earth-Science Reviews*, vol. 71, fasc. 3–4, pp. 271–304, ago. 2005, doi: 10.1016/j.earscirev.2005.03.001.

[83] D. E. Faleiros, M. Tuinstra, A. Sciacchitano, e F. Scarano, «Generation and control of helium-filled soap bubbles for PIV», *Exp Fluids*, vol. 60, fasc. 3, p. 40, mar. 2019, doi: 10.1007/s00348-019-2687-4.

[84] L. Morawska e J. Cao, «Airborne transmission of SARS-CoV-2: The world should face the reality», *Environment International*, vol. 139, p. 105730, giu. 2020, doi: 10.1016/j.envint.2020.105730.
[85] S. Balachandar, S. Zaleski, A. Soldati, G. Ahmadi, e L. Bourouiba, «Host-to-host airborne transmission as a multiphase flow problem for science-based social distance guidelines», *International Journal of Multiphase Flow*, vol. 132, p. 103439, nov. 2020, doi: 10.1016/j.ijmultiphaseflow.2020.103439.
[86] W. Chen, N. Zhang, J. Wei, H.-L. Yen, e Y. Li, «Short-range airborne route dominates exposure of respiratory infection during close contact», *Building and Environment*, vol. 176, p. 106859, giu. 2020, doi: 10.1016/j.buildenv.2020.106859.
[87] O. Gallo, L. G. Locatello, A. Mazzoni, L. Novelli, e F. Annunziato, «The central role of the nasal microenvironment in the transmission, modulation, and clinical progression of SARS-CoV-2 infection», *Mucosal Immunology*, vol. 14, fasc. 2, pp. 305–316, mar. 2021, doi: 10.1038/s41385-020-00359-2.
[88] Z. Ai, K. Hashimoto, e A. K. Melikov, «Influence of pulmonary ventilation rate and breathing cycle period on the risk of cross-infection», *Indoor Air*, vol. 29, fasc. 6, pp. 993–1004, nov. 2019, doi: 10.1111/ina.12589.
[89] Z. T. Ai e A. K. Melikov, «Airborne spread of expiratory droplet nuclei between the occupants of indoor environments: A review», *Indoor Air*, vol. 28, fasc. 4, pp. 500–524, lug. 2018, doi: 10.1111/ina.12465.
[90] M. Raffel, C. E. Willert, S. T. Wereley, e J. Kompenhans, *Particle Image Velocimetry: A Practical Guide*. Berlin, Heidelberg: Springer Berlin Heidelberg, 2007. doi: 10.1007/978-3-540-72308-0.
[91] G. R. Johnson *et al.*, «Modality of human expired aerosol size distributions», *Journal of Aerosol Science*, vol. 42, fasc. 12, pp. 839–851, dic. 2011, doi: 10.1016/j.jaerosci.2011.07.009.
[92] L. Morawska *et al.*, «Size distribution and sites of origin of droplets expelled from the human respiratory tract during expiratory activities», *Journal of Aerosol Science*, vol. 40, fasc. 3, pp. 256–269, mar. 2009, doi: 10.1016/j.jaerosci.2008.11.002.
[93] X. Xie, Y. Li, A. T. Y. Chwang, P. L. Ho, e W. H. Seto, «How far droplets can move in indoor environments ? revisiting the Wells evaporation?falling curve», *Indoor Air*, vol. 17, fasc. 3, pp. 211–225, giu. 2007, doi: 10.1111/j.1600-0668.2007.00469.x.
[94] M. Abkarian, S. Mendez, N. Xue, F. Yang, e H. A. Stone, «Speech can produce jet-like transport relevant to asymptomatic spreading of virus», *Proc. Natl. Acad. Sci. U.S.A.*, vol. 117, fasc. 41, pp. 25237–25245, ott. 2020, doi: 10.1073/pnas.2012156117.
[95] J. Fajnzylber *et al.*, «SARS-CoV-2 viral load is associated with increased disease severity and mortality», *Nat Commun*, vol. 11, fasc. 1, p. 5493, ott. 2020, doi: 10.1038/s41467-020-19057-5.
[96] Y. Pan, D. Zhang, P. Yang, L. L. M. Poon, e Q. Wang, «Viral load of SARS-CoV-2 in clinical samples», *The Lancet Infectious Diseases*, vol. 20, fasc. 4, pp. 411–412, apr. 2020, doi: 10.1016/S1473-3099(20)30113-4.

[97] R. Wölfel *et al.*, «Virological assessment of hospitalized patients with COVID-2019», *Nature*, vol. 581, fasc. 7809, pp. 465–469, mag. 2020, doi: 10.1038/s41586-020-2196-x.

[98] A. Mikszewski, L. Stabile, G. Buonanno, e L. Morawska, «THE AIRBORNE CONTAGIOUSNESS OF RESPIRATORY VIRUSES: A COMPARATIVE ANALYSIS AND IMPLICATIONS FOR MITIGATION», 29 gennaio 2021. doi: 10.1101/2021.01.26.21250580.

[99] K. P. Fennelly, «Particle sizes of infectious aerosols: implications for infection control», *The Lancet Respiratory Medicine*, vol. 8, fasc. 9, pp. 914–924, set. 2020, doi: 10.1016/S2213-2600(20)30323-4.

[100] J. Jimenez *et al.*, «What Were the Historical Reasons for the Resistance to Recognizing Airborne Transmission during the COVID-19 Pandemic?», *SSRN*, 2021.

[101] L. Morawska *et al.*, «How can airborne transmission of COVID-19 indoors be minimised?», *Environment International*, vol. 142, p. 105832, set. 2020, doi: 10.1016/j.envint.2020.105832.

[102] G. Buonanno, L. Ricolfi, L. Morawska, e L. Stabile, «Increasing ventilation reduces SARS-CoV-2 airborne transmission in schools: A retrospective cohort study in Italy's Marche region», *Frontiers in Public Health*, vol. 10, 2022, [Online]. Disponibile su: https://www.frontiersin.org/articles/10.3389/fpubh.2022.1087087

[103] F. Arpino, G. Cortellessa, A. C. D'Alicandro, G. Grossi, N. Massarotti, e A. Mauro, «Numerical Investigations of the Aerosol Airborne Dispersion Inside a University Lecture Room», *SSRN*, 2022, [Online]. Disponibile su: https://www.scopus.com/inward/record.uri?eid=2-s2.0-85144163339&partnerID=40&md5=6aa3b71e3faf257c4f838848d13d3a9e

[104] M. Abkarian, S. Mendez, N. Xue, F. Yang, e H. A. Stone, «Speech can produce jet-like transport relevant to asymptomatic spreading of virus», *Proc. Natl. Acad. Sci. U. S. A.*, vol. 117, fasc. 41, pp. 25237–25245, 2020, doi: 10.1073/pnas.2012156117.

[105] M. Abkarian, S. Mendez, N. Xue, F. Yang, e H. A. Stone, «Speech can produce jet-like transport relevant to asymptomatic spreading of virus», *Proc Natl Acad Sci USA*, vol. 117, fasc. 41, pp. 25237–25245, ott. 2020, doi: 10.1073/pnas.2012156117.

[106] H. K. Versteeg e W. Malalasekera, *An introduction to computational fluid dynamics: the finite volume method*, 2nd ed. Harlow, England ; New York: Pearson Education Ltd, 2007.

[107] J. H. Ferziger e M. Perić, *Computational methods for fluid dynamics*, 3rd, rev. ed ed. Berlin ; New York: Springer, 2002.

[108] J. Tu, G. H. Yeoh, e C. Liu, *Computational fluid dynamics: a practical approach*, Third edition. Oxford ; Cambridge, MA: Butterworth-Heinemann, 2018.

[109] Joel Guerrero, «Introduction to Computational Fluid Dynamics: Governing Equations, Turbulence Modeling Introduction and Finite Volume Discretization Basics.» 2021.

[110] Y. A. Çengel, M. A. Boles, e M. Kanoğlu, *Thermodynamics: an engineering approach*, Ninth edition. New York, NY: McGraw-Hill Education, 2019.
[111] S. B. Pope, *Turbulent Flows*, 1ª ed. Cambridge University Press, 2000. doi: 10.1017/CBO9780511840531.
[112] C. J. Greenshields e H. G. Weller, *Notes on computational fluid dynamics: general principles*. Reading, UK: CFD Direct Limited, 2022.
[113] S.J. Hulshoff, «CFD II Part 2: Computation and Modelling of Turbulence». Delft University of Technology, aprile 2105.
[114] André Bakker, «Applied computational fluid dynamics. Lecture 10 - Turbulence models». 2008. [Online]. Disponibile su: http://www.bakker.org
[115] C. D. Argyropoulos e N. C. Markatos, «Recent advances on the numerical modelling of turbulent flows», *Applied Mathematical Modelling*, vol. 39, fasc. 2, pp. 693–732, gen. 2015, doi: 10.1016/j.apm.2014.07.001.
[116] Y. A. Çengel, J. M. Cimbala, G. Cozzo, e C. Santoro, *Meccanica dei fluidi*, 3. ed. Milano: McGraw-Hill Education, 2015.
[117] S. V. Patankar, *Numerical heat transfer and fluid flow*. in Series in computational methods in mechanics and thermal sciences. Boca Raton: CRC Press, 2009.
[118] S. V. Patankar e D. B. Spalding, «A calculation procedure for heat, mass and momentum transfer in three-dimensional parabolic flows», *International Journal of Heat and Mass Transfer*, vol. 15, fasc. 10, pp. 1787–1806, ott. 1972, doi: 10.1016/0017-9310(72)90054-3.
[119] R. I. Issa, «Solution of the implicitly discretised fluid flow equations by operator-splitting», *Journal of Computational Physics*, vol. 62, fasc. 1, pp. 40–65, gen. 1986, doi: 10.1016/0021-9991(86)90099-9.

LIST OF PUBLICATIONS

JOURNAL ARTICLES

Cortellessa G., Canale C., Stabile L., Grossi G., Buonanno G. and Arpino F. (2023). Effectiveness of a portable personal air cleaner in reducing the airborne transmission of respiratory pathogens. *Building and Environment, 235,* 110222.

Arpino F., Canale C., Cortellessa G., Dell'Isola M., Ficco G., Grossi G. and Moretti L. (2024). Green hydrogen for energy storage and natural gas system decarbonization: An Italian case study. *International Journal of Hydrogen Energy, 49,* 586-600.

Canale C., Arpino F., Cortellessa G. , Grossi G. Different numerical approaches for the analysis of a waste-to-energy plant. *Submitted to Applied Thermal Engineering*

CONFERENCE PROCEEDINGS

Arpino F., Fallone C., Bertone M., Canale C., Cortellessa G., Dell'Isola M., Grossi G., Ficco G. and Moretti L. (2022). Green hydrogen for RES energy storage and natural gas system decarbonization: a case study in central-southern Italy. *Atti del XXII Congresso Nazionale CIRIAF*.

Grossi G., Arpino F., Bertone M., Canale C., Canale L., Cortellessa G., Dell'Isola M., Ficco G. and Moretti L. (2022). Natural gas system decarbonization by green hydrogen injection: a distributed approach. *IOP Conference Series: Earth and Environmental Science* (Vol. 1106, No. 1, p. 012004). IOP Publishing.

Grossi G., Sciacchitano A., Arpino F., Bertone M., Canale C., Cortellessa G. and Moretti L. (2022). CFD numerical simulations of a real car cabin: design, potential and limitations of numerical analysis. *Proceedings of the 39th UIT International Heat Transfer Conference*.

Grossi G., Arpino F., Canale C., Cortellessa G., Dell'Isola M., Del Plato L., Fallone C. and Ficco G. (2023). I possibili impieghi dell'idrogeno verde nell'industria pesante e il ruolo chiave delle hydrogen valleys. *Atti del XXIII Congresso Nazionale CIRIAF*.

Grossi G., Arpino F., Canale C., Cortellessa G., Ficco G. and Lombardi T. (2023). CFD design of a novel device for temperature profile measurement in Waste-to-Energy plants. *Proceedings of the 40th UIT International Heat Transfer Conference*.

Canale C., Arpino F., Cortellessa G., Ficco G., Grossi G., Huovinen M. and Karvinen A. (2023). A 3D numerical model for the performance analysis of a differential pressure flow meter in transient conditions for liquid fuels. *Proceedings of the 40th UIT International Heat Transfer Conference*.

Canale C., Arpino F., Cortellessa G., Ficco G., Grossi G. and Büker *O. (2024)* Investigation of the performance of an orifice plate flowmeter under transient conditions for liquid fuel *Proceedings of the IMEKO conference 2024, published on Measurement: Sensors.*